Upscaling multiphase flows in heterogeneous porous media and its application to EOR

Narges Dashtbeshbadounak

▶ **To cite this version:**

Narges Dashtbeshbadounak. Upscaling multiphase flows in heterogeneous porous media and its application to EOR. Applied geology. Sorbonne Université, 2021. English. NNT : 2021SORUS084 . tel-03615453

HAL Id: tel-03615453
https://theses.hal.science/tel-03615453

Submitted on 21 Mar 2022

HAL is a multi-disciplinary open access archive for the deposit and dissemination of scientific research documents, whether they are published or not. The documents may come from teaching and research institutions in France or abroad, or from public or private research centers.

L'archive ouverte pluridisciplinaire **HAL**, est destinée au dépôt et à la diffusion de documents scientifiques de niveau recherche, publiés ou non, émanant des établissements d'enseignement et de recherche français ou étrangers, des laboratoires publics ou privés.

Sorbonne Université

Géosciences, Ressources Naturelles et Environnement (ED 398)

IFP Energies Nouvelles, Direction Sciences de la Terre et Technologies l'Environnement

Changement d'échelle de déplacements de fronts en milieux hétérogènes et application à l'EOR

Par Narges Dashtbeshbadounak

Dirigée par Dr Benoît Noetinger

Présentée et soutenue publiquement le 5 mars 2021

Devant un jury composé de :

Dr Benoît Noetinger	IFPEN, FR	Promoteur et directeur de thèse
Dr Guillaume Enchéry	IFPEN, FR	Co-Promoteur de thèse
Dr Ann Muggeridge	Imperial College, UK	Rapporteur
Dr Frederick Delay	Université de Strasbourg, FR	Rapporteur
Dr Leila Heidari	Total, FR	Examinateur
Dr Pierre-Yves Lagrée	Sorbonne Université, FR	Examinateur

Abstract

Numerical modelling is a widely used tool in applied geoscience for quantifying flow in porous media, that is necessary to predict performance and optimize prospect exploitation at minimal environmental risk and cost. Reaching a satisfactory approximation of the exact solution and a robust numerical model of multiphase flows is particularly challenging because of the heterogeneity of the porous medium across a wide range of length scales, the coupling and nonlinearity of the driving equations, and the necessity of capturing all scales in the macroscale numerical model in a computationally efficient way.

We have developed a sequential approach to accelerate immiscible multiphase flow modelling in heterogeneous porous media using discontinuous Galerkin methods and dynamic mesh coarsening. This approach involves dynamic domain decomposition and different solution strategies in the different flow regions, using a criterion that can be fastly evaluated. We use high-resolution grids and low order methods in regions near the saturation discontinuity and a discontinuous Galerkin method along with low-resolution grids in single-phase flow regions of the domain. We present a fast technique to estimate the position of the saturation front and identify the flow zones that need high-resolution gridding and eventually, we demonstrate the accuracy of our approach through test cases from the second SPE10 model by comparing our results with fine-scale simulations.

Acknowledgement

I am grateful to many people for their support, scientific or otherwise, during the three years of working on this PhD thesis. First, I would like to express my gratitude and appreciation to my supervisors: Dr Benoît Noetinger for giving me the opportunity to pursue a PhD, and for his tremendous guidance throughout this work; and Dr Guillaume Enchéry for his continuous support and for sharing his wide knowledge on numerical modelling. I would also like to thank my committee members, Dr Ann Muggeridge, Dr Frederick Delay, Dr Leila Heidari, and Dr Pierre-Yves Lagrée for reviewing this dissertation as well as for their helpful comments and suggestions.

My gratitude also goes to Professor Béatrice Rivière, who reviewed my mid-thesis work and gave me a piece of critical advice that really encouraged me to improve my work. I benefited a lot from her vast knowledge on the subject.

Furthermore, I would like to thank the Department of Computational Physics of Porous Media of IFPEN for their financial support that made this research possible, and for their scientific support and helpful advice about my work.

I am very thankful to my colleagues and friends in IFPEN, Dr Nickolas Sobecki, Dr Omar Gassara, Dr Bastien Hamlat, Dr Zaineb Zaafouri, Sina Momeni, Andrea Romero Hernandez, Anyssa Diouf, Rosario Ruffino, Michelle Orea, Pierre Hacquard, Dr André Bruch, Djaméla Buda, and many others. I learnt a lot from their diverse academic and cultural backgrounds and greatly enjoyed their friendship over the years.

Last but not least, I would like to thank my parents, my family, and my friends in Iran and the ones I made in France, for supporting me and cheering me on. And of course, a big thank you to Julien, for his limitless patience and encouragement. I love you.

Contents

List of Figures

List of Tables

Nomenclature

Greek symbols

Ω	Computational domain
$\{\Omega_i\}$	Set of cells Ω_i of the spatial domain Ω
$\widehat{\Omega}$	Reference element
$\lvert\Omega_i\rvert$	Volume of the cell Ω_i
$\varepsilon = \{E\}$	Set of all faces
ε_Ω	Set of interior faces
ε_D	Set of the Dirichlet boundary faces
ε_N	Set of the Neumann boundary faces
$\varepsilon_{\partial\Omega}$	Set of boundary faces
ϵ	Tuning parameter
ζ_F^n	Set of all faces σ_{ij} where the front crosses the segment $(\boldsymbol{x}_i, \boldsymbol{x}_j)$
σ_{ij}	Interface between two neighbouring cells Ω_i and Ω_j
ϕ	porosity
φ_{il}	lth basis function on Ω_i
μ	Fluid viscosity
ρ	Fluid density
λ_T	Total mobility
λ_α	Phase mobility
γ_{ij}	Penalty term at face σ_{ij}
σ^2	Variance
σ	Standard deviation
ϵ	Tuning parameter
ω	Arbitrary smooth test function
η	penalty coefficient

variables

k^*	Upscaled permeability
k_{eff}	Effective permeability

p_c	Capillary pressure
s, s_w	Water saturation
s_{o_r}	Residual oil saturation
s_{w_i}	Irreducible water saturation
s_f	Water saturation at the front
s_o	Oil saturation
s_w^*	Reduced water saturation
v_{ij}	Total flux across the face σ_{ij}
$\boldsymbol{D}_{eff}$	Effective diffusivity tensor
F_i	Affine mapping from $\widehat{\Omega}$ to Ω_i
$\boldsymbol{v}_\alpha$	Phase velocity
Δt	Time step
A	Cross-sectional area
D	Dimension
L	Length
M	Viscosity ratio
P	Order of approximating polynomial
R	Number of quadrature points
c	Concentration
k	Absolute permeability
n	Time step number
p	Pressure
q	Flow rate of source and sink term
z	Vertical coordinate
$\boldsymbol{D}$	Diffusivity tensor
$\boldsymbol{n}$	Unit outward normal vector
$\widehat{\boldsymbol{q}}_r$	rth quadrature point in reference element $\widehat{\Omega}$
$\boldsymbol{v}$	Darcy total velocity
$\boldsymbol{x}$	Position vector
$\boldsymbol{y}$	Arbitrary smooth test function

Abbreviations

AIM	Adaptive implicit method
BL	Buckley Leverett
DG	Discontinuous Galerkin
FD	Finite difference
FFTMA	Fast Fourier transform moving average
FV	Finite volume
HDG	Hybridized discontinuous Galerkin
HMM	Hybrid mimetic mixed
IMPES	Implicit pressure – explicit saturation
IMPIMS	Implicit pressure – implicit saturation
IP DG	Interior penalty discontinuous Galerkin
LDG	Local discontinuous Galerkin
LGR	Local grid refinement
MPFA	Multi-point flux-approximation
MsFV	Multiscale finite volume
MsMFE	Multiscale mixed finite element
PDE	Partial differential equation
PVI	Pore volume injected
REV	Representative elementary volume
TOF	Time of flight
TPFA	Two-point flux-approximation

1 Introduction

A porous medium is a medium containing void spaces. These void pore spaces are generally connected such that a fluid can flow through it. Some examples of natural porous media are soil and rock. Understanding flow and transport in porous media is important in many human-controlled subsurface processes. Geothermal energy (Paksoy, 2007), as one of the renewable energy sources, needs a thorough understanding of the geothermal subsurface system to reach its total global potential (Matek, 2016). Another important application is the geological storage of CO_2. Indeed, carbon dioxide capture and storage have been proposed as one of the options to reduce the accumulation of greenhouse gases in the atmosphere (IEA, 2020). Some of the main challenges of this geological storage are CO_2 leaks, to the surface or the freshwater aquifers, through faults or abandoned wells (Lokhorst and Wildenborg, 2005). Impacts prediction of injecting CO_2 into the subsurface needs a deep understanding of flow problems in porous media. Last but not least, hydrocarbon recovery, remaining as one important source of energy in the foreseeable future, also requires an understanding of the balance of forces acting at different scales to maximize production especially in the secondary and tertiary recovery processes for existing resources (Bouquet et al., 2020).

Numerical modelling is a major tool for understanding and predicting fluid flow and transport in heterogeneous porous media in all these subsurface processes and also other energy-related applications including groundwater remediation and nuclear waste storage. Because of the importance of numerical modelling in decision making at geoscience management and engineering levels, the efficiency and accuracy of the simulation results are key. However, computational efficiency and solution accuracy are often difficult to maintain simultaneously.

In this work, we consider and adopt the language of the hydrocarbon recovery. Nevertheless, the methods and strategies presented apply to other domains of multiphase flow in porous media.

1.1 Statement of the problem

A reservoir model consists of a geological model describing the petrophysical properties of the reservoir, a flow model describing how the fluids are flowing, and the drive mechanisms describing the fluid communication to the surface (see Figure 1.1 for an illustration).

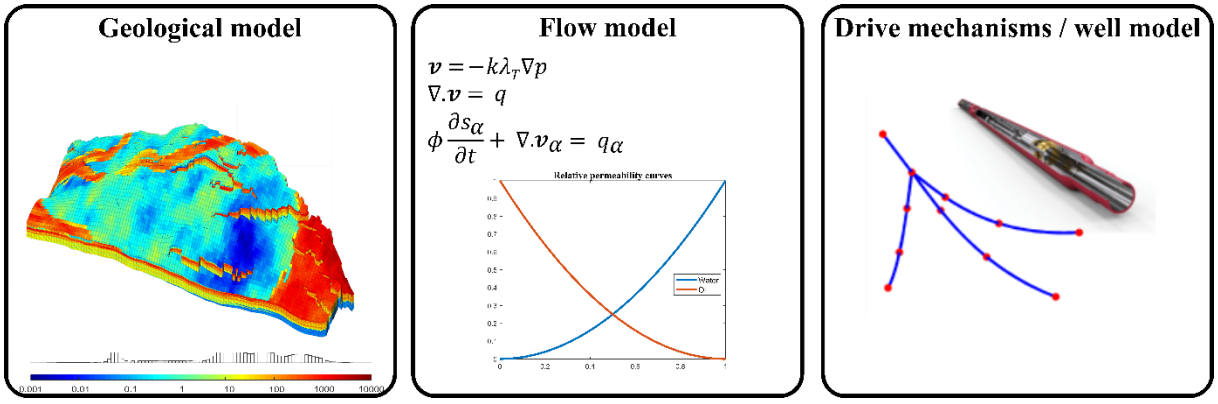

Figure 1.1: The main components of a reservoir simulation model (Lie, 2019).

One of the main challenges related to accurate numerical modelling in porous media is the heterogeneity of the rock properties which can vary over several orders of magnitude from pore to reservoir scale. It is well-known that fine-scale heterogeneities, implying strong localization or channelling of the flow, can change field-scale processes leading to early breakthrough or poor recovery that can hinder the global profitability of an EOR project (De-Wit and Homsy, 1997b). To have a more detailed representation of the medium heterogeneity, the geological models which describe the reservoir rock properties, are generated at high spatial resolutions.

The porous medium properties have different scales depending on the source of data and the methods of measurements. Core plug data is measured at the centimetre scale, while well log data is at the meter scale, and seismic data is at the order of a hundred meters (see Figure 1.2). Moreover, the amount of available data is limited. Therefore, it is necessary to use statistical methods to integrate these different-scale data coming from different measurement processes and to populate them over the whole reservoir domain. The current reservoir characterization methods can provide high-resolution geological models containing a very large number of grid cells. These geological models, generally, include several equally probable realizations of the same reservoir. The propagation of sparse data over the whole domain results in high uncertainties that

must be quantified too (Floris et al., 2001). These uncertainties associated with the distribution of the porous medium properties, mainly the permeability, are another challenge faced in the numerical modelling of multiphase flow. Reservoir engineers must quantify the uncertainties on the output data of interest, such as hydrocarbons recovery, to recommend the best decisions to increase the production and reduce the risks.

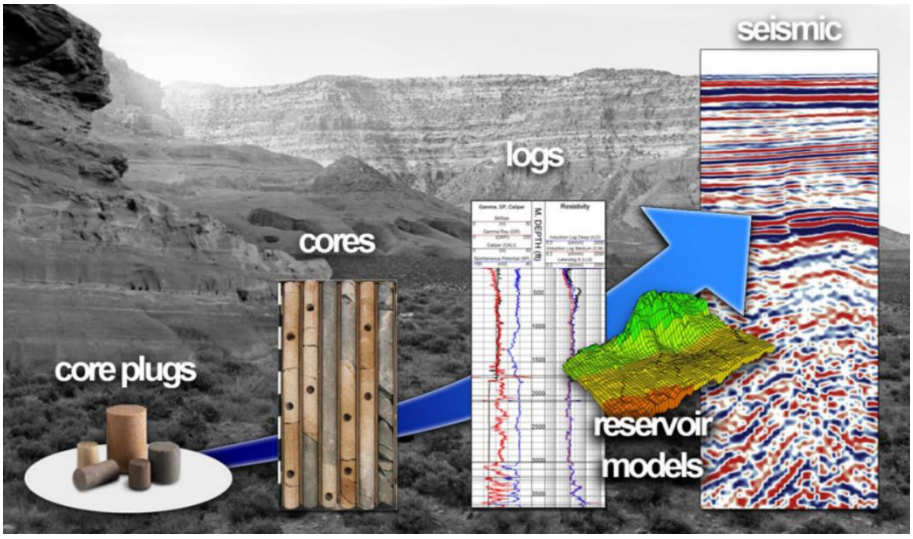

Figure 1.2: Representation of different data with different length scales used in reservoir modelling (EPGeology, 2014).

Another challenge arises from the discretization of the governing equations. A desirable discretization method should be accurate, stable, and locally conservative to respect the physical processes. Another important feature is the computational efficiency. Low-order discretization methods such as finite volume (FV) methods are currently widely used in reservoir simulations. They are stable, mass conservative, and computationally efficient. To improve the accuracy of the approximating solution, especially in the presence of highly heterogeneous anisotropic media, there has been a great interest in high order discretization methods, such as discontinuous Galerkin (DG) methods, over the last two decades. However, these high-order methods have a larger number of degrees of freedom, and ultimately higher computational time compared to low-order numerical methods in large-scale reservoir simulations. Moreover, the governing equations are usually nonlinearly coupled. There exist several solution methods to solve these coupled systems of equations, from fully implicit to sequential approaches, each having advantages and disadvantages in terms of computational cost, stability, and accuracy.

Solving multiphase flow equations directly on high-resolution geological models containing millions of cells is not computationally efficient. Even with high computing power, it is necessary to run several simulations on different independent realizations, as carrying out a single simulation on a highly detailed geological model is not sufficient if an estimation of the uncertainty is required (Gorell and Bassett, 2001). Thus, upscaling, the process of propagating the properties from a high-resolution model to a coarser model with less resolution, remains necessary whatever the available computing resources are. An example of permeability upscaling is shown in Figure 1.3 from the SAIGUP project (Manzocchi et al., 2008). The important aim of any upscaling method is to capture the effect of small-scale heterogeneities in an averaged sense, with well-controlled loss of information. While additive rock properties, like porosity, may be upscaled using the direct arithmetic averaging, upscaling the permeability and transmissibility is not straightforward due to the non-linear dependence on the fine-scale properties. The situation is far more complex when considering multiphase flows, due to the strong coupling in the governing equations that are the basis of the viscous fingering (Ganjeh-Ghazvini, 2019).

Developing a robust, reliable, accurate, and efficient reservoir model is still an open problem.

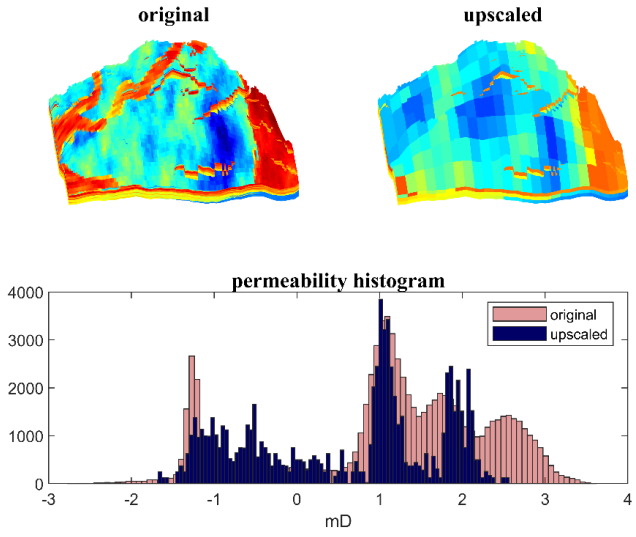

Figure 1.3: An example of upscaling the permeability from the SAIGUP project (generated using an example in MRST[1])

[1] sintef.no/projectweb/mrst/

1.2 Research objective

The main purpose of this study is to propose an efficient and accurate solution strategy that addresses the challenges of multiphase flow simulations and maintains a high order of accuracy in the whole domain. Such accurate and efficient model is needed for history matching, predicting the production in different scenarios, and better decision making for the optimal recovery plan. In this work, we focus on immiscible displacement processes, like water or gas injection during the secondary oil recovery. In immiscible displacements, viscous fingerings at the interface separating the fluids because of the injection of a less viscous fluid to displace a more viscous one may be amplified by the small-scale heterogeneity of the porous medium that controls the so-called "channelling" of the flow. The coupling of viscous fingering and channelling at the front can lead to some non-trivial large-scale behaviour and can dominate the flow and control the efficiency of hydrocarbon recovery (De-Wit and Homsy, 1997a). We present an approach that treats different flow regions separately. Implementing different solution strategies in different flow regions, with their specific features, allows increasing the solution accuracy while maintaining the computational cost at a reasonable level. The proposed model is based on adaptive gridding and higher-order discretization methods.

This work presents an approach that autonomously and dynamically generates a mesh that adapts its resolution with a lower resolution in smooth regions like single-phase flow regions and a higher resolution in local sharp regions like the front. This adaptive coarsening works thanks to the proposed technique that allows fast prediction of flow patterns and the front position. The objective of this technique is to approximately track the position of the front, without solving the fully-coupled pressure and saturation equations on the whole grid.

As a result of using a high-resolution mesh in the multiphase flow region near the front, the use of any multiphase upscaling technique is avoided. The finite volume method in this high-resolution region gives satisfactory results in a computationally efficient way. Far from the front, in single-phase areas, the grid is coarsened, and a linear DG scheme is used to get more accurate total fluxes.

1.3 Thesis outline

In chapter 2, some of the key concepts associated with flow in porous media as well as the governing equations of single and multiphase flow models are described. A review of the literature is presented in chapter 3, to understand the fundamentals and challenges of reservoir modelling as well as to characterize the knowledge gap in more detail. Chapter 4 is devoted to the discretization methods, their implementation and associated numerical errors. In chapter 5 we present the technique developed to predict the position of the front in a computationally efficient way, while in chapter 6, we detail the proposed solution strategy and analyse its advantages and limitation through different numerical simulations. Last but not least, we present the conclusions and perspectives in chapter 7.

2 Governing equations

In this chapter, we review some of the main concepts and formulate the driving equations of the flow and transport in porous media, to provide an understanding of these equations in single-phase and multiphase flows in the reservoir.

Porosity and permeability are the main properties of a porous medium. The ratio of the volume of void spaces to the total volume is defined as the porosity, ϕ. With this definition, ϕ varies between zero and one. The absolute permeability is an intrinsic property of the porous medium that measures its ability to allow a single fluid to flow through it. The permeability is generally correlated to the porosity. The general form of permeability is a tensor, meaning that the permeability in each direction depends on the permeabilities in other directions. In 2D, the permeability tensor is a matrix of the form $\begin{bmatrix} k_{xx} & k_{xy} \\ k_{yx} & k_{yy} \end{bmatrix}$, in which the off-diagonal terms represent this dependence. When the off-diagonal terms are all zero and diagonal terms are equal, the permeability becomes a scalar property that does not depend on the direction and is called isotropic. In other cases, the permeability is anisotropic.

Natural porous media are generally heterogeneous at all length scales from the pore scale to the reservoir scale in the order of several kilometres. Full-field numerical simulation of flow problems at the pore-scale is not computationally feasible. Moreover, obtaining data at the microscale is too challenging and too precise for most practical situations. A common scale is the representative elementary volume (REV). REV, usually in the order of several hundred to thousands of pores, is the smallest volume over which a property average does not change with a small change in its size.

2.1 Single-phase flow

One of the most fundamental laws in reservoir simulations is Darcy's law, by the French engineer Henry Darcy (Darcy, 1856). In one dimensional single-phase flow, Darcy's law can be represented as:

$$\frac{Q}{A} = -\frac{k}{\mu}\frac{\Delta p}{L} \qquad \text{Eq. 2.1}$$

where Q is the flow rate of the fluid, A is the cross-sectional area of the porous medium, L is its length, μ is the viscosity of the fluid, k is the permeability of the porous medium, and Δp is the pressure difference across the length of the medium. $\boldsymbol{v} = Q/A$ is called the Darcy velocity.

In multi-dimensions, the general form of Darcy's law reads:

$$\boldsymbol{v} = -\frac{k}{\mu}(\nabla p - \rho g \nabla z) \qquad \text{Eq. 2.2}$$

where ρ is the density of the fluid and z is the vertical coordinate. To derive the single-phase fluid flow system of equations at the macroscopic scale, the mass conservation law is applied to a REV computational domain Ω:

$$\frac{\partial}{\partial t}\int_{\Omega} \phi \rho d\boldsymbol{x} + \int_{\partial\Omega} \rho \boldsymbol{v}.\boldsymbol{n} ds = \int_{\Omega} \rho q d\boldsymbol{x} \qquad \text{Eq. 2.3}$$

where $\boldsymbol{n}$ is the unit vector normal to the boundary of the domain $\partial\Omega$, and q is the flow rate of the source or sink, i.e. the inflow and outflow of the fluid per volume. Applying Gauss' theorem to Eq. 2.3, the mass conservation equation for single-phase flows becomes:

$$\frac{\partial \phi \rho}{\partial t} + \nabla.(\rho \boldsymbol{v}) = \rho q. \qquad \text{Eq. 2.4}$$

In this thesis we make some assumptions as follows:

- negligible gravitational effects,
- constant fluid viscosity,
- isothermal reservoir condition,
- incompressible rock and fluid.

With these assumptions, and using Darcy's law in Eq. 2.4, the single-phase flow equation or the "pressure" equation simplifies to:

$$\nabla . \boldsymbol{v} = -\nabla . \left(\frac{k}{\mu} \nabla p \right) = q. \qquad \text{Eq. 2.5}$$

To close the model, boundary conditions are imposed:

$$\begin{cases} p = p_D & on\ \partial\Omega_D \\ \boldsymbol{v} . \boldsymbol{n} = 0 & on\ \partial\Omega_N \end{cases} \qquad \text{Eq. 2.6}$$

which correspond to Dirichlet and homogeneous Neumann boundary conditions on the boundaries of the domain.

2.2 Multiphase flow

In most applications of reservoir simulations, two or more phases are generally present, e.g., water or gas displacing oil or CO_2 displacing the brine. In multiphase flows, each phase occupies a certain fraction of the pore space and new properties are introduced in the flow model (Marle, 1981). The pore volume fraction occupied by each phase, α, is defined as its saturation, s_α. We assume that all the fluid phases fill the void space, i.e.

$$\sum_\alpha s_\alpha = 1. \qquad \text{Eq. 2.7}$$

Another property in a multiphase flow model is the relative permeability which measures how the presence of one phase hinders the ability of the flow of another phase. In the presence of other phases, each phase experiences a reduced permeability called the effective permeability, defined as:

$$k_\alpha^{eff} = k_{r_\alpha} k \qquad \text{Eq. 2.8}$$

where the relative permeability, k_{r_α}, generally is a function of phase saturation, s_α, but their dependence cannot de defined exactly. It is a popular choice to use some empirical laws to relate the saturation and the relative permeability.

At the pore scale, due to the interfacial tension between two immiscible fluids, the pressure in these two phases is generally different. This pressure difference across the fluids interface is called the capillary pressure, p_c:

$$p_c = p_i - p_j \qquad \text{Eq. 2.9}$$

where p_i and p_j denote the pressure in the i and j phases, usually being the nonwetting and wetting phases, respectively.

In this work, we consider an immiscible two-phase flow model, for example, water and oil in a waterflood problem in a porous medium. We neglect capillary effects, along with the other assumptions mentioned in single-phase flow model. We use the power law, one of the most common empirical relations to define the relative permeability that reads in terms of reduced water saturation, $s_w^* = \frac{s_w - s_{w_i}}{1 - s_{w_i} - s_{o_r}}$ (Brooks and Corey, 1964):

$$k_{r_w} = k_{r_w}^{max}(s_w^*)^{n_w}$$
$$k_{r_o} = k_{r_o}^{max}(1 - s_w^*)^{n_o} \qquad \text{Eq. 2.10}$$

s_{w_i} and s_{o_r} are irreducible water saturation and residual oil saturation, respectively. $k_{r_\alpha}^{max}$, or the maximum relative permeability of each phase α, and n_α, the exponent of each phase, should be generally found by fitting to the measured data. In the numerical examples throughout this manuscript, we set both exponents, n_w and n_o to 2, a popular choice in the industry, and the maximum relative permeabilities to 1, $k_{r_w}^{max} = k_{r_o}^{max} = 1$. The corresponding relative permeability curves are shown in Figure 2.1.

Like in single-phase flows, when modelling the behaviour of multiple fluids flowing in porous media, mass conservation and Darcy's law are used to derive the system of equations. Considering the fluids to be incompressible, the conservation equation for each phase is:

$$\phi \frac{\partial s_\alpha}{\partial t} + \nabla.(\boldsymbol{v}_\alpha) = q_\alpha, \quad \alpha = o, w \qquad \text{Eq. 2.11}$$

where $\boldsymbol{v}_\alpha$ is the phase velocity, and q_α is the flow rate of the source and sink in each phase. We write the two mass conservation equations into a more manageable system of equations, composed of a pressure or flow equation and a saturation or transport equation.

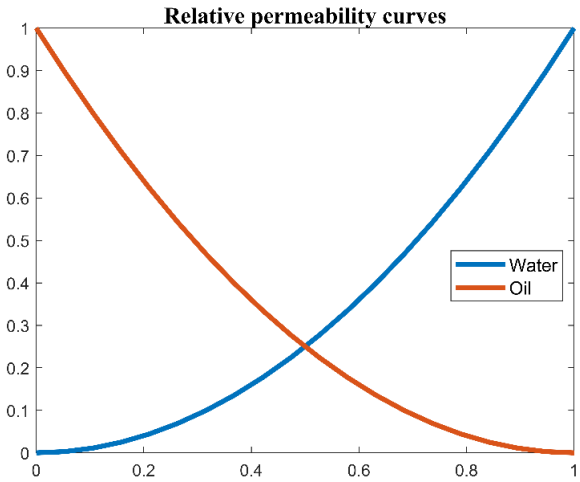

Figure 2.1: Water and oil relative permeability curves as a function of water saturation, computed using the quadratic law with the unit endpoint values.

2.2.1 **Pressure equation**

Darcy's law for the phase velocity, in the absence of gravitational and capillary forces, reads:

$$\boldsymbol{v}_\alpha = -\frac{k k_{r_\alpha}(s_\alpha)}{\mu_\alpha} \nabla p \qquad \text{Eq. 2.12}$$

with p the local pressure which is equal to water and oil pressure in our case, and μ_α the phase viscosity. k_{r_α}/μ_α is called the phase mobility and is denoted by λ_α. Adding the conservation equation, Eq. 2.11, of both phases and considering that $s_w + s_o = 1$ gives:

$$\nabla . \boldsymbol{v} = q \qquad \text{Eq. 2.13}$$

with $\boldsymbol{v}$ the total velocity or the sum of water and oil velocities, and q the total source and sink term. Writing Darcy's law for the total velocity gives:

$$\boldsymbol{v} = -k\lambda_T \nabla p \qquad \text{Eq. 2.14}$$

where λ_T is the total mobility, the sum of water and oil mobilities:

$$\lambda_T = \lambda_o + \lambda_w = \frac{k_{r_o}}{\mu_o} + \frac{k_{r_w}}{\mu_w} \quad \text{Eq. 2.15}$$

A substitution of total Darcy's law into the overall mass-conservation law gives the 'pressure equation':

$$-\nabla.(k\lambda_T(s_w)\nabla p) = q. \quad \text{Eq. 2.16}$$

The boundary conditions to complete the pressure equation are the prescribed pressure in Dirichlet boundaries and the homogeneous no-flow condition in Neumann boundaries, as described in Eq. 2.6.

2.2.2 **Saturation equation**

Writing the conservation equation of water in terms of total velocity and water fractional flow f_w leads to the 'saturation equation':

$$\phi \frac{\partial s_w}{\partial t} + \nabla.(f_w(s_w)\boldsymbol{v}) = q_w \quad \text{Eq. 2.17}$$

to be solved with the initial and boundary conditions:

$$\begin{cases} s_w = s_w^0, & in\ \Omega \\ s_w = s_D, & if\ \boldsymbol{v}.\boldsymbol{n} < 0\ \ on\ \partial\Omega \end{cases} \quad \text{Eq. 2.18}$$

with s_w^0 the initial saturation in the domain and s_D the Dirichlet condition on the inlet boundary of the domain. The fractional flow function $f_w = \lambda_w/\lambda_T$ measures the water fraction of the total flow.

The system of equations described through Eq. 2.16 to Eq. 2.18 is nonlinearly coupled. The mobility term in the pressure equation is saturation dependent and the flux function term in the saturation equation is pressure dependent. There are several approaches to numerically solve this coupled system of equations. In a fully implicit approach, all the variables are solved simultaneously. This approach is unconditionally stable, but its implementation and solution are

computationally expensive, especially for large problems like full-field reservoir simulations. Another class of methods, sequential approaches, aims at solving the pressure and saturation equations separately and sequentially. The main advantage of these approaches lies in the reduction of the size of the linear systems to be solved, and therefore superior computational efficiency. Another important advantage is that it allows mixing different discretization methods in the same system, which can be very beneficial as the flow and transport equations have different mathematical characters, the elliptic character of the flow versus the hyperbolic character of the fluid transport (Bell et al., 1986). Sequential approaches have different forms, like the so-called IMPES (implicit pressure – explicit saturation) and the IMPIMS (implicit pressure – implicit saturation) schemes (Coats, 2000; Fagin and Stewart, 1966; Stone and Garder, 1961). Some of the main disadvantages of sequential approach are the additional memory requirements and the splitting error related to the decoupling of flow and transport equations. One proposed remedy to decoupling error is to add an extra step after solving the transport equation to revisit the flow problem (Hajibeygi and Tchelepi, 2014; Lee et al., 2008). Adaptive implicit method (AIM) is another method which tries to combine advantages of sequential and fully implicit methods by implementing each of them adaptively in the domain (Cao and Aziz, 2002; Spillette et al., 1973; Thomas and Thurnau, 1982). For example, a fully implicit method is most suitable for local areas with large variations in the saturation, while computationally efficient IMPES scheme can be applied elsewhere. The main challenge in AIM is the difficulty of finding a suitable switching criterion (Marcondes et al., 2009).

3 Literature review

This chapter presents a review of literature, starting with different approaches to describe single-phase and multiphase flows in porous media, from stochastic to numerical methods and fast diagnostic tools. Next, a review and analysis of upscaling methods, in single-phase and multiphase flow modelling, known as one of the classical approaches to accelerate flow simulations, is detailed followed by a brief review of some alternative techniques. In the last section, we review some of the methods used to locate the saturation discontinuity, one of the most important local features of an immiscible multiphase flow model.

3.1 Stochastic approaches

In the stochastic approach, input parameters such as permeability and porosity are considered as being random functions of the position. Geostatistical tools provide methods allowing to generate as many random maps honouring imposed statistical properties as desired (Guadagnini et al., 2018). In this thesis, FFTMA (Le Ravalec et al., 2000) will be used to generate spatially correlated Gaussian random maps.

The idea of stochastic methods is to be able to estimate the ensemble average of the properties of interest, including dynamic data such as pressure, saturation, and cumulated oil production that are themselves random. Indeed, the randomness of the input parameters propagates through the solution of the partial differential equations that govern the flow. In practice, this ensemble average could also be obtained by averaging many independent simulations: the so-called Monte Carlo approach. Although easy to parallelize, it remains an expensive approach in the case where many simulations need to be performed, especially if each simulation is computationally costly and long. Moreover, the number of realizations that are required is itself a part of the issue.

The core idea of stochastic methods is to look for the output parameters average, such as the pressure $\langle p(\boldsymbol{x}, t)\rangle$ and the saturation $\langle s(\boldsymbol{x}, t)\rangle$, and to find if an effective set of equations driving these averages may be found by some methods. The associated variance may be studied by analogous methods, to provide some information about the related uncertainties.

Although conceptually simple, some difficulties may be anticipated. First, the form of the equations may be changed, even in the simplest single-phase context by considering ensemble-averaged Darcy's law. It may be shown under a quite general hypothesis (Nœtinger and Gautier, 1998) that the linear relation between averaged flux and pressure gradient becomes an integrodifferential operator that only keeps the overall linearity of the original problem, a strong requirement. The case of a tracer advected in a random flow-field leads to the so-called macro-dispersion (Gelhar and Axness, 1983). In two-phase flows, few works followed this approach (Artus et al., 2004; Langlo and Espedal, 1994; Spesivtsev and Teodorovich, 2007; Zhang and Tchelepi, 1999).

Another difficulty is that even if the form of the ensemble-averaged equation is known, the question on how to relate the associated coefficients to the input geostatistical parameters remains. In the context of single-phase problems, considering the ensemble averaging of Darcy and advection/dispersion equations, the main approach is the small perturbation expansion (Dagan, 1989). Considering that the local permeability may be decomposed as:

$$k(\boldsymbol{x}) = \langle k \rangle + \epsilon \delta k(\boldsymbol{x}) \qquad \text{Eq. 3.1}$$

With the perturbation value $\delta k(\boldsymbol{x}) \geq 0$, the ensemble-average $\langle k \rangle$, and the tuning parameter ϵ, one may expand the solution of Laplace and tracer equations in powers of ϵ. It may be anticipated that the second-order term provides contributions involving averages of $\langle \delta k(r) \delta k(r') \rangle$ corresponding to permeability correlations. The quantity $\langle \delta k(r) \delta k(r) \rangle = \sigma_k^2$ is the permeability covariance function. It allows expressing the effective permeability up to the second order as:

$$k_{eff} = \langle k \rangle (1 - 1/D \, \sigma_k^2 / \langle k \rangle^2 + \cdots) \qquad \text{Eq. 3.2}$$

in which D=1,2,3 is the number of dimensions available to flow. Further developments were performed to get higher-order terms, generalizing the approach to higher variances using field theoretical approaches, Feynman diagrams, and so on (Dagan, 1993; Indelman and Abramovich, 1994; King, 1987; Noetinger, 1994).

In the case of the passive tracer transport equation that reads:

$$\frac{\partial c}{\partial t} + \nabla.(\boldsymbol{v}c) = \nabla.(\boldsymbol{D}.\nabla c) \qquad \text{Eq. 3.3}$$

in which c is the concentration, $\boldsymbol{v}$ is the local Darcy velocity that depends on the underlying disorder, and $\boldsymbol{D}$ is the diffusivity tensor that represents the local molecular diffusion/dispersion tensor. The stochastic approach leads to an effective equation that reads asymptotically:

$$\frac{\partial \langle c \rangle}{\partial t} + \nabla.(\langle \boldsymbol{v} \rangle \langle c \rangle) = \nabla.\left(\boldsymbol{D}_{eff}.\nabla c\right). \qquad \text{Eq. 3.4}$$

The tensor $\boldsymbol{D}_{eff}$, proportional to $\boldsymbol{v}\sigma_k^2 l_c/\langle k \rangle^2$ with the correlation length l_c, may have a non-zero value even if the input **D** vanishes. This corresponds to the so-called macro-dispersion phenomena (Dagan, 1989; Gelhar and Axness, 1983) which represents the mixing due to the fluctuations of streamlines of local velocity $\boldsymbol{v}$. Once again, methods such as renormalization group techniques were proposed to increase the validity range of the results (Jaekel and Vereecken, 1997). Good agreement was obtained using field data.

For completeness, let us mention another class of stochastic techniques that were developed for modelling flow in fracture networks. The framework is mainly percolation theory and involves different methods. The interested reader can look at the textbooks of Berkowitz and Balberg (1993) and Hunt et al. (2014).

Previously listed methods were developed for problems driven by linear equations, such as Darcy equation with random coefficients, and passive tracer advection/dispersion. The situation is far more complex when two-phase flow, such as water/oil in porous media, is considered. The generalization of stochastic methods to two-phase flows is difficult due to the coupling between the pressure equation and the saturation conservation equation which leads to a coupling between viscous effects and channelling effects. Partial decoupling approximations (Langlo and Espedal, 1994; Zhang and Tchelepi, 1999) can lead to erroneous results (Nœtinger et al., 2005). The technical difficulty is that the existence of the Buckley Leverett discontinuity leads to technicalities for setting up the perturbation theory. A change of variable proposed by King and Dunayevski (1989) allowed to get some results up to the second order in the

permeability variance for a limited range of validity (Artus et al., 2004; Noetinger et al., 2004; Spesivtsev and Teodorovich, 2007). The main result is that finding an effective transport equation sharing some similarities with non-linear advection/dispersion equation driving the ensemble-averaged saturation remains to be done.

3.2 Numerical methods

Numerical modelling of multiphase flows in porous media aims at solving the governing equations through their discretization. The main challenges regarding the flow equation are the accuracy of the flux that enters the transport equation and dealing with the heterogeneous permeability that can vary by several orders of magnitude over the domain. On the other hand, the main difficulties for numerically solving the hyperbolic problems of conservation laws lie in the presence of discontinuities in the exact solution and the complicated coupling of different origins near these discontinuities. In the following, we review the main classical and most widely used methods as well as some advanced discretization methods. To review their mathematical base idea and the strengths and weaknesses, we consider the elliptic flow equation, described in Eq. 2.16. For a more thorough review and comparison of discretization methods in geosciences, see Di Pietro and Vohralík (2014).

3.2.1 Finite difference and finite volume methods

Perhaps the simplest and oldest approach is the finite difference (FD) method. Finite difference methods work based on replacing the derivatives in the partial differential equation (PDE) with an approximation based on Taylor series. Even though this approach is very easy to implement and can be very efficient, the need for an orthogonal grid structure limits their application in more general and complex domain geometries.

In many engineering processes, including flows in porous media, mass conservation is an important property. In these contexts, finite volume (FV) methods are very popular. The reason is that finite volume methods, unlike finite difference methods, have physical principles behind them and can be derived only based on the conservation of the desired quantity over control volumes, independently from the continuous equation. In FV methods the unknowns are approximated by constant values for each cell or control volume, that represent the volume-

averaged values. This another difference with finite difference methods, in which the physical quantities are calculated at specific nodes, gives FV methods more geometric flexibility. Despite these differences in derivations, FV and FD methods are usually used as identical in the literature. A common approach to derive a finite volume representation of the flow equation is to integrate Eq. 2.16 over a grid cell or control volume Ω_i in the domain Ω, and use the divergence theorem to obtain:

$$\int_{\partial\Omega_i} \boldsymbol{v}.\boldsymbol{n}\, ds = \int_{\Omega_i} q d\boldsymbol{x}, \qquad \text{Eq. 3.5}$$

where $\boldsymbol{n}$ is the outward unit normal vector on the boundaries of the grid cell $\partial\Omega_i$. Different finite volume schemes approximate the flux through interfaces from a set of neighbouring cell-averaged pressure values. The two-point flux-approximation (TPFA) scheme is the simplest form of a finite volume discretization. It works based on approximating the flux across the face, $\sigma_{ij} = \partial\Omega_i \cap \partial\Omega_j$, using the values in the two neighbouring cells, Ω_i and Ω_j, on the sides of the face σ_{ij}:

$$v_{ij} = |\sigma_{ij}|\lambda_{ij}\frac{p_i - p_j}{d_{ij}} \qquad \text{Eq. 3.6}$$

where $|\sigma_{ij}|$ denotes the area of the face, λ_{ij} denotes the mobility defined at the face, and d_{ij} is the distance between the neighbouring cell centres. This scheme is simple to implement and computationally efficient, and that is why it is widely used in industrial software. However, the main constraint in this scheme is its conditional consistency. If the grid does not satisfy some orthogonality condition, called K-orthogonality, which is usually the case in unstructured grids in porous media with complex geology, the solution of the TPFA method will have errors. The severity degree of the error depends on the direction of the interfaces with respect to the direction of the permeability tensor. These artefacts or errors, called “grid orientation effects”, can lead to the convergence to a completely wrong solution if the mentioned orthogonality condition failure is dominant (Aavatsmark, 2007; Faille, 1992; Wu and Parashkevov, 2009).

Another class of finite volume methods, multi-point flux-approximation (MPFA) schemes, aims to overcome the shortcomings of the TPFA scheme. The key idea in this class of

methods is to overcome the conditional consistency constraints by generalizing the approximation of fluxes, from the two cell-averaged values of the neighbouring cells used in the TPFA scheme to a more general approximation with additional terms (Aavatsmark et al., 1998a, 1998b; Aavatsmark et al., 1996; Edwards and Rogers, 1998). For example, considering an orthogonal grid and a permeability tensor k with nonzero off-diagonal terms, for a given function p the flux across the interface σ_{ij}, in the x-direction, will be (Aarnes et al., 2007a):

$$\int_{\sigma_{ij}} \boldsymbol{v}.\boldsymbol{n}\, ds = -\int_{\sigma_{ij}} \left(k_{xx}\partial_x p + k_{xy}\partial_y p + k_{xz}\partial_z p\right) ds \qquad \text{Eq. 3.7}$$

For non-orthogonal grids, partial derivatives in the direction of interfaces also should be estimated. MPFA schemes, like other FV methods, have a physical principle and some continuity equations are imposed to derive the final numerical fluxes. The difference in various MPFA schemes lies in the imposed continuity and conservativity requirements (Droniou, 2014). One of the most known MPFA schemes, the O-method, involves the introduction of an 'interaction region' around each corner point in the grid. An illustration of an interaction region for a two-dimensional grid is shown in Figure 3.1. The interaction region, in the example case of this figure, is composed of four sub-cells from four neighbour cells sharing a vertex. The solution is approximated by a linear function in each of these sub-cells. Continuity of approximating functions at face midpoints and conservativity of fluxes around the vertices are imposed to obtain the final system in the O-scheme. There exist other MPFA schemes, for example, L- and G-methods. See Droniou (2014) for a thorough review of finite volume methods. MPFA methods have also some limitations and drawbacks, from which we can mention their "*conditional coercivity and monotony*", which may result in instabilities and inaccurate approximations, and their higher computational cost in comparison with TPFA methods (Aavatsmark et al., 2007; Droniou, 2014).

There exist other more modern classes of FV methods, for example, hybrid mimetic mixed (HMM) methods, more robust than MPFA methods but at the cost of a higher number of unknowns. The HMM methods are composed of three class of methods: The hybrid finite volume methods (Eymard et al., 2010), the mimetic finite difference methods (Brezzi et al., 2005b; Brezzi et al., 2005a), and the mixed finite volume methods (Droniou and Eymard, 2006). It has

been shown that all these three classes of methods are the same (Droniou et al., 2010). These methods have important properties, including their conservation and stability, which made them an attractive scheme in flow simulations, for example, in the works of Aarnes et al. (2008), Natvig et al. (2011), and Antonietti et al. (2016). However, they have their weaknesses and limitations. One of their weaknesses is the inaccuracy of the solution on coarse meshes in the case of an anisotropic heterogeneity, which comes from their nonlocal computation of the fluxes (Droniou, 2014).

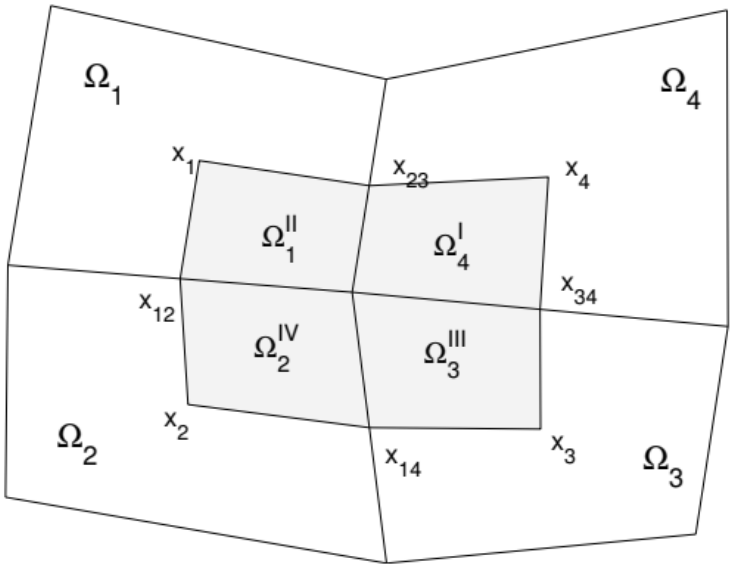

Figure 3.1: An example of the interaction region for a two-dimensional grid with four cells in the O-method (Aarnes et al., 2007a).

3.2.2 **Finite element and discontinuous Galerkin methods**

One of the main constraints of classical finite volume methods is their low order of accuracy. One approach to reach a higher order of approximation is to increase the mesh resolution, which can be a limitation in many applications. Another approach is to approximate the solution with some arbitrary basis functions, such as polynomials, which is the core mathematical idea of finite element and discontinuous Galerkin methods.

One of the main differences of this class of methods with the classical finite difference and finite volume methods is that they solve a weak form of equations. This weak form is

obtained by multiplying the exact form of the equation, for example, Eq. 2.16, called the strong form by an arbitrary test function, ω, and then integrating by part:

$$\int_{\Omega} \omega[-\nabla.(\lambda \nabla p)]d\boldsymbol{x} = 0. \qquad \text{Eq. 3.8}$$

Finite element methods seek for an approximated solution that satisfies the weak form of the equation, where both the approximated solution and the smooth test functions are written as a sum of basis functions. The solution of Eq. 3.8 on the cell Ω_i is generally defined as:

$$p_h = \sum_{l} p_l \varphi_l \qquad \text{Eq. 3.9}$$

where φ_l represents the basis functions and p_l represents the coefficients of the function that approximate p with p_h.

The advantages of finite element methods include the freedom in choosing the basis functions and in the shape of mesh elements used to discretize the computational domain Ω. However, some of the disadvantages of classical finite element methods are related to adaptivity and stability issues. Roughly speaking, discontinuous Galerkin (DG) methods incorporate the favourable features of finite volume and finite element methods, through a combination of element-based discretization and locally defined basis functions. DG methods are like finite element methods but with discontinuities in test functions. DG methods can also be viewed like finite volume methods, in terms of element-wise approximating functions. But, in DG methods, the solution is approximated by a polynomial of an arbitrary degree instead of a piece-wise constant function in finite volume methods.

Reed and Hill in 1973 introduced the first discontinuous Galerkin method for solving linear transport equations. Around the same time and in an independent path, the interior penalty (IP) discontinuous Galerkin methods has been introduced. Nitsche in 1971 first presented penalty terms to weakly impose the boundary conditions in finite element spaces. Generalizing the penalty techniques in the same manner for the enforcement of continuity between elements lead to the development of interior penalty (IP) methods for parabolic and elliptic equations (Arnold,

1982; Babuska, 1973; Babuška and Zlámal, 1973; Percell and Wheeler, 1978; Wheeler, 1978). Another formulation of DG methods for elliptic problems was developed using a mixed formulation. These methods, called local discontinuous Galerkin (LDG), introduce a discontinuous approximation for both p and ∇p (Bassi and Rebay, 1997; Cockburn and Shu, 1998). The basic idea in mixed methods is to solve for the unknown and its flux simultaneously, instead of solving for the pressure and obtain the fluxes in a post-processing step. See the work of Arnold et al. (2002) for a unified analysis of DG methods for elliptic problems.

In the last two decades, DG methods have gone under massive developments and have risen their position in numerical modelling methods. DG methods have some important properties which made them popular in many fields of applications including flow and transport in porous media. The order of the approximating polynomials can vary from one element to the next one because there is no continuity constraint in basis functions between the elements. The order of accuracy only depends on the exact solution, and as a result, a higher order of accuracy can be achieved by increasing the degree of the approximating polynomials. DG methods are highly parallelizable and can handle hp-adaptive strategies, either h-refinement, the increase in the spatial resolution or p-refinement, the increase in the order of approximation. They do not have any constraint regarding the continuity between elements, so they allow the use of general meshes with arbitrary shapes of elements in domains with complex geometries. Another important property is their local mass conservation as it reflects the physical nature of the processes that are being modelled. This property is difficult to hold in high-order finite element methods.

Discontinuous Galerkin methods are flexible and can be coupled with other discretization schemes like more computationally efficient FV methods. This important feature allows engineers to use different methods in different parts of the computational domain and especially implement the DG scheme in the subdomains of interest. DG methods can be applied to a wide range of problems, from hyperbolic to parabolic and elliptic equations. Thanks to the discontinuity of the approximating functions, they can handle strong discontinuous coefficients, which makes them an attractive scheme for flow and transport in porous media. Many researchers have applied DG methods to flow simulations in porous media, from early works of Riviere et al. (2000) in single-phase flows to its extension in multiphase flow processes in the works of Riviere

and Wheeler (2002), Bastian and Riviere (2004), and more recent works of Lee and Wheeler (2018) Fabien et al. (2018), and Cappanera and Riviere (2019), just to mention a few.

However, one of the main drawbacks in DG methods is their high number of degrees of freedom associated with the discontinuity between elements and the duplication of nodes at the interfaces. The higher number of degrees of freedom compared to the classical finite element and finite volume methods lead to larger memory and computational time. One approach to speed up the DG computations is to use hybridized DG (HDG), which reduces the number of coupled unknowns through an introduction of new unknown traces on the mesh skeleton (Woopen et al., 2014). However, HDG implementations can be challenging, as their construction depends on the type of the equations.

3.3 Flow diagnostic tools

Another approach to have a better understanding of flow patterns is simple approximation techniques, called "flow diagnostic tools". These class of methods, relying on simpler flow settings, single-phase or steady-state flows, are less computationally expensive compared to a full simulation of multiphase flows using standard or advanced discretization methods. Thanks to this important feature they can be very useful for obtaining qualitative and quantitative information. Here, we briefly review streamline methods, one of the main flow diagnostic tools.

Since the early works of Muskat and Wyckoff (1937), several authors applied streamline-based methods in different applications. Considering a velocity vector field $\boldsymbol{v}$ at a given time, streamlines are a set of curves that are locally tangential to this velocity field at each point and show the direction of the flow at these points. An example is shown in Figure 3.2. One of the key concepts in streamline simulations is the decoupling of a multi-dimensional problem to a set of one-dimensional problems, thanks to the time-of-flight formulation. Time-of-flight (TOF) is the time it takes for a neutral particle to travel along a streamline. This transformation of coordinates along with the use of the TOF to represent the distance, make this method a powerful tool in many fields of applications. Streamline-based methods can be used as a multi-dimensional single and multiphase flow simulator (Batycky et al., 1997), a powerful diagnostic tool in ranking geostatistical models and upscaling (Ates et al., 2005; Idrobo et al., 2000; Shook and Mitchell,

2009), and an evaluation tool in waterflooding efficiency (Datta-Gupta and King, 2007; Izgec et al., 2011; Thiele and Batycky, 2003), history matching (Yin et al., 2011), flood surveillance (Batycky et al., 2008), and front tracking (Berre et al., 2002; Bratvedt et al., 1992). See the book of Datta-Gupta and King (2007) and the work of Al-Najem et al. (2012) for a review on the development and the detailed mathematical formulation of streamlines.

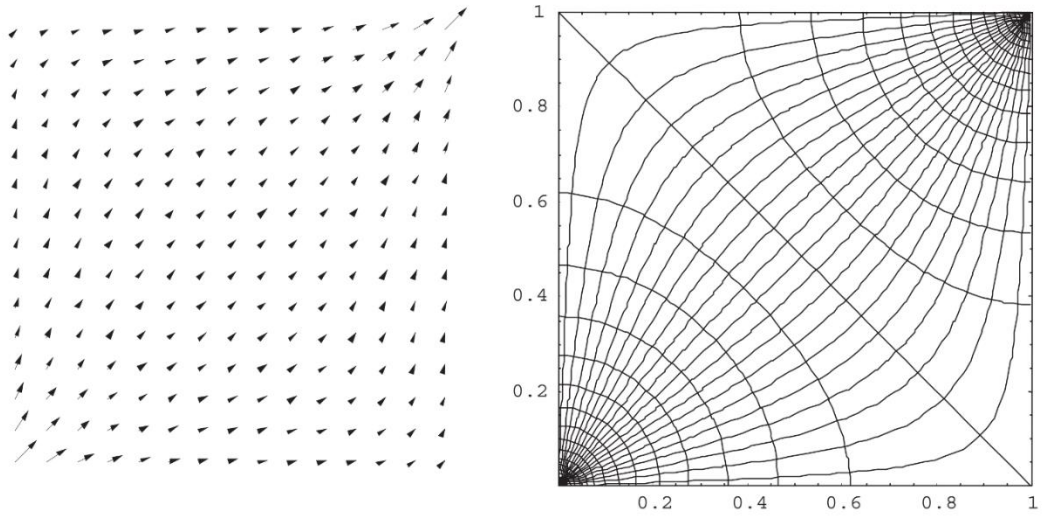

Figure 3.2: Velocity field on the left plot, streamlines and iso-potential lines on the right plot, in a homogeneous quarter five-spot pattern for single-phase incompressible flow (Datta-Gupta and King, 2007).

A streamline simulation is a sequential approach, in which the pressure and saturation equations are decoupled and solved separately at each time step. After solving the pressure equation implicitly, the instantaneous velocity vectors are generated to be used to map the streamlines. Once the streamlines are defined, the fluid flow problem is reduced into 1D problems over streamlines. The solution obtained on the streamlines is then transmitted to the original grid to account for the saturation. This loop is repeated at each time step (Al-Najem et al., 2012).

One of the main limitations of streamline-based approaches is their application in more general non-orthogonal and unstructured grids (Shahvali et al., 2012). Among other flow diagnostic tools, we can mention the works of Shahvali et al. (2012) and Møyner et al. (2015).

3.4 Upscaling

As argued before, even with high computational power, numerical solution of the governing equations on the high-resolution geostatistical models is not feasible, because of the high uncertainties due to the limited amount of available data and the growing need for simulations with multiple realizations of the same reservoir. Therefore, it is customary to use an equivalent model with a lower resolution and fewer parameters that represent the high-resolution model in an averaged sense. In the following, we review upscaling, the process of propagating the properties from a fine grid model to a coarser one, in single-phase and multiphase flows.

3.4.1 Single-phase upscaling

The main goal of upscaling in single-phase flow problems is to find an equivalent value of the non-additive property, the absolute permeability. Single-phase flow is mainly described with the mass conservation and Darcy's law, Eq. 2.5. The main objective of any single-phase upscaling is to find an equivalent k^* such that the solution of this equation at the coarse scale is close to its fine solution, in an averaged sense. This problem is difficult except for very special cases. For most general cases, there is no exact solution and the upscaled permeability values depend on the flow boundary conditions and the discretization of the reservoir. Extensive reviews of existing permeability upscaling methods can be found in the works of Durlofsky (2005, 2003, 1991), King et al. (1995), Renard and Marsily (1997), Wu et al. (2002), Farmer (2002), and Dagan et al. (2013).

For some special cases, the upscaled properties can be calculated using mathematical theories without dependence on the equivalence criteria. Homogenization is a mathematical theory that gives a framework for suppressing high-frequency details from a partial differential equation (PDE) with an oscillating coefficient, producing another PDE with homogenized coefficients (Hornung, 1997). The homogenization theory has a rigorous mathematical foundation if the underlying heterogeneous porous medium presents a wide separation of scales and spatial periodicity. In other words, the homogeneous upscaled equation emerges, when there exists a periodic REV with a characteristic length scale much smaller than the length scale of the medium under study. This approach is applicable only for systems with these strong hypotheses,

but within this framework, it provides a powerful tool to determine both the parameters and the large-scale equations. The assumption of periodicity allows the study of the domain to be replaced by the study of the basic cell subjected to periodic boundary conditions. The assumption of the small ratio of the characteristic length scale of the REV to the length scale of the medium makes it possible to ensure that the large-scale equation emerges (Hornung, 1997).

We do not detail the formulation, but the homogenized single-phase flow equation, after some analysis, is of the form:

$$-\nabla.\left(k_{eff}\nabla p_0\right) = q \qquad \text{Eq. 3.10}$$

with p_0 the zeroth-order approximation of the pressure. k_{eff} is the effective permeability tensor that does not depend on the boundary conditions (Amanbek et al., 2017).

As it is seen, the form of the equation in the single-phase flow case keeps the same form after homogenization. This theory makes it possible to determine both the parameters and the large-scale equation, free of any discretization issue. Discretizing the large-scale equation using a coarse grid can be treated as a separate issue. A schematic representation of the application of the homogenization theory in upscaling is shown in Figure 3.3.

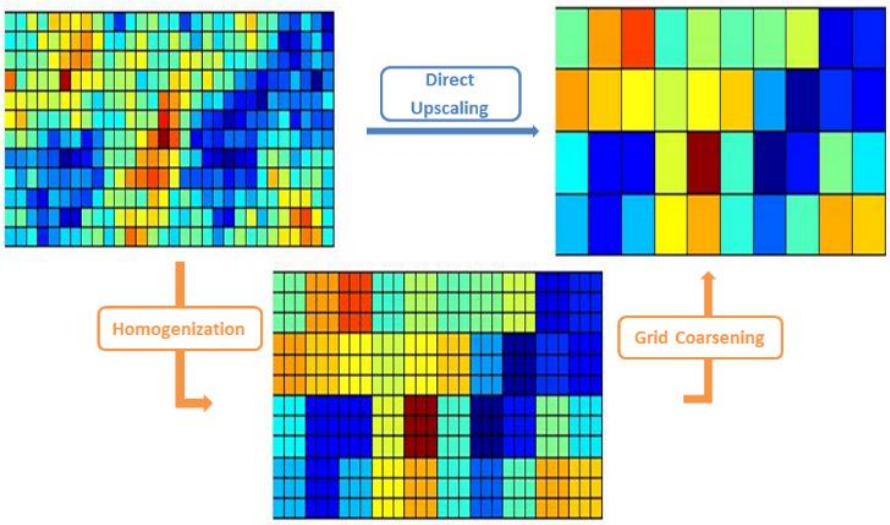

Figure 3.3: A schematic representation of the application of homogenization theory in upscaling.

The main conclusion of the homogeneous equation methods is that at large scales, the low-frequency components of the flow are driven by an effective Darcy's law, characterized by an effective permeability that depends on the details of the small-scale permeability. Another very important advantage of this theory is to show that the flow equation at the coarse scale takes the same form as the flow equation in the REV scale. However, regarding the application of homogenization theory for deriving the upscaled equations and coefficients, the extreme assumptions of the periodicity of the medium should be considered. In practical cases, these assumptions are rarely met. Therefore, it is more common to use more physical upscaling methods, briefly reviewed in the following.

3.4.1.1 **Local methods**

In local methods, the upscaled permeability in each coarse grid block is solely restricted to the effect of the underlying permeability within the grid block. This class of methods can be further divided into analytical averaging and numerical flow-based methods.

3.4.1.1.1 **Averaging methods**

Averaging methods are one of the simplest ways to compute the upscaled permeability. Deutsch (1989) proposed the use of a power averaging method to compute the upscaled permeability for each coarse grid block Ω_i:

$$k^* = \left(\frac{1}{|\Omega_i|} \int_{\Omega_i} k(\boldsymbol{x})^P ds \right)^{\frac{1}{P}} \qquad \text{Eq. 3.11}$$

with power P in the interval between -1 and +1, corresponding to the harmonic and arithmetic averages, respectively. In general, P depends on the spatial distribution of permeabilities and can be found by calibration with the fine-scale results. The power averaging method is motivated by the Wiener inequality or the so-called fundamental inequality (Wiener, 1912), which states that the upscaled permeability in a statistically homogeneous domain is always bounded by its harmonic and arithmetic means.

The main drawback of the analytical methods is their limited range of applications. In some special cases, for example in the perfectly stratified isotropic media, there is an exact analytical upscaled permeability. These correct upscaling methods are harmonic averaging for the case of perpendicular layers to the direction of the flow and arithmetic averaging for the parallel case. However, in most general cases, using analytical approaches involves some risks.

3.4.1.1.2 **Flow-based methods**

In flow-based numerical methods, fine-scale simulations are used to compute the upscaled values. One approach is to perform fine-scale simulations on subdomains, corresponding to the coarse grid blocks, separately and use the resulting fine pressure and total flux values to compute the equivalent permeabilities. One important question in this class of methods is the appropriate boundary conditions. One common approach is to use constant pressure boundary conditions on the two faces in the direction of the flow, for example, $p = 1$ on the inlet face and $p = 1$ on the outlet face. A no-flow condition is usually implemented on the other faces. An illustration of this method is shown in Figure 3.4 for one coarse grid block. By changing the direction of the flow, the upscaled permeability can be calculated for the three main directions, using:

$$k_x^* = \frac{Q_x L_x}{A_x \Delta P_x}, \qquad k_y^* = \frac{Q_y L_y}{A_y \Delta P_y}, \qquad k_z^* = \frac{Q_z L_z}{A_z \Delta P_z} \qquad \text{Eq. 3.12}$$

Here, Q_x is the total flux over the face of the area $A_x = L_y \times L_z$, L_x is the length of the block, and ΔP_x is the pressure drop in the flow direction.

This method was introduced by Warren and Price (1961) and Begg et al. (1989). The problems of this approach, as already mentioned, is related to the choice and validity of the boundary conditions. The no-flow boundary conditions are truly valid only in symmetric cases where the coarse block is bounded by its mirror images, which is far from the real reservoir models in most cases. Another approach is to set a constant pressure on these faces that are perpendicular to the flow direction, allowing the flow to leave or enter the domain (Guerillot et al., 1990). Using periodic boundary conditions is another popular alternative (Durlofsky, 1991). Some choices of boundary condition are discussed in King and Mansfield (1997).

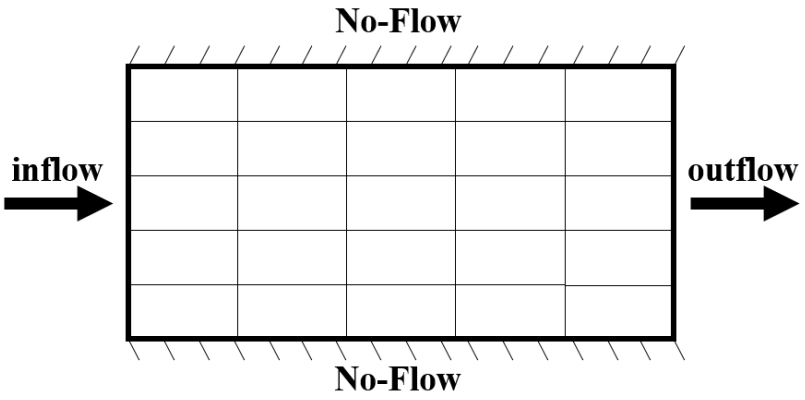

Figure 3.4: An illustration of a local flow-based upscaling method. In this 2D example, the flow direction is set to x-direction while a no-flow condition is set on the y-direction.

The same method of upscaling can be used to directly compute the upscaled transmissibility values at the interfaces of the coarse grid (Peaceman, 1997; White and Horne, 1987). The coarse transmissibility is computed such that it reproduces the averaged flux through faces:

$$v_{ij} = T_{ij}^{*}\left(\frac{1}{|\Omega_i|}\int_{\Omega_i} p d\boldsymbol{x} - \frac{1}{|\Omega_j|}\int_{\Omega_j} p d\boldsymbol{x}\right). \qquad \text{Eq. 3.13}$$

Here, T_{ij}^{*} represents the upscaled transmissibility for the coarse face σ_{ij} and v_{ij} is the total flux over the same face, computed in a fine-scale simulation. The same challenges related to the boundary conditions exist in this approach. Another unpleasant surprise is the appearance of negative transmissibility values that have been discussed in the literature (Wu et al., 2002).

Some authors like Gómez-Hernández and Journel (1990) and Hou and Wu (1997a), proposed the "oversampling" technique to reduce the boundary conditions impacts and to improve the final result of the upscaling. This technique, as its name suggests, recommends solving the fine-scale flow problem in a region larger than the coarse block. Figure 3.5 shows a simple schematic of the oversampling technique.

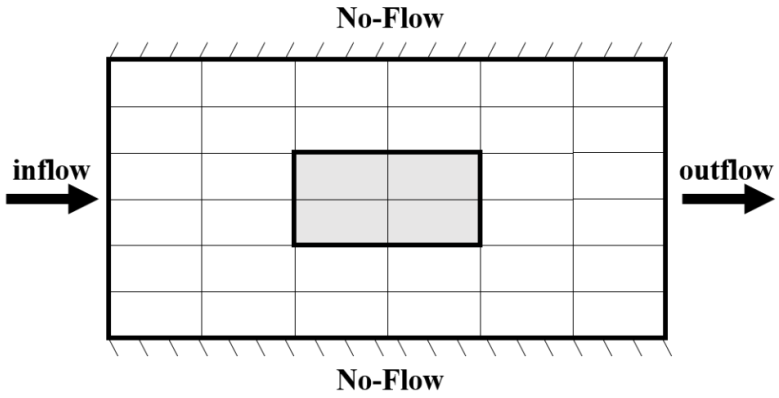

Figure 3.5: An illustration of the oversampling technique for the local upscaling method.

3.4.1.2 **Local-global methods**

In this class of methods, a global-scale solution is known over the whole domain and this information is used to solve a local upscaling problem. One approach is to solve a flow problem over the whole domain on a coarse grid, and use the approximated pressure as boundary conditions for the local flow problem over each coarse grid block, as described in the previous section (Chen et al., 2003; Chen and Durlofsky, 2006; Gerritsen and Lambers, 2008). This method usually is done in an iterative procedure to overcome the problem of poor coarse-scale boundary conditions to solve a fine-scale flow equation. Among other variations of this method, we can mention the works of Chen and Durlofsky (2006), Alpak et al. (2012), and Alpak (2015).

3.4.1.3 **Global methods**

These methods use the fine-scale solution on the base geological model to compute the upscaled properties, permeabilities or transmissibilities. White and Horne (1987) were the first ones to propose a global upscaling method. Their approach is to solve the flow equation on the original geological grid a few times with a set of different global boundary conditions and to compute the coarse-scale pressure and total flux values using the volume-averaging and integration over faces, respectively. Having these coarse-scale fluxes and pressures and using a coarse-scale Darcy's law for each face in the coarse grid, the upscaled transmissibility tensor can be computed using:

$$v_{ij} = T_{ij}^{*}(p_i - p_j). \qquad \text{Eq. 3.14}$$

Another approach in this class of methods tries to compute the upscaled properties such that it minimizes the difference between global fine and coarse pressure and flux fields (Holden and Nielsen, 2000). An alternative approach that does not need the fine-scale solution was proposed by Nielsen and Tveito (1998). These methods may be the most computationally expensive among all upscaling methods, but they do not need any assumption on local boundary conditions. However, they depend on prior knowledge of the global boundary conditions or drive mechanisms. Once these conditions change, the upscaled properties may not be valid or accurate.

3.4.2 **Multiphase upscaling**

The challenge in upscaling becomes more critical in multiphase flows. Multiphase upscaling is much less developed than single-phase upscaling, that is now routinely carried out. Generally, the upscaling of absolute permeability alone cannot model a multiphase process in a heterogeneous medium and may lead to incorrect oil recovery and water breakthrough times in reservoir simulations and becomes more severe in presence of high-permeability channels or extensive flow barriers (Muggeridge, 1991). Multiphase flow models generally include a generalized Darcy's law, where the relative permeability is introduced in the equation, and a mass conservation equation for each phase, Eq. 2.16 and Eq. 2.17.

As mentioned previously, homogenization of single-phase flow equations leads to equations of the same form, with effective permeability values which are the same as flow-based local upscaled permeabilities with linear boundary conditions. But in the two-phase flow case, the situation is different if there are different saturation functions in different fine grid cells (Farmer, 2002). In some special cases, for example, where the capillary pressure and relative permeability curves do not change over the whole domain, the homogenized equations keep the same form as the original two-phase flow equations with an upscaled permeability tensor (Amaziane, 1993; Bourgeat, 1997; Saez et al., 1989). However, in most cases, the homogenized two-phase flow equations are not of the same form as their original ones. One conclusion of homogenization theory can be that upscaling approaches developed for single-phase flow models cannot be directly applied to multiphase flow models.

3.4.2.1 **Pseudo functions**

A well-known method for upscaling of multi-phase flow problems is the use of dynamic pseudo relative permeabilities to reproduce the results of a given fine grid simulation on a coarse grid. This method was initially proposed for correcting numerical dispersion effects by Kyte and Berry (1975), at a period in which simulations were carried out using a few grid blocks inducing high numerical dispersion that needed to be corrected. Since then, several approaches have been proposed to generate these pseudo-functions, in which a two-phase process is simulated on the fine grid and the results are used to calculate pseudo relative permeabilities at a coarser scale, using the volume-averaged fluxes for each phase and assuming that the type of flow equations remains the same. One approach is first, to calculate the average fine pressures for each coarse grid block, and the integrated fine-grid fluxes of each phase over each face in the coarse grid. Then, Darcy's law at the coarse scale is used to compute the coarse grid pseudo relative permeability values (Kyte and Berry, 1975). However, in practice, this method may lead to a negative or an infinite pseudo relative permeability value (Barker and Dupouy, 1999; Stone, 1991).

Another approach, first suggested by Stone (1991), is to use the total mobility to obtain the pseudo relative permeabilities directly from the average fractional flow and the average total mobility, in the absence of capillary and gravity effects. However, this method is inadequate where there are significant variations in total mobility (Barker and Fayers, 1994). Another limitation is the assumption of no capillary and gravity effects. This method, as well, may lead to negative values (Barker and Dupouy, 1999). Some authors like Barker and Fayers (1994), and Hewett and Behrens (1991) proposed to improve Stone's method using better definitions of the average total mobility. But still, they may fail to reproduce the fine grid solution on a coarse scale.

Several other pseudo relative permeability methods have been proposed to overcome these drawbacks, but it has been shown that there are practical limitations in using pseudo relative permeabilities, independent of the approach to compute them (Barker and Dupouy, 1999; Barker and Thibeau, 1997; Christie, 1996; Darman et al., 2002). The key problems related to the use of pseudo-functions in upscaling of multiphase flows from a fine grid geological model to a

coarse grid simulation model include the dependence of results on the location of coarse blocks, the flow direction, and boundary conditions. Another problem is the need for some grouping techniques to decrease the large numbers of relative permeability functions. All these challenges lead to practical difficulties with the use of pseudo-functions that extensively discussed by Barker and Thibeau (1997), and Darman et al. (2002). The difficulty with pseudos and other multiphase upscaling classical methods is that they mix homogenization issues with numerical discretization issues. The net result is a quite unclear and un-controllable mix of techniques. Starting from a completely homogeneous medium leads to pseudos that may not simply return the input properties of the medium. On the contrary, homogenizing a homogeneous medium recovers the input properties, as it should. This means that pseudo properties mix averaging and scale effects as does homogenization, and specific effects due to details of the underlying discretization. The net result gives a somewhat un-understandable property. One gets a set of pseudo relative permeabilities per coarse scale that is not manageable by reservoir simulators, and somewhat erratic variations of k_r with local saturation that can lead to numerical instabilities while performing the coarse-scale simulation.

3.5 Alternative approaches

Due to the mentioned practical difficulties in multiphase cases, the upscaling is only limited to permeability upscaling in the energy industry (Audigane and Blunt, 2004). Single-phase upscaling, even though being "*the best-understood form of upscaling*" (Christie, 1996), does not have an unequivocal solution. This has been a motivation for research on alternative approaches to accelerate flow simulations. Some of these approaches are reviewed shortly in the following.

3.5.1 Dual grid techniques

Rame and Killough (1991) were first to propose to use different grids to solve pressure and saturation equations and presented an approach for immiscible multiphase flows. Verdière et al. (1996) proposed a dual mesh method that uses a sequential algorithm by solving the pressure equation on a coarse grid and the saturation equation on a fine one. At each time step, the pressure equation can thus be solved using upscaled permeability values. Audigane and Blunt

(2004) extended this work to three-dimensions in the presence of gravity effects and wells. A schematic of this approach is shown in Figure 3.6. A reconstruction step is required to determine fine-scale velocities from the coarse-scale solution (step 4 in the figure). This method can be attractive, as it provides fast and accurate results because of solving only the saturation equation on the fine grid. But one limitation of this method is that the reconstruction of fluxes from the coarse grid to the fine grid is not robust.

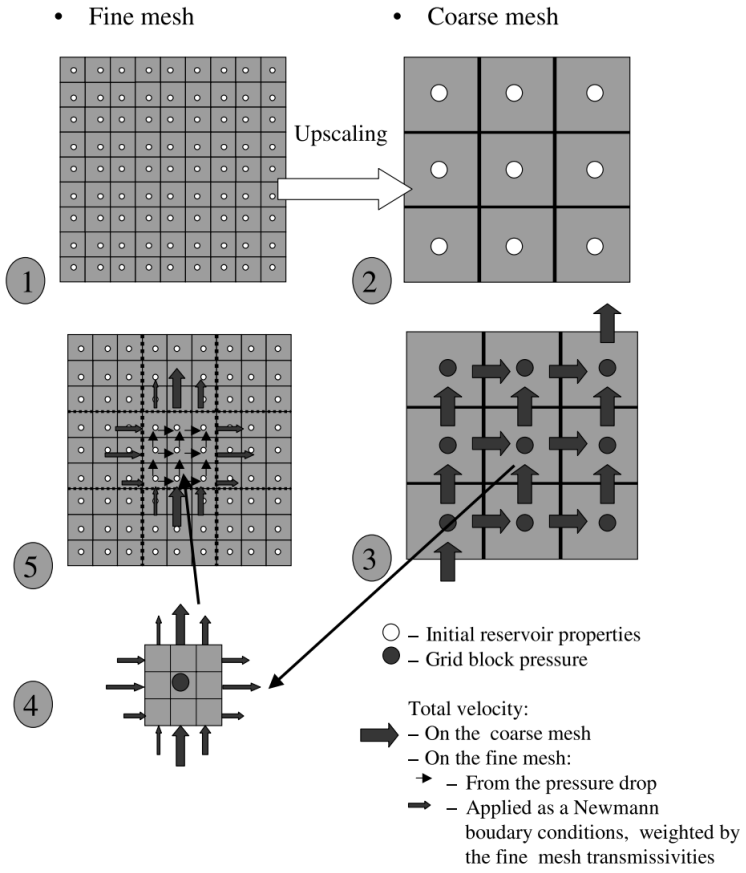

Figure 3.6: A schematic of the dual mesh method algorithm (Audigane and Blunt, 2004). The reconstruction of fluxes in step 4 is the main challenge in this method.

3.5.2 **Multiscale methods**

These class of methods aim at systematically capturing the effects of fine-scale heterogeneities in the coarse-scale model. Hou and Wu (1997b) first proposed the idea of a multiscale finite element method, where the base functions are constructed to capture the fine-scale information. Soon after, the multiscale solvers have been developed for finite volume methods, MsFV (Jenny et al., 2005; Jenny et al., 2003), as well as mixed finite element methods,

MsMFE (Aarnes et al., 2005; Aarnes, 2004). In these methods, basis functions are constructed numerically on a local flow problem in dual coarse grid blocks (see Figure 3.7). Once the flow equations are solved on the coarse grid, the fine-scale solution can be approximated using the basis functions (Lie et al., 2017c). Kippe et al. (2008) compared extensively the finite element and finite volume multiscale with upscaling methods.

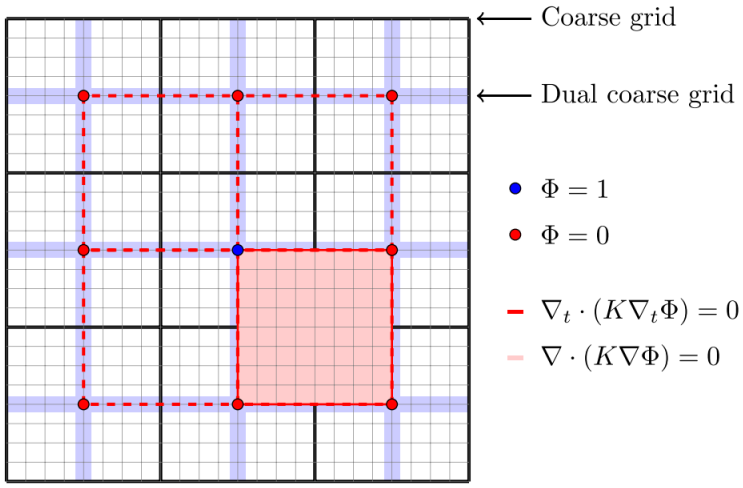

Figure 3.7: Representation of basis functions for FV multiscale methods. Basis functions are computed by solving local flow problems in the dual coarse grid (Lie et al., 2017c).

3.5.3 **Adaptive gridding**

The basic idea of using non-uniform grids in flow simulations in porous media is not new in the energy industry. Adaptive gridding techniques have been followed in two different ways, the techniques based on refinement and the techniques based on coarsening. The local grid refinement (LGR) techniques add more spatial resolution by dividing the coarse grid blocks in a structured manner. An illustrative example of an LGR method is shown in Figure 3.8. The use of adaptive or non-uniform gridding in multiphase flow simulations in porous media goes back to 1980s. Von-Rosenberg (1982) implemented a local grid refinement for finite difference methods with the unit mobility ratio and Quandalle (1983) extended it to variable mobility ratios. Dynamic versions of it were developed in the works of Heinemann et al. (1983) in two-dimensional cartesian grids with a limitation on the level of refinement and Han et al. (1987) with more improvements in terms of subdivisions and refinement levels. Since then, many improvements have been made in this method in the works of Sammon (2003), Christensen et al. (2004) and van

Batenburg et al. (2011), to mention a few. A similar approach is the adaptive mesh refinement, introduced in the work of Berger and Oliger (1984), where a finer resolution grid is placed over the coarse blocks with discontinuities or shocks. A local time step is defined to solve the equations on the refined blocks with the boundary conditions from the coarse grid.

The difference in various LGR methods usually lies in the answer to question 'where and when to add refinement'. van Batenburg et al. (2011) reviewed and compared some of the local refinement techniques in terms of implementation and criteria. What all these methods have in common, generally, is that they consist of a refinement step and an un-refinement or coarsening step. More importantly, in general, the geological model is not preserved in the process, and the approach to increase the solution accuracy is through decreasing numerical diffusion. Hoteit and Chawathé (2016) tried to overcome this limitation by storing the fine-scale rock properties in their proposed local refinement approach.

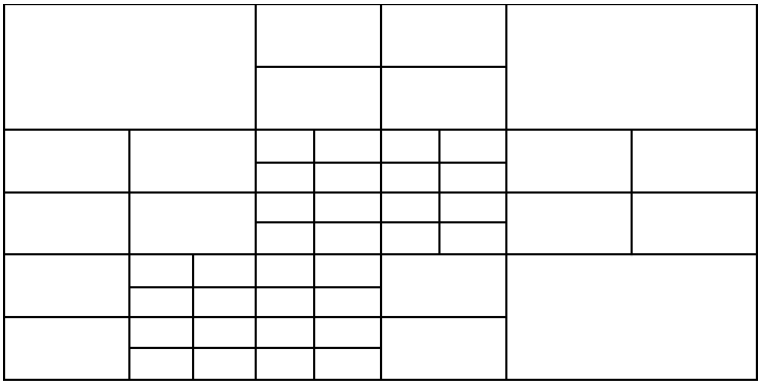

Figure 3.8: An example of a local grid refinement with three refinement levels.

Another class of adaptive gridding techniques is non-uniform coarsening methods. Durlofsky et al. (1997) clearly showed the advantages of generating a non-uniform coarse grid that adapts to high-velocity zones. An important key to the development of these methods is the agglomeration-based coarsening, first proposed by King et al. (2006). These methods do not generate the coarse grid explicitly, but instead, create a partition vector over the original resolution grid to represent the relation of the coarse grid to its original high-resolution grid. This partition vector (π) is an integer value vector such that $\pi(c) = b$ if cell c in the fine grid belongs to block b in the coarse grid. An illustration is shown in Figure 3.9.

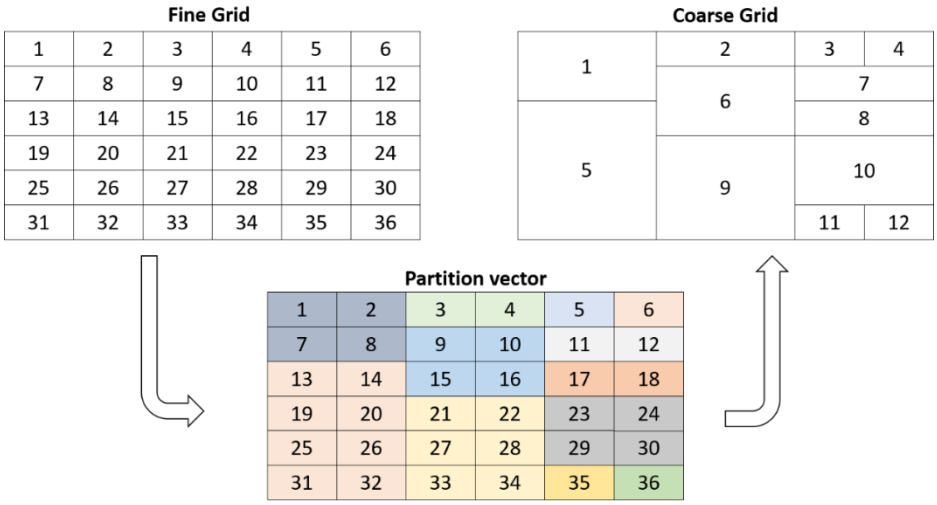

Figure 3.9: A simple example of agglomeration-based coarsening. In this example, the partition vector is shown in terms of colours. The fine grid cells with the same colour belong to the same coarse grid block.

Many authors have developed non-uniform coarsening approaches to better capture the underlying heterogeneity of original fine model (Aarnes et al., 2008; Alpak et al., 2012; Lie et al., 2017b; Natvig et al., 2012), or to better adapt to flow patterns in order to increase the accuracy of transport solvers (Aarnes et al., 2007b; Hauge et al., 2012, 2010), or finally to generate reduced-order models using non-uniform coarsening and flow-based single-phase upscaling (Guion et al., 2019; Karimi-Fard and Durlofsky, 2016; Lie et al., 2017a; Lie et al., 2014). The flow-based coarsening methods, like the method of Aarnes et al. (2007b), are an improvement of the work of Durlofsky et al. (1997) to a general framework to create non-uniform coarse grids with arbitrary shape while minimizing the constraints. This approach needs the conditions of cell connectivity and mass conservation of the velocity field to be met. They use the flow magnitude to detect high and low flow regions and create partition vectors. In its dynamic version, the original fine grid is always present in the simulation. For example in the works of Hauge et al. (2012), they developed a flow-based coarsening approach for multiscale simulations. They improved the coarsening approach of Aarnes et al. (2007b) to generate a less-irregular grid and include a priori geological heterogeneity information and provided an adaptive coarsening approach.

One of the main challenges in adaptive gridding approaches is the criteria to add resolution, either in terms of adding subdivisions or non-uniform coarsening. Classical criteria in

the literature are usually based on the spatial or temporal gradient of the values of phase saturations or concentrations (van Batenburg et al., 2011).

3.6 Localization of the saturation discontinuity

As mentioned before, capturing the instabilities at the front is important in reaching an accurate solution in immiscible multiphase flows in porous media. In adaptive gridding approaches, different criteria, using different techniques, generally try to identify the multiphase region in the vicinity of the front and increase the mesh resolution in this region to capture the interactions of medium heterogeneity and viscous fingering. Here, we will review some of the existing methods for modelling the saturation discontinuities.

3.6.1 Front tracking methods

The term "front tracking" refers to a class of methods that treat discontinuities in the solution, including shocks (Holden and Risebro, 2015). In reservoir numerical simulations, Glimm and his co-workers developed a front tracking method for hyperbolic conservation laws (Glimm et al., 1983; Glimm et al., 1981, 1980). In their approach, the position of shock waves is simulated separately through the introduction of these discontinuities as independent computational entities with a degree of freedom. Away from the front, classical numerical methods, like finite difference methods, are implemented to solve the conservation law. Having the initial saturation discontinuity, this approach computes the time evolution of the front during the simulation. The velocity of propagation of the front is determined using the mass conservation law and Rankine-Hugoniot equation. The time step is the same as the one used in the transport solver in the main sequential scheme. The front speed is calculated from the method of characteristics. Solving a Riemann problem normal to the front:

$$\frac{\partial s}{\partial t} + v_n \frac{\partial}{\partial n} f_w(s) = 0 \qquad \text{Eq. 3.15}$$

where v_n is the normal component of the velocity and $\partial/\partial n$ indicates the normal derivative (Glimm et al., 1981). It should be noted that the normal component of the velocity in the Riemann problem is continuous. The characteristic speed of the shock front is entered in this

equation. It should be noted that in the limit of vanishing capillary pressure, the saturation is discontinuous at the front. So the transport equation is to be understood in the sense of generalized functions, with the appearance of both standard derivatives and delta-like functions corresponding to the front location. The singular part involving delta functions can be rewritten under the more familiar following form:

$$\left.\frac{d\boldsymbol{x}(s_f)}{dt}\right]_{front} = v_n \qquad \text{Eq. 3.16}$$

where $\boldsymbol{x}(s_f)$ denotes any position vector along the front. Daripa et al. (1987) present an overview of the front tracking model developed by the authors and a series of tests in reservoir simulations.

As mentioned, this front tracking method uses a separate scheme to treat the sharp front and a classical discretization method to solve the saturation equation elsewhere. There exist another class of front tracking methods that do not involve a standard discretization method. This class of methods consider all saturation waves as discontinuities. The saturation profile is not considered as a continuous function with one sharp front, but instead a piecewise constant function with discrete fronts (Bratvedt et al., 1992; Bressan, 1992; Holden and Risebro, 2015; Lie and Juanes, 2005; Risebro, 1993). This class of methods are based on the exact and approximate solutions of hyperbolic conservation laws of the form:

$$\frac{\partial s}{\partial t} + \frac{\partial \boldsymbol{F}_w(s)}{\partial \boldsymbol{x}} = 0 \qquad \text{Eq. 3.17}$$

where $\boldsymbol{F}_w = f_w \boldsymbol{v}$. The Riemann problem is a type of initial value problem where the initial state is given in the form of a piecewise function:

$$s_0(\boldsymbol{x}) = \begin{cases} s_L, & \boldsymbol{x} < 0 \\ s_R, & \boldsymbol{x} \geq 0 \end{cases} \qquad \text{Eq. 3.18}$$

Solutions of Riemann problem, exact or approximations, are important in front tracking methods. For a constant piecewise initial data, there exist exact analytical solutions. Starting from a piecewise approximation of the initial data, a series of Riemann problems are defined and

solved independently until they interact with the other discontinuities. Refer to the book of Holden and Risebro (2015) for a thorough overview of this class of front tracking methods.

One of the challenges in front tracking methods is their extension to three-dimensional numerical modelling. Glimm et al. (1998) performed a feasibility analysis for front tracking in 3D and offered some solutions. Another solution, proposed in the work of Lie and Juanes (2005) is to combine front tracking methods with streamline simulations. Streamline simulations, as mentioned, work based on decoupling three-dimensional problems into a set of one-dimensional problems, which can be solved using the front tracking method. They presented their approach in three-dimensional three-phase simulations. Some other implementation issues in front tracking methods were discussed by Langseth (1996).

3.6.2 **Level set method**

The level set method was originally introduced by Osher and Sethian (1988), by defining a signed distance function $\varphi(\mathbf{x},\mathrm{t})$ for tracking the evolution of the front Γ with a given speed of F. This level set function, $\varphi(\mathbf{x},\mathrm{t})$, has an important property; the zero level-set gives the front, i.e., $\Gamma(\mathrm{t}) = \{\mathbf{x}|\ \varphi(\mathbf{x},\mathrm{t}) = 0\}$. The motivation behind this method is that moving the level set functions are easier to model, even at a cost of increasing the dimension of the problem by one. Figure 3.10 shows a level set function of a 2D front. The function φ at each point is set to be the shortest distance from the point to the front at time t (Sussman et al., 1994):

$$\begin{cases} \varphi(\boldsymbol{x},t) = +d\,, & \boldsymbol{x} \in \Omega \\ \varphi(\boldsymbol{x},t) = -d\,, & \boldsymbol{x} \in \overline{\Omega} \\ \varphi(\boldsymbol{x},t) = 0\ , & \boldsymbol{x} \in \partial\Omega \end{cases} \qquad \text{Eq. 3.19}$$

The evolution equation of the level set will be (Osher and Sethian, 1988):

$$\frac{\partial\varphi}{\partial t} + F|\nabla\varphi| = 0 \qquad \text{Eq. 3.20}$$

The level set function φ, is initialized as the signed distance function. However, under the evolution of the equation above, it will not necessarily remain so. Therefore, it is necessary for

later times, to re-initialize, or replace the level set function with a signed distance function while preserving the location of the zero level-set.

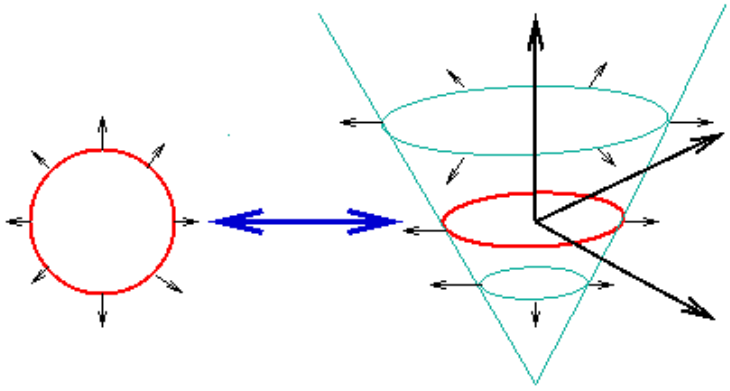

Figure 3.10: Original front in the XY plane (left) and the level-set function in XYZ (right) (Sethian, 1996b).

3.6.3 **Fast marching method**

Sethian (1996a) developed the fast marching method as a special case of the level set method when the front speed is only a function of position and does not change its direction. A new variable $T(\mathbf{x})$ or the arrival time is introduced. The $T(\mathbf{x})$ measures the time at which the front reaches the position $\mathbf{x}$, i.e., $\varphi(\mathbf{x}, \mathrm{T}) = 0$. The arrival time satisfies the "*stationary Eikonal equation*":

$$F.\nabla T = 1. \qquad \text{Eq. 3.21}$$

In other words, the gradient of the arrival time function is inversely proportional to the speed of the front. Knowing the position $\mathbf{x}$ and speed function F at this position, T will provide the time at which the front reaches $\mathbf{x}$. Sethian (1996a, 1996b) provided an algorithm, called the fast marching method, to solve the Eq. 3.21. This conversion from a general level set to a stationary formulation is an important characteristic which made the solution approaches very fast. For a detailed formulation and solution algorithm, see Sethian (1999).

Karlsen et al. (2000) first applied this fast marching level set method for solving the transport equation in multiphase flow simulations in porous media as a solver faster than standard numerical methods. They continued this work later (Berre et al., 2005) by presenting some

deficiencies of their previous approach, the inaccuracy of the marching algorithm and the calculated arrival times for some cases. They showed why the previously presented level set fast marching method cannot be used to solve the saturation equations in porous media. They also presented an alternative derivation of fast marching methods in close relation with time-of-flight and streamline methods, and a new advancing-front method with more limitations in its application but more accuracy.

4 Discretization methods

Starting from a geostatistical model with the defined rock properties in all grid cells, usually as a result of the statistical propagation of a few measured data, and a fluid model with a system of governing equations, we can simulate fluid flow processes in porous media using different numerical discretization methods and different solution algorithms. In this chapter, we consider discretization of the governing equations of single and immiscible multiphase flows in porous media, described in chapter 2. We detail the finite volume and the discontinuous Galerkin methods and present two-dimensional test cases. For each method, we discuss the numerical errors.

4.1 Finite volume method

4.1.1 Single-phase flow:

As described in chapter 2, the flow equation for a single-phase incompressible flow is:

$$\nabla . \boldsymbol{v} = \nabla . \left(-\frac{k}{\mu} \nabla p \right) = q. \qquad \text{Eq. 4.1}$$

We assume the reservoir domain Ω, with boundary $\partial\Omega$, is partitioned into cells $\{\Omega_i\}$. As mentioned in chapter 3, a common approach to derive a finite-volume discretization is to integrate the flow equation over each grid cell or control volume, Ω_i. Using the divergence theorem, we obtain the mass balance equation for each control volume, which reads (Eymard et al., 2000):

$$\int_{\partial\Omega_i} \boldsymbol{v} . \boldsymbol{n} \, ds = \int_{\Omega_i} q d\boldsymbol{x} \qquad \text{Eq. 4.2}$$

To formulate the standard two-point flux approximation finite-volume scheme, it is necessary to approximate the flux, $\boldsymbol{v} . \boldsymbol{n}$, across faces, σ_{ij}, from values of the two neighbouring cells, Ω_i and Ω_j, on two sides of the face σ_{ij}. Assuming the pressure is linear inside each cell, we write consistent approximations of flux using Darcy's law (Lie, 2019):

$$v_{i,\sigma} = |\sigma_{ij}| \frac{k_i}{\mu} \frac{p_i - p_\sigma}{d_{i,\sigma}}$$

$$v_{j,\sigma} = |\sigma_{ij}| \frac{k_j}{\mu} \frac{p_j - p_\sigma}{d_{j,\sigma}} \qquad \text{Eq. 4.3}$$

where $d_{i,\sigma}$ is the distance from the centre of the cell Ω_i to the centre of the face σ_{ij} and p_σ is the face pressure. A representation of two neighbouring control volumes in a simple two-dimensional Cartesian grid is shown in Figure 4.1. To derive the formulation of the flux across the face in the two-point flux approximation scheme, we impose the conservativity of the fluxes, $v_{ij} = v_{i,\sigma} = -v_{j,\sigma}$, for the interface σ_{ij}, which gives:

$$v_{ij} = |\sigma_{ij}| \left(\frac{d_{i,\sigma}}{k_i} + \frac{d_{j,\sigma}}{k_j} \right)^{-1} \frac{(p_i - p_j)}{\mu} = T_{ij}(p_i - p_j) \qquad \text{Eq. 4.4}$$

where T_{ij} is called face or edge transmissibility and includes the distance-weighted harmonic average of k in the two neighbouring cells Ω_i and Ω_j. The final TPFA scheme to discretize Eq. 4.1 is obtained by writing Eq. 4.2 for all faces in all grid cells with the two-point approximated fluxes of Eq. 4.4, which reads:

$$\sum_j v_{ij} = \sum_j T_{ij}(p_i - p_j) = q_i, \qquad \forall \Omega_i \in \Omega. \qquad \text{Eq. 4.5}$$

Solving this system gives the approximated cell-averaged pressures, $p = \{p_i\}$.

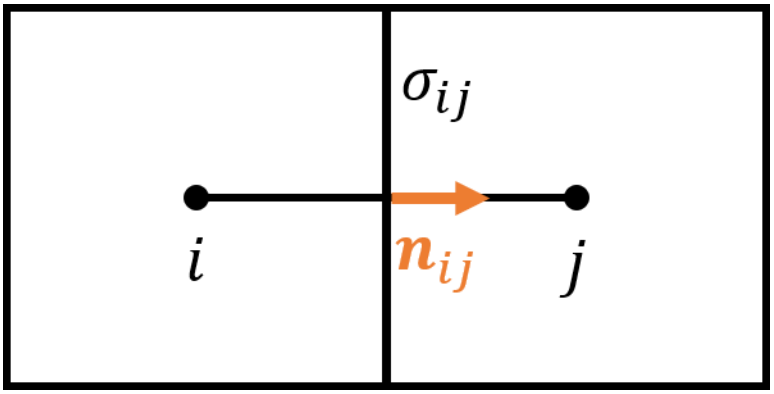

Figure 4.1: Two cells used to derive the TPFA discretization scheme for a 2D Cartesian grid.

4.1.2 **Multiphase flow**

In this section, we consider an immiscible two-phase flow problem with water (w) and oil (o) phases. Already described in chapter 2, the conservation of the volume of each phase, assuming the rock and the fluids are incompressible and in the absence of capillary and gravity forces, is given by:

$$\phi \frac{\partial s_\alpha}{\partial t} + \nabla.(\boldsymbol{v}_\alpha) = q_\alpha, \quad \alpha = o, w \qquad \text{Eq. 4.6}$$

In chapter 2, we detailed how this equation is converted into a flow and a transport equation and we briefly reviewed different approaches of solving this system of equations. The benefits of sequential splitting methods, namely reduced computational time and the possibility to combine different numerical methods, are very attractive in many fields of applications including reservoir simulations. Therefore, we choose this approach in this work. Assume we are at the time n and we want to approximate the solution at time $n + 1$. A simple algorithm for one time-step in a sequential approach is shown in Figure 4.2. At each time step, the values of saturation, pressure, and flux from the current time step, $s^n, p^n, \boldsymbol{v}^n$, are known. Assuming that the impact of mobility, λ_T, on the flow is moderate in time, the flow (pressure) equation is solved to compute pressure and fluxes, $p^{n+1}, \boldsymbol{v}^{n+1}$. Using new fluxes, the transport equation is solved to compute s^{n+1}. In the following, we detail the finite volume discretization of flow and transport equations for immiscible two-phase flows.

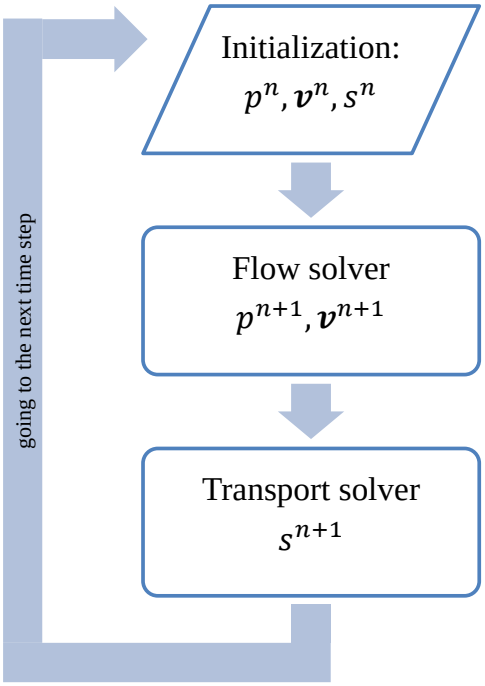

Figure 4.2: A simple flowchart of a sequential approach for each time step.

4.1.2.1 **Discretizing the flow equation**

Recalling from chapter 2, the flow equation for the immiscible two-phase flow is given by:

$$\nabla . \boldsymbol{v} = -\nabla . (k\lambda_T(s_w)\nabla p) = q. \qquad \text{Eq. 4.7}$$

In the sequential approach, we solve the above pressure (flow) equation assuming s is held fixed in time. Therefore, the time-dependent $\lambda_T(s_w)$ becomes position dependant only, and the pressure equation can be solved like a single-phase flow equation, as described in section 4.1.1. The only difference is the introduction of a new variable, the relative permeability. The standard finite-volume two-point flux approximation to discretize the pressure equation gives:

$$\sum_j v_{ij}^{n+1} = \sum_j T_{ij}^n \left(p_i^{n+1} - p_j^{n+1}\right) = q_i^{n+1}, \qquad \forall \Omega_i \in \Omega \qquad \text{Eq. 4.8}$$

where the superscripts n and $n+1$ represent the time step, $p^{n+1} = \{p_i^{n+1}\}$ is the new cell-wise constant approximated pressure, q_i^{n+1} is the volume average of the total source term q over the cell i at timestep $n+1$, and T_{ij}^n is the face transmissibility given by the distance-weighted harmonic average of $k\lambda_T^n$ values in the two neighbouring cells Ω_i and Ω_j:

$$T_{ij}^n = |\sigma_{ij}| \left(\frac{d_{i,\sigma}}{k_i \lambda_{T_i}^n} + \frac{d_{j,\sigma}}{k_j \lambda_{T_j}^n} \right)^{-1}. \qquad \text{Eq. 4.9}$$

The transmissibility depends on time through its implicit dependence on the local saturation at time t^n.

4.1.2.2 **Discretizing the transport equation**

To explain the finite volume discretization of transport equation we first consider a one-dimensional hyperbolic differential equation of the form:

$$\frac{\partial s}{\partial t} + \frac{\partial F(s)}{\partial x} = 0, \qquad s(x,0) = s_0(x), \qquad \text{Eq. 4.10}$$

where F represent the flux function. Partitioning the domain Ω into control volumes Ω_i, where $\Omega_i = [x_{i-1/2}, x_{i+1/2}]$, let $\Delta x_i = x_{i+1/2} - x_{i-1/2}$. To derive the finite volume discretization, Eq. 4.10 is integrated over the grid cell Ω_i:

$$\int_{x_{i-1/2}}^{x_{i+1/2}} \frac{\partial s}{\partial t} dx + \left(F_{i+1/2} - F_{i-1/2} \right) = 0. \qquad \text{Eq. 4.11}$$

$F_{i\pm1/2}$ represent the flux function evaluated at the cell interfaces, which can be approximated as below in the absence of gravity and capillary forces:

$$F_{i\pm1/2} \approx f_w(s)_{i\pm1/2} v_{i\pm1/2}. \qquad \text{Eq. 4.12}$$

$f_w(s)_{i\pm1/2}$ is the fractional flow function, approximated at the cell interface. Denoting by s_i the FV approximation of the average value of the saturation over each control volume Eq. 4.11 gives:

$$\frac{ds_i(t)}{dt} + \frac{1}{\Delta x_i}\left(F_{i+1/2} - F_{i-1/2}\right) = 0, \qquad \text{Eq. 4.13}$$

Considering the time domain $[0, T]$ be partitioned into time steps $\Delta t^n = t^{n+1} - t^n$, an explicit time discretization of Eq. 4.10 is of the form:

$$s_i^{n+1} = s_i^n - \frac{\Delta t^n}{\Delta x_i}\left(F_{i+1/2}^n - F_{i-1/2}^n\right) \qquad \text{Eq. 4.14}$$

And an implicit temporal discretization is of the form:

$$s_i^{n+1} + \frac{\Delta t^n}{\Delta x_i}\left(F_{i+1/2}^{n+1} - F_{i-1/2}^{n+1}\right) = s_i^n \qquad \text{Eq. 4.15}$$

To approximate the flux functions, $f_w(s)_{i\pm1/2}$, a standard approach is the upwind scheme. It is common to write the upwind scheme on the fractional flow using the direction of the fluxes:

$$f_w(s)_{i+1/2} = \begin{cases} f_w(s_i), & if\ v_{i+1/2} \geq 0, \\ f_w(s_{i+1}), & if\ v_{i+1/2} < 0. \end{cases} \qquad \text{Eq. 4.16}$$

Extending the finite volume discretization to a more general multi-dimensional transport equation of the form:

$$\phi \frac{\partial s_w}{\partial t} + \nabla.\left(f_w(s_w)\boldsymbol{v}\right) = q_w \qquad \text{Eq. 4.17}$$

and implementing the so-called θ scheme for temporal discretization, a common form in reservoir simulations, gives:

$$\phi_i \frac{s_i^{n+1} - s_i^n}{\Delta t} + \frac{1}{|\Omega_i|}\sum_{j \neq i}\left[\theta F_{ij}(s_w^{n+1}) + (1-\theta)F_{ij}(s_w^n)\right] = q_i(s_w^n). \qquad \text{Eq. 4.18}$$

where Δt is the time step in the case the time domain is partitioned into equal intervals, s_i is the volume-average of water saturation, ϕ_i is the porosity of cell i, and $|\Omega_i|$ is the volume of cell i. $\theta = 0$ gives the explicit scheme and $\theta = 1$ gives the implicit scheme.

F_{ij}, the approximation of the flux function over the face σ_{ij}, like in 1-D case, is given by:

$$F_{ij} \approx f_w(s)_{ij} v_{ij}. \quad \text{Eq. 4.19}$$

where v_{ij} is the total flux at the face σ_{ij}, coming from the solution of the pressure equation. $f_w(s)_{ij}$ denotes the fractional-flow function associated with the face σ_{ij} and is chosen using the upwind scheme:

$$f_w(s)_{ij} = \begin{cases} f_w(s_i), & if\ v_{ij} \geq 0, \\ f_w(s_j), & if\ v_{ij} < 0. \end{cases} \quad \text{Eq. 4.20}$$

The difference between implicit and explicit discretization schemes is the time at which the saturation dependent fractional flow functions are evaluated.

Explicit schemes are less diffusive than implicit ones, but a Courant-Friedrichs-Lewy (CFL) condition on the time step size is required to guarantee the stability of the saturation solutions (Courant et al., 1928). The CFL condition for Eq. 4.18 with $\theta = 0$ holds whenever the time-step size satisfies the following inequality (Aarnes et al., 2007a):

$$\Delta t \leq \min_i \frac{\phi_i |\Omega_i|}{v_i^n \max\{f_w'(s)\}_{0 \leq s \leq 1}} \quad \text{Eq. 4.21}$$

where v_i^n represents the influxes:

$$v_i^n = \max(q_i, 0) - \sum_j \min(v_{ij}, 0). \quad \text{Eq. 4.22}$$

This condition depends on saturation through total fluxes v_{ij} and needs to be updated each time the pressure equation is solved. This constraint on the time-step size can be very limiting in reservoir simulations, especially in regions with large values of the velocity.

Implicit schemes are free of this restriction and are the more common approach in reservoir simulations. However, this scheme solves a nonlinear system of equations using the

Newton or the Newton-Raphson iterative methods. Let us briefly introduce the Newton-Raphson method. Consider the following residual equation for cell Ω_i (see Eq. 4.18):

$$G(s_i^{n+1}) = s_i^{n+1} - s_i^n - \frac{\Delta t}{\phi_i |\Omega_i|}\left(\sum_{j \neq i} F_{ij}(s_w^{n+1}) + \max(q_i, 0) + f_w(s_i^{n+1}) \min(q_i, 0)\right) \quad \text{Eq. 4.23}$$

To solve Eq. 4.18 for the new saturation using this method, we start with an initial guess, which is an approximation to the unknown, and move towards the correct solution in each iteration. Denoting by $\tilde{s}_i$ an approximation of the new saturation in cell Ω_i and using a Taylor expansion, we have:

$$0 = G(\tilde{s}_i + d\tilde{s}) \approx G(\tilde{s}_i) + G'(\tilde{s}_i)(d\tilde{s}), \quad \text{Eq. 4.24}$$

which gives a new approximation, $\tilde{s}_i + d\tilde{s}$, with $G'(\tilde{s}_i)d\tilde{s} = -G(\tilde{s}_i)$. This brief introduction to the solution of the implicit discretization and considering that at each iteration a linear system of equations is to be solved shows that this scheme is more computationally demanding than explicit schemes. This method also introduces more numerical diffusion into the solution for large time steps.

4.1.3 **Numerical errors**

Any approximation method involves numerical errors. Numerical errors usually have different sources and components. In steady-state single-phase flows and for a specific discretization scheme, the main source of error is the spatial discretization related to the resolution of the computational grid. In multiphase flows, another component is the temporal discretization error. Other sources of errors are splitting errors due to the decoupling between the pressure and saturation equations. The splitting errors can become severe in some cases, especially if the time steps are too large. In this section, we demonstrate the numerical errors and convergence properties of the finite volume scheme in single and multiphase flow problems. To

quantify the errors, we choose layer 70 of the second model of SPE10 benchmark test (Christie and Blunt, 2001). This model contains $60 \times 220 \times 85$ cells, in which the top 35 layers (70 ft) represent Tarbert formation and the bottom 50 layers (100 ft) represent Upper Ness formation. Tarbert formation is a shallow marine environment while the Upper Ness is fluvial. This model, used originally as a benchmark for upscaling methods in the 10th SPE comparative solution project, is highly heterogeneous. In Figure 4.3, porosity and permeability models are shown. Both Tarbert and Upper Ness formations have large permeability variations of several orders of magnitudes.

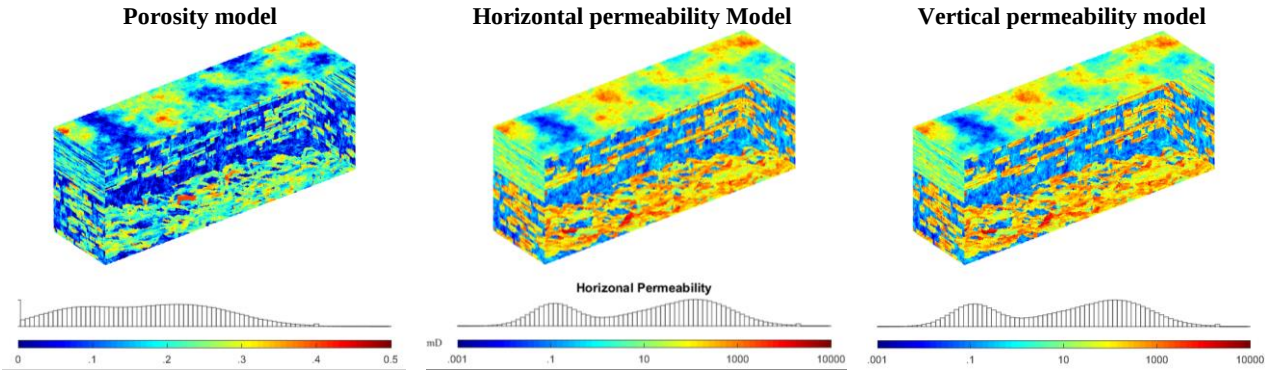

Figure 4.3: Porosity and permeability models for the SPE10 second model. The permeabilities are shown on the logarithmic scale (generated using the MRST[2]).

Errors are represented in terms of L^2 or L^1 norm of the difference between the discretized solution, denoted by $u_h(t)$ in a general form, and the continuous analytical solution, $u(t)$:

$$\|u_h - u\|^2_{L^2(\Omega)} = \left(\int_\Omega (u_h - u)^2 d\boldsymbol{x}\right)^{1/2} = \left(\sum_{\Omega_i \in \Omega} \int_{\Omega_i} \left(u_h(\boldsymbol{x}) - u(\boldsymbol{x})\right)^2 d\boldsymbol{x}\right)^{1/2} \quad \text{Eq. 4.25}$$

$$\|u_h - u\|_{L^1(\Omega)} = \left|\int_\Omega (u_h - u) d\boldsymbol{x}\right| = \left|\sum_{\Omega_i \in \Omega} \int_{\Omega_i} \left(u_h(\boldsymbol{x}) - u(\boldsymbol{x})\right) d\boldsymbol{x}\right|$$

[2] https://www.sintef.no/projectweb/mrst/

where u can be the pressure p or the saturation s. In most porous media flow problems, the exact analytical solution is not known. Therefore, we compute a highly refined numerical solution to set it as the reference and close representative of the analytical solution in Eq. 4.25. The order of convergence is estimated using the equation below:

$$\alpha = \frac{\ln\left(\frac{\left\|u_{h_{j-1}} - u\right\|^2_{L^2(\Omega)}}{\left\|u_{h_j} - u\right\|^2_{\mathrm{L}^2(\Omega)}}\right)}{\ln\left(\frac{h_{j-1}}{h_j}\right)} \qquad \text{Eq. 4.26}$$

where h_j and h_{j-1} denote the new and old step sizes. To quantify the spatial discretization errors for the flow equation, we choose the finite volume solution on the original fine resolution geological grid as the reference solution. We then compute the TPFA finite volume solution, p_{h_j} for a sequence of increasingly coarser computational grids with mesh sizes h_j. Each coarse grid is obtained by uniform agglomeration of the base fine grid with a coarsening ratio. In other words, if the domain is discretized with a Cartesian grid of 60×220 cells in the original form, a coarse grid with the coarsening ratio or the agglomeration ratio of 2 is a Cartesian grid of 30×110 cells. Boundary conditions include a no-flow condition imposed on the $YMAX$ and $YMIN$ exterior boundaries, and constant pressures at the $XMIN$ and $XMAX$ boundaries. The discretization error for different levels of coarse grid resolution is computed using Eq. 4.25. The results are represented in Table 4.1. The pressure solutions for different discretization levels are shown in Figure 4.4. As expected, the finer the resolution of the computational grid is, the smaller the discretization error is. But on the other hand, the main constraint in real-field three-dimensional reservoir simulations is the computational cost of solving flow problems in high-resolution grids.

Table 4.1: Spatial discretization numerical error and convergence order for the numerical approximation of flow equation using finite volume method in layer 70 of the SPE10 test case.

Grid resolution	**L2 norm** $\|u_h - u\|^2_{L^2(\Omega)}$	**L2 relative error** $\frac{\left(\|u_h - u\|^2_{L^2(\Omega)}\right)}{\|u\|^2_{L^2(\Omega)}}$	**Order of convergence**
3*11	7.79E+07	3.45E-02	--
6*22	4.53E+07	2.00E-02	0.781269
12*44	2.63E+07	1.16E-02	0.783122
24*44	1.53E+07	6.78E-03	0.780786

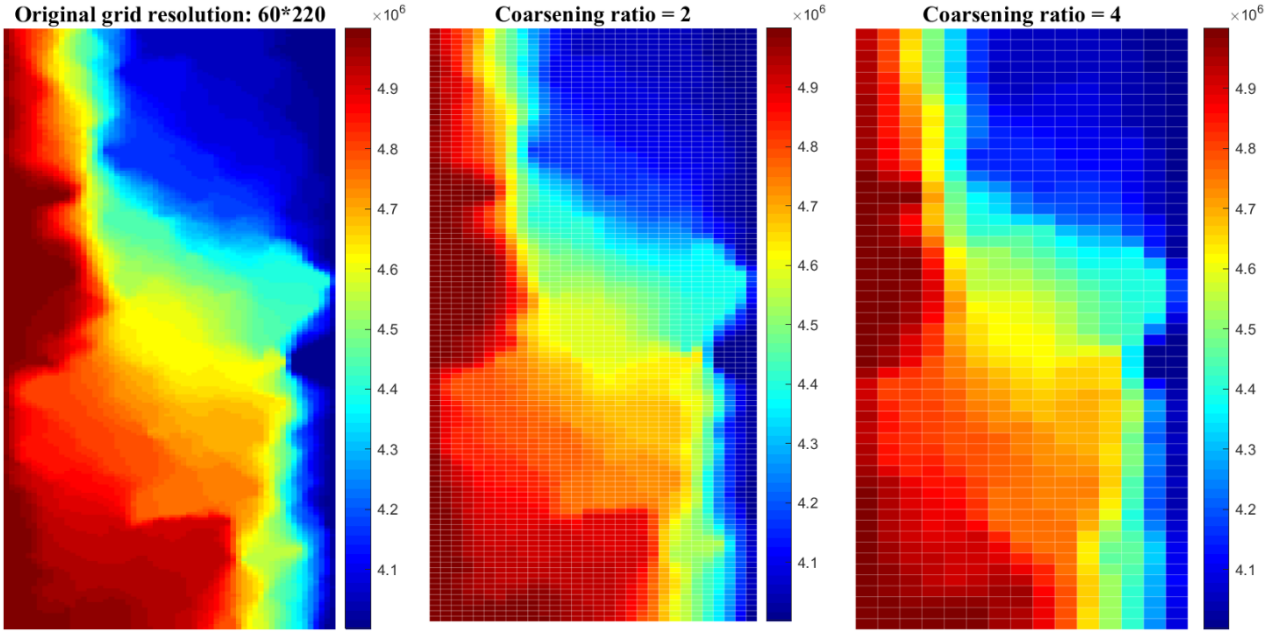

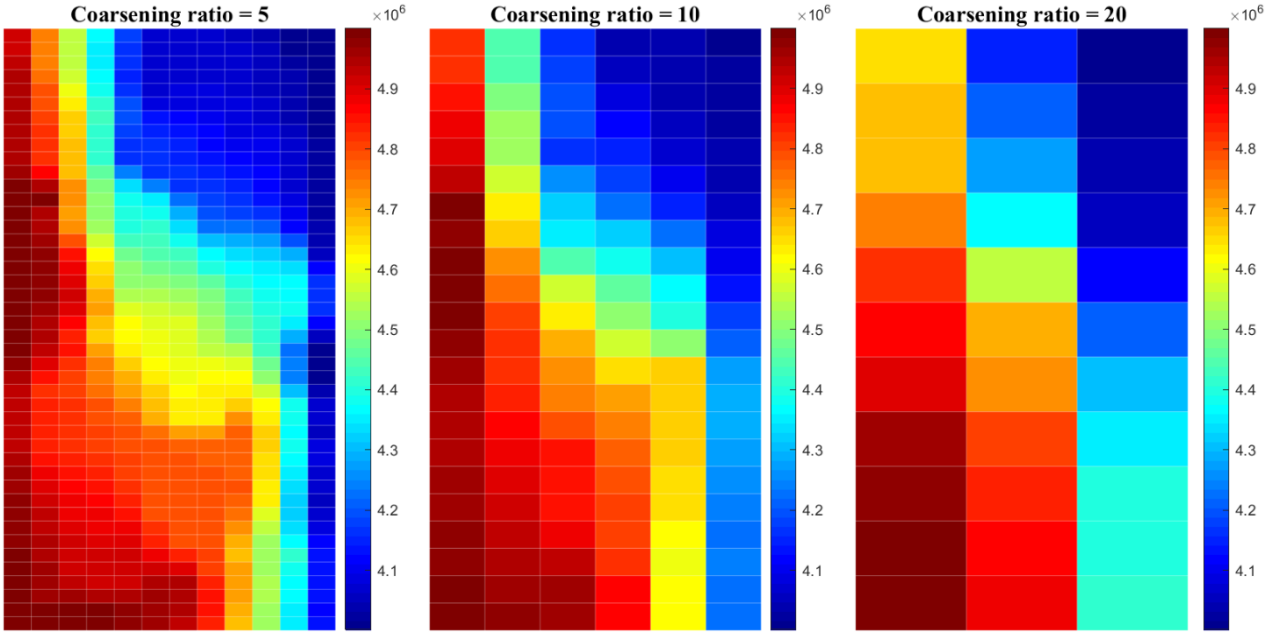

Figure 4.4: Pressure approximations using finite volume discretization of the single-phase flow equation for different levels of computational grid resolution in layer 70 of the SPE10 benchmark test.

To demonstrate the temporal discretization error of the implicit finite volume solution of the transport equation in the same layer of the SPE10 test case, we consider a waterflood problem. The flow and pressure boundary conditions are kept the same as in the previous example. The reservoir is initially fully saturated with oil with a viscosity of $0.5\ cp$. The water of viscosity $0.05\ cp$ is injected from the left ($XMIN$) boundary of the domain. The temporal discretization error is computed after 1000 days discretized with one timestep i.e., $\Delta t = 1000$ days. First, the pressure is approximated using a TPFA finite volume scheme and the fluxes are used to approximate the saturation in different cases. The transport equation is numerically solved with an implicit formulation with different cases of saturation substeps $\delta t = \Delta t/2^n$, with $n = 0, \dots, 6$. The reference solution is set to be the transport solution with $2^7 = 128$ saturation substeps.

Table 4.2 shows the L1 errors and convergence rates. Some of the saturation profiles along with the reference solution are presented in Figure 4.5. The decrease in numerical diffusion with decreasing the size of the saturation time step can be seen qualitatively from this figure.

Table 4.2: Temporal discretization numerical error and convergence order for the FV approximation of the transport equation using the implicit scheme in layer 70 of SPE10 model.

Saturation steps	L1 norm	L1 relative error	Order of convergence
1	3.63E+03	4.90E-01	--
2	2.23E+03	3.01E-01	0.70
4	1.29E+03	1.75E-01	0.79
8	7.08E+02	9.55E-02	0.87
16	3.61E+02	4.86E-02	0.97
32	1.64E+02	2.21E-02	1.14
64	5.67E+01	7.64E-03	1.53

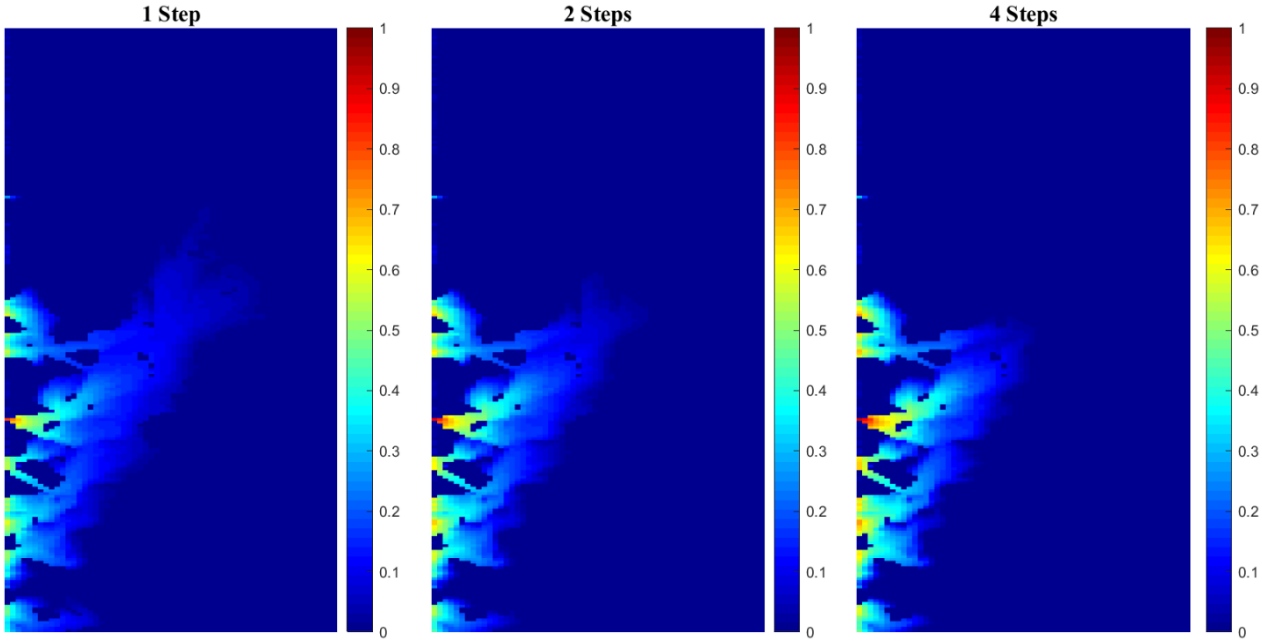

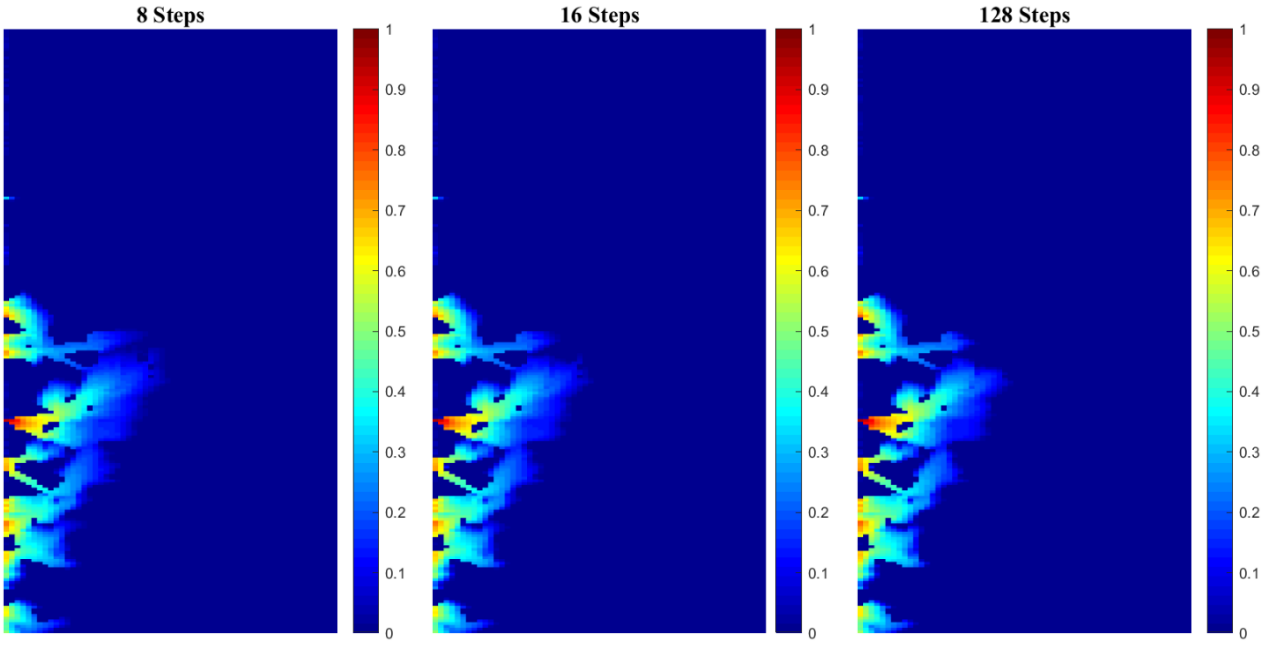

Figure 4.5: Saturation approximation using the implicit scheme for different numbers of saturation time steps in layer 70 of the SPE10 benchmark test.

The last type of numerical errors we study is the splitting error. As mentioned before, the pressure and saturation equations are coupled through the mobility terms in the pressure equation and velocity terms in the saturation equation. To demonstrate the splitting error related to the decoupling of flow and transport solvers, we consider the same model as in the previous example, with same oil viscosity of $0.5\,cp$ and two cases of water viscosity, 0.05 and $0.5\,cp$. The motivation behind this is to show the impact of viscosity ratio $M = \mu_o/\mu_w$ on the splitting error. The total time of simulation, T, is 4000 days, which is discretized with different timestep sizes, Δt, in different cases: $\Delta t = T/2^n$, with $n = 0, \dots, 6$. The saturation is solved using the explicit finite volume scheme in all cases.

Table 4.3 and Table 4.4 present the L^2 and L^1 errors related to the pressure and saturation approximations for the two cases of M. Figure 4.6 shows the saturation profiles in comparison with the reference solution, which is the IMPES solution with the time step of size $\Delta t = T/2^7$. These saturation profiles qualitatively show the impact of mobility variations on the coupling between pressure and saturation equations. When the viscosity ratio, M, deviates from one, the coupling between pressure and saturation is stronger and large time steps can lead to large errors.

Table 4.3: Splitting error and convergence order for the FV IMPES scheme in a waterflood problem with the viscosity ratio $M = \mu_o/\mu_w = 10$ in layer 70 of the SPE10 test case.

Splitting steps	**Saturation**		**Pressure**	
	L1 norm relative	Order of convergence	L2 norm relative	Order of convergence
1	3.28E-01	--	1.61E-02	--
2	2.00E-01	0.71	3.26E-03	2.31
8	3.68E-02	1.21	1.17E-03	1.88
16	1.62E-02	1.18	3.68E-04	1.66
32	7.24E-03	1.16	1.28E-04	1.52
64	2.37E-03	1.61	3.86E-05	1.74

Table 4.4: Splitting error and convergence order for the FV IMPES scheme in a waterflood problem with the viscosity ratio $M = \mu_o/\mu_w = 1$ in layer 70 of the SPE10 test case.

Splitting steps	**Saturation**		**Pressure**	
	L-2 norm relative	Order of convergence	L-2 norm relative	Order of convergence
1	1.32E-01	--	7.92E-03	--
2	6.74E-02	0.97	2.98E-03	1.41
4	3.43E-02	0.98	1.61E-03	0.89
8	1.68E-02	1.03	1.20E-03	0.42
16	7.52E-03	1.16	6.88E-04	0.80
32	3.17E-03	1.24	2.90E-04	1.25
64	1.03E-03	1.63	8.96E-05	1.69

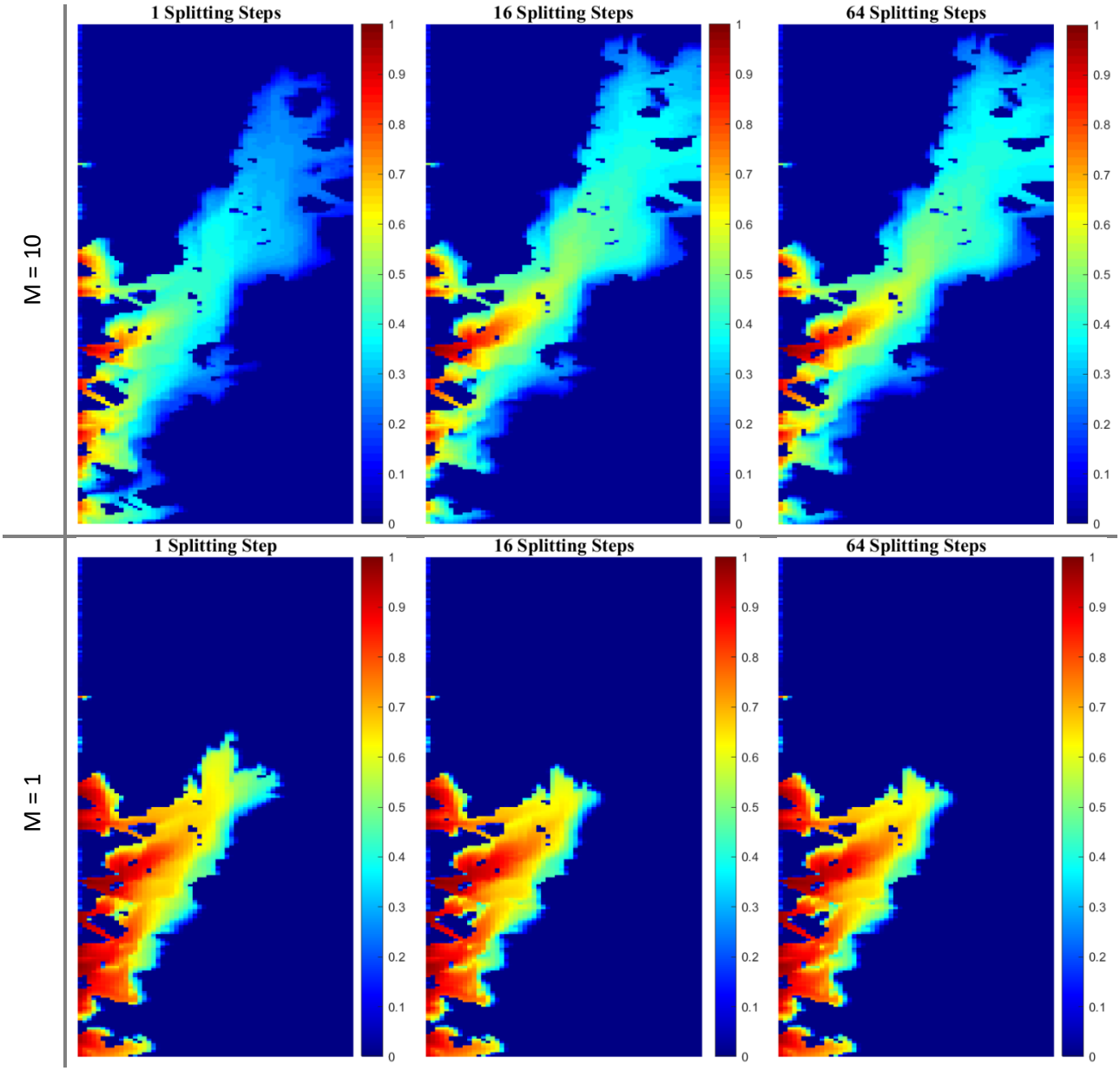

Figure 4.6: Saturation profiles using the FV IMPES scheme with splitting steps of 1, 16, and 64 and two cases of viscosity ratio in layer 70 of the SPE10 benchmark test.

4.2 Discontinuous Galerkin method

4.2.1 Discretizing the flow equation

In this section, we detail the discontinuous Galerkin (DG) discretization method for solving the multiphase flow equation. To obtain the DG discretization of the pressure equation

Eq. 2.16, we first re-write the elliptic pressure equation in a mixed form through the introduction of an auxiliary variable $\boldsymbol{z} \coloneqq \nabla p$ (Cockburn and Shu, 1998)

$$\begin{cases} \boldsymbol{z} = -\nabla p, & in\ \Omega, \\ \nabla.(k\lambda_T \boldsymbol{z}) = q, & in\ \Omega, \\ p = p_D, & on\ \partial\Omega_D, \\ \boldsymbol{z}.\boldsymbol{n} = 0, & on\ \partial\Omega_N. \end{cases} \quad \text{Eq. 4.27}$$

By multiplying the first and second equations by smooth test functions $\boldsymbol{y}$ and ω, respectively, and integrating by part on a cell Ω_i we get,

$$\int_{\Omega_i} \boldsymbol{y}.\boldsymbol{z} - \int_{\Omega_i} \nabla.\boldsymbol{y}p + \int_{\partial\Omega_i} \boldsymbol{y}.\boldsymbol{n}p = 0, \quad \text{Eq. 4.28}$$

$$-\int_{\Omega_i} \nabla\omega.(k\lambda_T \boldsymbol{z}) + \int_{\partial\Omega_i} \omega k\lambda_T \boldsymbol{z}.n = \int_{\Omega_i} \omega q. \quad \text{Eq. 4.29}$$

Let us denote by $\mathbb{P}_P(\Omega_i)$ the space of polynomials of degree at most P on $\Omega_i \in \Omega$ and by $P_P(\Omega) = \{\omega_i : \bar{\Omega} \to R;\ \forall\Omega_i \in \Omega, \omega_i|\Omega_i \in P_P(\Omega_i)\}$ the space of discontinuous polynomials on the partitioned domain Ω. The general form of the local discontinuous Galerkin method is obtained as follows to find $p_i \in P_P(\Omega)$ and $\boldsymbol{z}_i \in [P_P(\Omega)]^2$ (Arnold et al., 2002)

$$\int_{\Omega_i} \boldsymbol{y}.\boldsymbol{z}_i - \int_{\Omega_i} \nabla.\boldsymbol{y}p_i + \int_{\partial\Omega_i} \boldsymbol{y}.\boldsymbol{n}_i\hat{p}_i = 0 \quad \text{Eq. 4.30}$$

$$-\int_{\Omega_i} \nabla\omega.(k\lambda_T \boldsymbol{z}_i) + \int_{\partial\Omega_i} \omega k\lambda_T \hat{\boldsymbol{z}}_i.\boldsymbol{n}_i = \int_{\Omega_i} \omega q. \quad \text{Eq. 4.31}$$

Here, $\hat{p}_i$ and $\hat{\boldsymbol{z}}_i$ are approximations to p and $\boldsymbol{z} = -\nabla p$, respectively, on the boundary of Ω_i, that need to be defined. We choose the form introduced by Cockburn and Shu (1998). Let us assume we are at the current time step n and p^n, $\boldsymbol{z}^n$, and s^n are known. The DG discretization method to solve Eq. 4.27 solves the following system to obtain $p_i^{n+1} \in P_P(\Omega)$ and $\boldsymbol{z}_i^{n+1} \in [P_P(\Omega)]^2$, for $\forall\Omega_i \in \Omega$, $\forall\boldsymbol{y}_i \in [P_P(\Omega)]^2$, and $\forall\omega_i \in P_P(\Omega)$, (Frank et al., 2015):

$$\int_{\Omega_i} \boldsymbol{y}_i.\boldsymbol{z}_i^{n+1} - \int_{\Omega_i} \nabla.\boldsymbol{y}_i p_i^{n+1} + \sum_j \int_{\sigma_{ij}} \boldsymbol{y}_i.\boldsymbol{n}_{ij} \begin{cases} \{p_i^{n+1}\}, & on\ \varepsilon_\Omega \\ p_D, & on\ \varepsilon_D \\ p_i^{n+1}, & on\ \varepsilon_N \end{cases} = 0, \quad \text{Eq. 4.32}$$

$$
\begin{aligned}
&-\int_{\Omega_i} \nabla\omega_i.\left(k_i\lambda_{T_i}^n \boldsymbol{z}_i^{n+1}\right) \\
&+\sum_j \int_{\sigma_{ij}} \omega_i \begin{cases} \left\{\left(k_i\lambda_{T_i}^n\right)\boldsymbol{z}_i^{n+1}\right\}.\boldsymbol{n}_{ij} + \dfrac{\eta}{h_{ij}}[\![p_i^{n+1}]\!].\boldsymbol{n}_{ij}, & on\ \varepsilon_\Omega \\ \left(k_i\lambda_{T_i}^n\right)\boldsymbol{z}_i^{n+1}.\boldsymbol{n}_{ij} + \dfrac{\eta}{h_{ij}}\left(p_i^{n+1} - p_D\right), & on\ \varepsilon_D \\ 0, & on\ \varepsilon_N \end{cases} \\
&= \int_{\Omega_i} \omega_i q_i^{n+1}
\end{aligned}
\qquad \text{Eq. 4.33}
$$

η is a user-defined penalty coefficient h_{ij} is the diameter of the face σ_{ij}. $\varepsilon = \{\partial\Omega_i\}$ is the set of all faces composed of interior faces ε_Ω and boundary faces $\varepsilon_{\partial\Omega}$. Boundary faces include the Dirichlet set ε_D and Neumann set ε_N. For any interior face σ_{ij} and any function $\omega = \omega(x)$, the jump of ω is defined as,

$$[\![\omega]\!]_{ij} := \omega_i \boldsymbol{n}_{ij} + \omega_j \boldsymbol{n}_{ji} = \left(\omega_i - \omega_j\right)\boldsymbol{n}_{ij} \qquad \text{Eq. 4.34}$$

and the weighted average of ω as:

$$\{\omega\}_{ij} = \omega_i w_{ij} + \omega_j(1 - w_{ij}). \qquad \text{Eq. 4.35}$$

Taking $w_{ij} = 0.5$ leads to the simple arithmetic averaging.

For the DG numerical resolution of Eq. 4.32 and Eq. 4.33, we use FESTUNG[3], the Finite Element Simulation Toolbox for Unstructured Grids, an open-source MATLAB/GNU Octave toolbox, developed as a package for discontinuous Galerkin methods. For more details of this DG method and its implementation, we refer to the series of papers that the authors of this toolbox have published: Frank et al. (2015), Reuter et al. (2016), Jaust et al. (2018), Reuter et al. (2018), and Reuter et al. (2020).

4.2.2 **Adaptation of FESTUNG for reservoir simulations**

To adapt the FESTUNG toolbox for flow simulations in porous media and better take the permeability heterogeneities into account, we have implemented some changes. Following Di Pietro and Ern (2011), we have changed the standard arithmetic average in the averaging operator

[3] https://github.com/festung/FESTUNG

of Eq. 4.35 into a harmonic average depending on the values of $(k\lambda_T)$ calculated based on the saturation at the previous time step in a sequential multiphase flow model:

$$w_{ij}^n = \frac{\alpha_j^n}{\alpha_i^n + \alpha_j^n} \qquad \text{Eq. 4.36}$$

where $\alpha^n = k\lambda_T^n$. Another necessary improvement to generalize the DG discretization to porous medium related flow problems is in the penalization of internal and boundary jumps. The introduction of the harmonic average of diffusion coefficient $(k\lambda_T)$ to penalize jumps across faces in heterogeneous anisotropic media was proposed in the work of Ern et al. (2008). Therefore, $\frac{\eta}{h_{ij}}$ in Eq. 4.33 is replaced with $\frac{\eta\gamma_{ij}^n}{h_{ij}}$ (Jamei and Ghafouri, 2016). γ_{ij}^n is a penalty factor, that unlike the user-defined η, considers the permeability and mobility on both sides of the interface σ_{ij}. γ_{ij}^n on the interfaces is set to be the harmonic average of α^n values in the two neighbouring cells for the interior faces $\sigma_{ij} \in \varepsilon_\Omega$:

$$\gamma_{ij}^n = \frac{2 \times \alpha_i^n \alpha_j^n}{\alpha_i^n + \alpha_j^n} \qquad \text{Eq. 4.37}$$

This value reduces to α_i^n in Dirichlet boundaries. The use of the harmonic average of diffusivity coefficient $(k\lambda)$ to penalize jumps and diffusivity dependant weights in averaging operators has been proved to be necessary for heterogeneous porous media, similar to the importance of harmonic averaged terms in the calculation of face transmissibility in finite volume methods (Di Pietro and Ern, 2011).

When the diffusion coefficient heterogeneity has several orders of magnitude, it is critical to adapt the DG scheme. Figure 4.7 and Figure 4.8 show the pressure and velocity approximations computed using the DG method, with FESTUNG default and adapted schemes, in layer 70 of SPE10 benchmark model. We set Dirichlet conditions on the west and east boundaries, and a no-flow condition on the north and south boundaries. The computations are done on the original fine grid. The order of approximation in the DG scheme is set to one in all grid cells. From this figure, it can be observed that the impact of the adapted penalty strategy and diffusion dependent weights in heterogeneous domains becomes more important especially in

flux approximations. By comparing the flux magnitudes in default and adapted implementations and considering the permeability field shown in Figure 4.9, it can be observed that the difference is larger in high-permeability zones. This high permeability subdomains, shown in red in Figure 4.9, have important impacts on the solution of the transport equation.

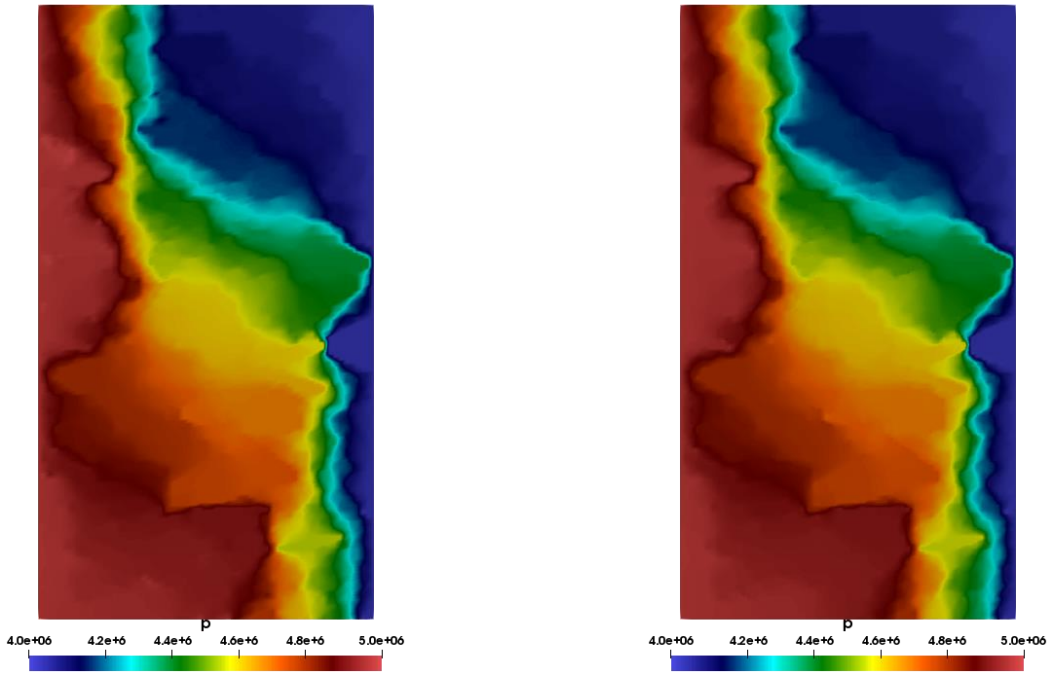

Figure 4.7: Pressure approximations using the DG scheme with the default formulation in the left plot and the adapted formulation in the right plot.

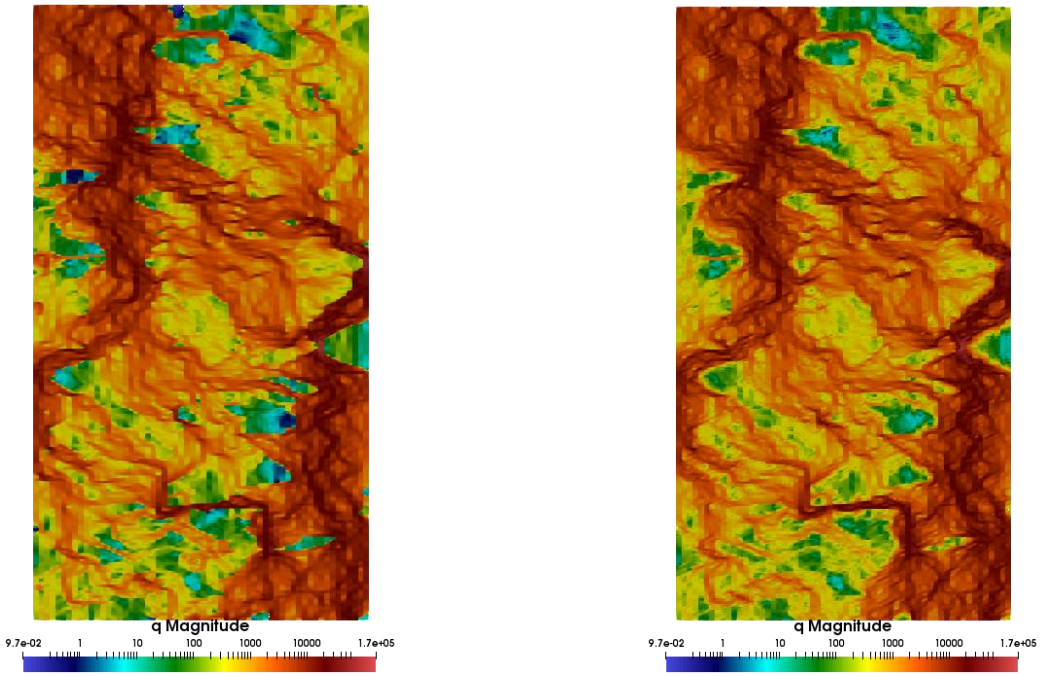

Figure 4.8: Magnitude of DG approximations of (∇p) using the default formulation in the left plot and the adapted formulation in the right plot, on a logarithmic scale.

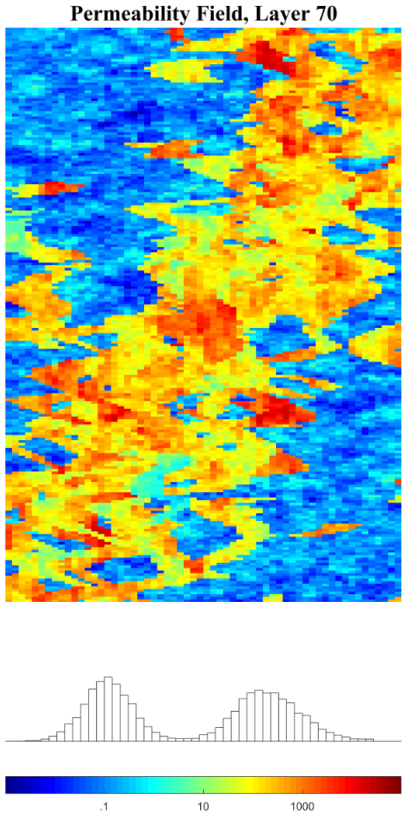

Figure 4.9: Permeability field in layer 70 of SPE10 second model, shown on a logarithmic scale to better represent the variations.

4.2.3 **Reconstruction of conservative fluxes**

To reconstruct conservative fluxes from the DG solution we compute:

$$v_{ij}^{n+1} = \begin{cases} \int_{\sigma_{ij}} \{(k_i \lambda_{T_i}^n) \boldsymbol{z}_i^{n+1}\}.\boldsymbol{n}_{ij} + \dfrac{\eta \gamma_{ij}^n}{h_{ij}} [\![p_i^{n+1}]\!].\boldsymbol{n}_{ij}\,, & on\ \varepsilon_\Omega, \\ \int_{\sigma_{ij}} (k_i \lambda_{T_i}^n) \boldsymbol{z}_i^{n+1}.\boldsymbol{n}_{ij} + \dfrac{\eta \gamma_{ij}^n}{h_{ij}} (p_i^{n+1} - p_D)\,, & on\ \varepsilon_D, \end{cases} \quad \text{Eq. 4.38}$$

which corresponds to Eq. 4.33 with the test function $\omega = 1$. This equation also shows the local conservation property of DG scheme.

4.2.4 **Using the underlying permeability values**

Another objective of using DG in this work is to test the idea of using the underlying fine permeability values instead of one upscaled permeability value per grid block when evaluating the integral terms.

In DG, the face and cell integrals are evaluated using quadrature integration rules. The quadrature rule for the reference element $\widehat{\Omega}$ is defined by:

$$\int_{\widehat{\Omega}} \hat{g}(\hat{x}) d\hat{x} = \sum_{r=1}^{R} \omega_r \hat{g}(\widehat{\boldsymbol{q}}_r) \quad \text{Eq. 4.39}$$

with R quadrature points $\widehat{\boldsymbol{q}}_r \in \widehat{\Omega}$ and quadrature weights $\omega_r \in \mathbb{R}$. The quadrature rule and all the integrals are defined in the reference element and a one-to-one mapping F_i relates the reference element to every physical cell. The idea is to use a lower resolution grid along with the underlying fine permeability values at the quadrature points instead of one upscaled value for all the quadrature points in one cell or face. One of the points to notice is the decision to use the finest permeability value at the closest point to the quadrature point or to use an intermediate resolution value depending on the total number of quadrature points per element.

As already mentioned in the DG formulation, we assume that all the coefficient functions are in piecewise polynomial spaces. Considering the diffusivity coefficient in the multiphase flow equation $\alpha(t) = k\lambda_T$, in FESTUNG, we seek for a matrix $\mathrm{A}(t) \in \mathbb{R}^{K\times N}$ such that:

$$\alpha_i(t, \boldsymbol{x})|_{\Omega_i} = \sum_{l=1}^{N} \mathrm{A}_{il}(t)\varphi_{il}(\boldsymbol{x}) \qquad \text{Eq. 4.40}$$

where $\alpha_i(t)$ approximates $\alpha(t) = k\lambda_T$. In FESTUNG, L^2-projection is used to produce this approximation, being locally defined for each element Ω_i:

$$\forall \omega_i \in \mathbb{p}_d(\Omega), \int_{\Omega_i} \omega_i \alpha_i(t) = \int_{\Omega_i} \omega_i \alpha(t) \qquad \text{Eq. 4.41}$$

Choosing $\omega_l = \varphi_{il}$ for $j \in \{1, \dots, N\}$ and using the numerical quadrature, we get (see Frank et al. (2015) for more details):

$$\begin{aligned}
&\int_{\widehat{\Omega}} \begin{bmatrix} \hat{\varphi}_1(\hat{\boldsymbol{x}})\alpha\big(t, \boldsymbol{F}_i(\hat{\boldsymbol{x}})\big) \\ \vdots \\ \hat{\varphi}_N(\hat{\boldsymbol{x}})\alpha\big(t, \boldsymbol{F}_i(\hat{\boldsymbol{x}})\big) \end{bmatrix} d\hat{\boldsymbol{x}} \\
&= \sum_{r=1}^{R} \omega_r \begin{bmatrix} \alpha\big(t, \boldsymbol{F}_1(\hat{\boldsymbol{q}}_r)\big) \\ \vdots \\ \alpha\big(t, \boldsymbol{F}_K(\hat{\boldsymbol{q}}_r)\big) \end{bmatrix} [\hat{\varphi}_1(\hat{\boldsymbol{q}}_r), \quad \cdots, \quad \hat{\varphi}_N(\hat{\boldsymbol{q}}_r)] \qquad \text{Eq. 4.42} \\
&= \begin{bmatrix} \alpha\big(t, \boldsymbol{F}_1(\hat{\boldsymbol{q}}_1)\big) & \cdots & \alpha\big(t, \boldsymbol{F}_1(\hat{\boldsymbol{q}}_R)\big) \\ \vdots & \ddots & \vdots \\ \alpha\big(t, \boldsymbol{F}_K(\hat{\boldsymbol{q}}_1)\big) & \cdots & \alpha\big(t, \boldsymbol{F}_K(\hat{\boldsymbol{q}}_R)\big) \end{bmatrix} \begin{bmatrix} \omega_1\hat{\varphi}_1(\hat{\boldsymbol{q}}_1) & \cdots & \omega_1\hat{\varphi}_N(\hat{\boldsymbol{q}}_1) \\ \vdots & \ddots & \vdots \\ \omega_R\hat{\varphi}_1(\hat{\boldsymbol{q}}_R) & \cdots & \omega_R\hat{\varphi}_N(\hat{\boldsymbol{q}}_R) \end{bmatrix}
\end{aligned}$$

Here, the idea is to use the finer resolution values at the positions of $\alpha\big(t, F_i(\hat{\boldsymbol{q}}_r)\big)$ in the matrix $\begin{bmatrix} \alpha\big(t, \boldsymbol{F}_1(\hat{\boldsymbol{q}}_1)\big) & \cdots & \alpha\big(t, \boldsymbol{F}_1(\hat{\boldsymbol{q}}_R)\big) \\ \vdots & \ddots & \vdots \\ \alpha\big(t, \boldsymbol{F}_K(\hat{\boldsymbol{q}}_1)\big) & \cdots & \alpha\big(t, \boldsymbol{F}_K(\hat{\boldsymbol{q}}_R)\big) \end{bmatrix}$ instead of the coarse-scale values. There is a limit in the number of quadrature points per element for a specific order of polynomials. We have tried to test this idea and Figure 4.10 shows an example of the preliminary results. As can be seen, the details in the right plot with the underlying permeability have increased in some parts of the domain. However, we did not proceed this approach further and it is planned to be continued in the future work (see the perspectives in chapter 7).

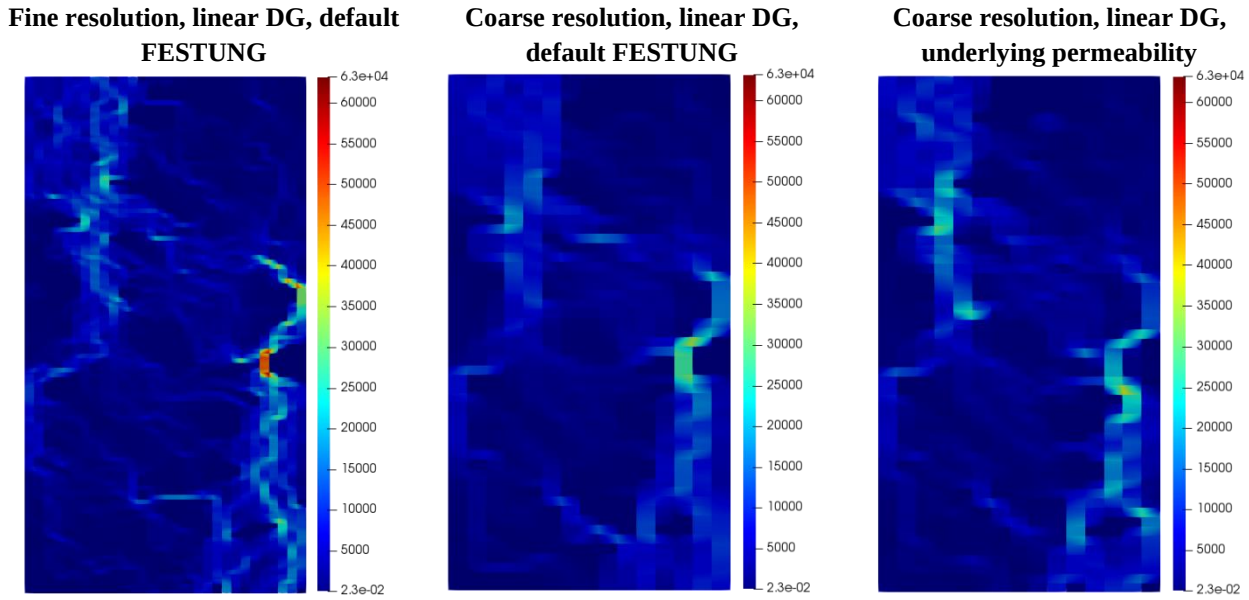

Figure 4.10: Magnitude of flux computed using the DG discretization scheme with linear approximations, on fine and coarse grids for the default implementation, and the coarse grid with underlying fine permeability values.

4.2.5 **Numerical errors**

In this section, we demonstrate the error estimations for DG discretization scheme of the flow equation. Throughout this work, we implement the DG scheme only for the pressure equation in the immiscible incompressible flow problems. We choose layer 70 of SPE 10 benchmark test, like previous examples. This layer, from Upper Ness formation, has heterogeneity over several orders of magnitude and has high-permeable sandstone channelled into low-permeable flow barriers. Due to limitations in available computational resources, we have chosen a subdomain that covers 60×60 cells of the whole computational grid with 60×220 cells. The errors are demonstrated in terms of the L2-norm for approximated solutions computed at different resolutions: the P-resolution and the h-resolution, associated with the order of polynomials and the mesh resolution, respectively.

4.2.5.1 **p-convergence**

To evaluate the P-convergence of the DG scheme, we fix the spatial resolution at the original resolution and change the order of approximations from 0 to 3. The reference solution is

set as the DG approximated solution on this Cartesian grid with an order of approximation 4. Table 4.5 represents the L2-norms relative to the reference solution.

Table 4.5: L2 norm for p and $\boldsymbol{z} = \nabla p$ on the original grid with different orders of approximation.

Polynomial Degree	Pressure L2 norm	z_x L2 norm	z_y L-2 norm
0	4.17E+06	6.05E+05	4.26E+05
1	4.00E+05	1.98E+05	1.68E+05
2	1.38E+05	1.11E+05	1.07E+05
3	6.42E+04	8.09E+04	8.56E+04

4.2.5.2 **h-convergence**

To evaluate the h-convergence of the DG scheme, we fix the order of approximation and change the mesh resolution. Computational grids of different resolutions are created through a uniform agglomeration of the original fine grid, with agglomeration ratios of 1 (original grid), 2, 4, 5, 10, and 20 (the coarsest resolution). The order of approximating polynomials is set to 4, in all cases. The reference solution is the DG approximation with the order of polynomials 4, on the highest resolution grid. Table 4.6 represents L2-norms for the pressure p and the numerical flux ∇p. It is worth noting the higher order of convergence in the DG pressure approximation, which is close to 1, compared to the FV pressure approximation, which is about 0.8.

Table 4.6: L2 norm for pressure and numerical flux approximations, for different cases of grid resolution.

Agglomeration ratio	Pressure L-2 norm	Pressure order of convergence	z_x L2 norm	z_y L-2 norm
2	7.87E+06	1.17E+00	8.59E+05	6.28E+05
4	1.78E+07	9.99E-01	1.12E+06	7.74E+05
5	2.22E+07	9.33E-01	1.16E+06	7.72E+05
10	4.24E+07	9.77E-01	1.36E+06	7.94E+05
20	8.35E+07	--	1.39E+06	7.89E+05

To compare the P and h convergence rates, relative L2 errors in the x-component of $\boldsymbol{z} = \nabla p$, from both of the previous convergence tests, are plotted in Figure 4.11. To have a unified comparison, these relative errors are plotted versus the number of global degrees of freedom. This figure confirms that the P-convergence is faster than the h-convergence.

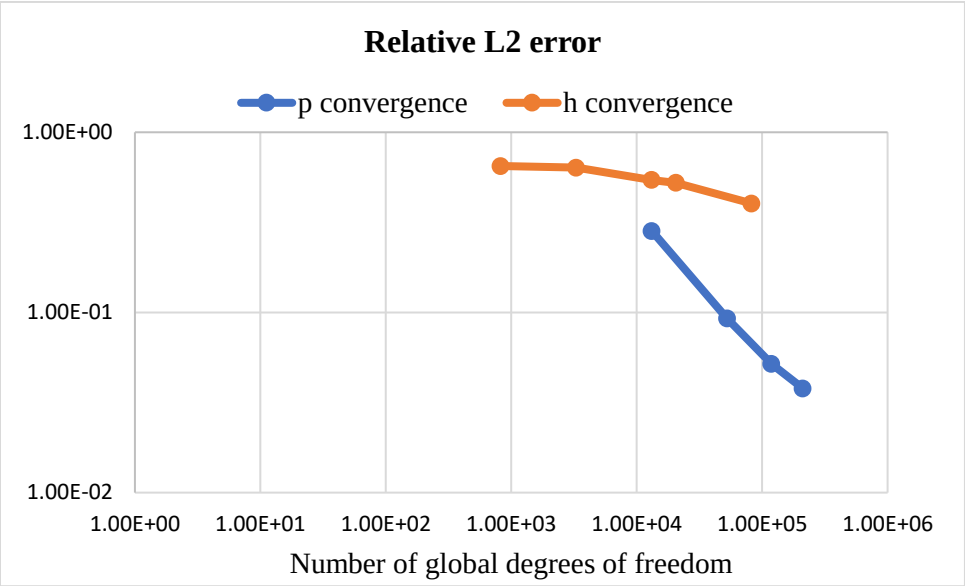

Figure 4.11: z_x relative L2 errors versus the number of global degrees of freedom, for both P and h convergence tests. Both axes are in logarithmic scale.

Figure 4.12 presents the magnitude of $\boldsymbol{z} = \nabla p$ for the reference solution and some variations of the mesh resolution and the order of polynomials. The total number of unknowns in the case with $P = 1$ in the original fine grid is the same as in the case with $P = 3$ in the coarsened grid with an agglomeration ratio of 2. The comparison of their corresponding plots shows that the finer resolution approximation is closer to the reference solution. It is also worth noticing that the DG method with the higher order of approximation on a lower resolution grid successfully captures the flow details in areas with large variations.

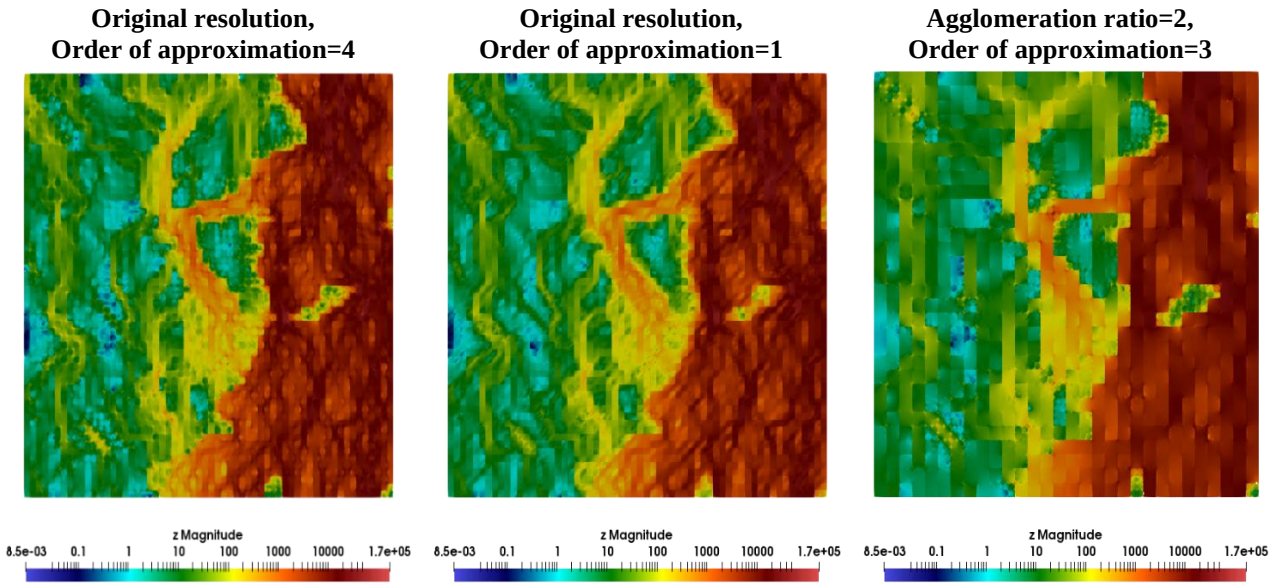

Figure 4.12: Magnitude of $\boldsymbol{z}$ in a subgrid of layer 70 of the SPE10 test case.

5 Fast front tracking method

We have developed a fast front tracking technique (FFrT) to estimate the position of the saturation discontinuity without solving the transport equation in each cell of the domain. The idea of this method is that the velocity of the front is mainly controlled by the interplay between the heterogeneity of absolute permeability and the mobility jump at the front, and not by the rarefaction wave behind the front that is continuously spreading along time, damping the instability. This method is an extreme simplification of the initial problem that is expected to yield a fast estimation of the location of the water-oil interface, based on some concepts from pore network modelling and Buckley Leverett equation. This method is an initial value problem, meaning that it computes the position of the interface from the given initial position of the front or the saturation discontinuity.

In this chapter, we detail the formulation of the proposed technique. We start with a review of the Buckley Leverett problem, as we use it in the proposed fast front tracking technique. We then present the formulation and the solution algorithm of the FFrT method, followed by several test cases to validate this technique in comparison with the analytical and standard numerical methods.

5.1 Buckley Leverett problem

One of the simplest and most widely used methods for estimating the advance of a fluid displacement front, in a one-dimensional immiscible displacement process, is the Buckley-Leverett (BL) theory. Buckley and Leverett (1942) provided an analytical solution for the case of a linear, incompressible, immiscible, two-phase flow system when gravity and capillary pressure effects are negligible. Water is injected at one edge and oil is produced at the other one. This method uses fractional flow theory to estimate the rate at which the injected water moves in the porous medium:

$$-\boldsymbol{v}\frac{\partial f_w}{\partial \boldsymbol{x}} = \phi\frac{\partial s}{\partial t} \qquad \text{Eq. 5.1}$$

This equation is referred to as the Buckley Leverett equation. It belongs to a type called "*quasi-linear homogeneous equation of the first order with two independent variables*" (Marle, 1981). According to the method of characteristics applied to the Buckley-Leverett equation, the velocity of the slice of the fluids with a saturation s, $\boldsymbol{v}|_s$, is given by:

$$\boldsymbol{v}|_s = \frac{\boldsymbol{v}}{\phi}\frac{\partial f_w}{\partial s}\Big|_s \qquad \text{Eq. 5.2}$$

In other words, if at the point $\boldsymbol{x}_f$ and at time t_1 the saturation is equal to s_f, it is still equal to this value at the position $\boldsymbol{x}_f + \Delta t \frac{v}{\phi}\frac{\partial f_w}{\partial s}\Big|_{s=s_f}$ and at time $t_1 + \Delta t$.

This solution may lead to meaningless multivalued saturations at the same location because these saturations do not travel at the same velocities. Buckley and Leverett assumed the existence of a saturation discontinuity and changed the solution obtained from the method of characteristics to a profile with a saturation discontinuity, given by a Rankine-Hugoniot condition (Marle, 1981). The Welge tangent method allows us to determine the value of the saturation shock and thus the position of discontinuity (Welge, 1952):

$$\frac{\partial f_w}{\partial s}\Big|_{s=s_f} = \frac{f_w(s_f) - f_w(s_{w_i})}{s_f - s_{w_i}} \qquad \text{Eq. 5.3}$$

5.2 FFrT formulation

Considering a two-phase flow problem like a waterflood, we suppose that the saturation takes only two values corresponding to the saturation ahead the front (typically s_{w_i}) and behind the front (typically s_f) the saturation corresponding to the Buckley-Leverett shock front. The mobility ratio between both fluids corresponds to the mobility ratio at the front. Explicit expressions may be obtained analytically if the input relative permeabilities are quadratic, that reads:

$$\begin{cases} \lambda_T^+ = \dfrac{1}{\mu_o}, & s = s_{w_i} \\ \lambda_T^- = \dfrac{2}{\mu_o}\left(1 - \dfrac{1}{\sqrt{1+M}}\right), & s = s_f \end{cases} \qquad \text{Eq. 5.4}$$

Here, $M = \mu_o/\mu_w$, is the viscosity ratio of displaced to the displacing fluid. It can be observed that for M=3 the mobility ratio at the front is equal to 1 and the viscous instability is less severe than that indicated by the value of M corresponding to pure fluids in a Hele-Shaw cell (Saffman and Taylor, 1958).

We define ζ_F^n as the set of all faces σ_{ij} where the front crosses the segment $(\boldsymbol{x}_i, \boldsymbol{x}_j)$. $\boldsymbol{x}_i$ and $\boldsymbol{x}_j$ represent the cell centres of the cells i and j. $\boldsymbol{x}_j$ represents the downstream cell depending on the direction of the flow (see Figure 5.1).

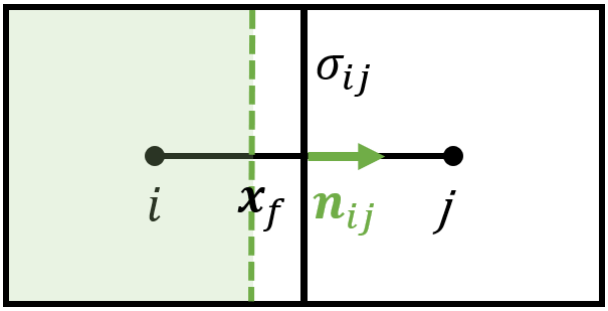

Figure 5.1: The two cells and the front position used to define the FFrT algorithm.

ζ_F^0 is initialized depending on the initial conditions of the transport problem. In the waterflood problem that we consider, the left Dirichlet boundary is considered as ζ_F^0. Now, consider that we are at time step n of the simulation, below is the flowchart of the method for each time step:

(1) Computation of the transmissibility values at all faces:

In the FFrT technique, the saturation can only take two values which represent the absence and presence of the front in the cell. Consequently, mobility takes the values of λ_T^+ or λ_T^- and $k_{r\alpha}$ takes the value of $k_{r_\alpha}^{max}$ depending on the position of the front. To compute the transmissibility values, we use a distance-weighted harmonic averaging of the cell mobilities, like Eq. 4.9 in the TPFA FV scheme:

$$T_{ij}^{n} = 2|\sigma_{ij}|d_{ij}\left(\frac{d_{i,\sigma}}{k_i\lambda_{T\,i}^{n}} + \frac{d_{j,\sigma}}{k_j\lambda_{T\,j}^{n}}\right)^{-1} \quad \text{Eq. 5.5}$$

The differences with the TPFA method include the calculation of total mobility values that only changes between two values, λ_T^+ and λ_T^-, and the computation of the transmissibility at the ζ_f faces (like in Figure 5.1). At these front faces, the transmissibility is computed as:

$$T_{ij}^{n} = 2|\sigma_{ij}|\, d_{ij}\left(\frac{d_{i,f}}{k_i\lambda_T^-} + \frac{d_{f,\sigma}}{k_i\lambda_T^+} + \frac{d_{j,\sigma}}{k_j\lambda_T^+}\right)^{-1} \quad \text{Eq. 5.6}$$

which is equivalent to the distance-weighted harmonic average of the three divisions with different properties, depending on the position of the front. It should be noted that thanks to the simplification of this technique, the transmissibility values need to be modified only at the position of the front. Initially $\lambda_T = \frac{k_{r_o}{}^{max}}{\mu_o}$. This value is updated each time at $\sigma_{ij} \in \zeta_f^n$.

(2) Solving the flow equation:

The pressures are calculated using the TPFA formulation of the finite volume method, by solving Eq. 4.8 for all $\Omega_i \in \Omega$, with the transmissibility values T_{ij}^n calculated using Eq. 5.5 and Eq. 5.6. It can be noted that the only difference between this method and a standard FV method in solving the flow equation is the calculation of transmissibility values.

(3) Computing the saturation at the front:

The Welge tangent method, Eq. 5.3, is used to construct the saturation at the front, s_f, analytically. For the case of quadratic relative permeabilities, this equation gives the saturation at the front as a function of the viscosity ratio, $M = \mu_o/\mu_w$, as follows:

$$s_f = 1/\sqrt{1+M} \quad \text{Eq. 5.7}$$

(4) Computing the velocity at the front:

We compute the velocity at the front, $v_{f,i,j}^{n+1}$, using the discretized form of Eq. 5.2 and the total fluxes v_{ij}^{n+1}:

$$v_{f,i,j}^{n+1} = \frac{v_{ij}^{n+1}}{|\sigma_{ij}|\phi} \frac{\partial f_w}{\partial s}\Big|_{s_f} \qquad \text{Eq. 5.8}$$

(5) Moving the front:

Considering that only the normal component of velocity accounts for the local velocity at the front, the discretized front is advanced according to the ordinary interface evolution equation:

$$\frac{\boldsymbol{x}_{f,i,j}^{n+1} - \boldsymbol{x}_{f,i,j}^{n}}{\delta t^{n+1}} = v_{f,i,j}^{n+1} \boldsymbol{n}_{ij} \qquad \text{Eq. 5.9}$$

δt^{n+1} denotes the sub-timestep for the update of the front position.

(6) Defining the sub-timestep:

We define the sub-timestep by posing a condition that measures the smallest time to reach the cell centre:

$$\delta t^{n+1} = \min_{\sigma_{ij} \in \zeta_F^n} \left(\frac{\left\| \boldsymbol{x}_j - \boldsymbol{x}_{f,i,j}^{n} \right\|}{v_{f,i,j}^{n+1}} \right). \qquad \text{Eq. 5.10}$$

$\boldsymbol{x}_{f,i,j}^{n}$ represents the current position of the front between two adjacent cells i and j (see Figure 5.1).

We repeat the steps (5) and (6) until the sum of all δt^{n+1} is equal to the time step in the main scheme, Δt^{n+1}.

5.3 Test case validation

To test the proposed FFrT method, we consider two-dimensional water-flood problems, where oil is displaced by water with identical or different viscosities. Both fluids are incompressible. Two regimes of flow can be distinguished, “stable” and “unstable”. Here, the

viscosity ratio, M, is used to differentiate these two types of flow. M is the ratio of the displaced fluid viscosity to the displacing fluid viscosity, μ_o/μ_w. In unstable flows, small perturbations grow with time and complex geometric structures called fingers are developed, first described by Saffman and Taylor (1958).

5.3.1 Buckley Leverett problem

We set up a simple example to compare the FFrT method with the BL solution and two finite volume implicit solvers on fine and coarse resolution grids.

We choose a $10 \times 2\, m^2$ domain, discretised by a fine-resolution Cartesian grid with 200×50 cells and a coarse-resolution one with 20×5 cells. The permeability and porosity are spatially homogeneous and equal to 0.01 Darcy and 1.0, respectively. The field is initially fully saturated with oil. Water is injected from the left edge with a constant rate of $10^{-6}\, m^3/s$ (4.3×10^{-3} pore volume/day). The oil viscosity is set to $10\ cp$. Three different cases are tested for water viscosity: 1, 3.33, and 10 cp, in different cases.

Figure 5.2 shows the comparison of the FFrT method with the analytical BL solution for a viscosity ratio of 3, at three different time steps corresponding to 0.13, 0.26, and 0.39 pore volume injected (PVI). Figure 5.3 compares the FFrT method with the analytical BL solution for viscosity ratios of 1 and 10 corresponding to water viscosities of 10 and 1, respectively. At last, the comparison of the analytical BL solution, the FFrT method, and two resolution of the finite volume method are shown in Figure 5.4. As it can be observed from all these figures, the FFrT method gives the exact location of the saturation discontinuity in the BL one dimensional displacement process. It should be noted that this method is developed to model only the position of the front. The saturation behind the front is homogeneously equal to the saturation at the front.

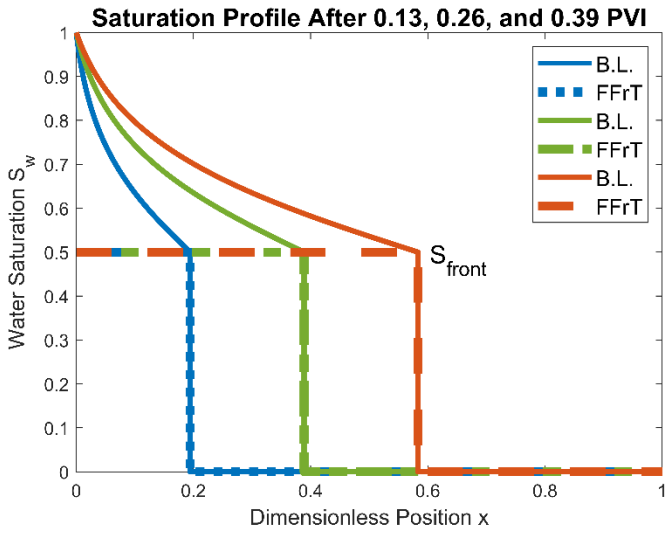

Figure 5.2: Comparison of the FFrT method with the analytical solution of the BL equation for a viscosity ratio of $M = 3$, at three different times.

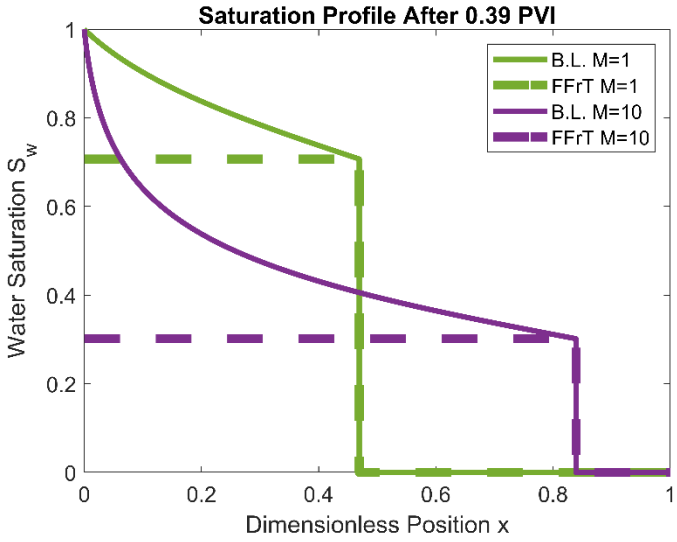

Figure 5.3: Comparison of the FFrT method with the analytical solution of the BL equation for two different viscosity ratio M=1 and 10, after 0.39 pore volume injected.

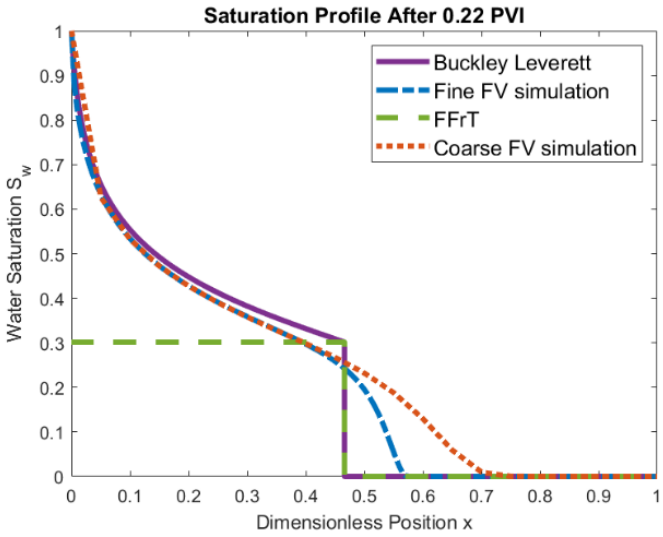

Figure 5.4: Saturation profiles obtained with the FFrT method, the analytical solution of the BL equation, and FV simulations on fine and coarse grids for a water-flood problem with the viscosity ratio $M = 10$, after 0.22 pore volume injected.

5.3.2 **Layered medium**

Let us consider a two-layers domain, with a different constant homogeneous permeability in each layer. We set Dirichlet boundary conditions on the left and right boundaries, and Neumann no-flow conditions on the top and bottom domain boundaries. The permeability ratio between the two layers and the viscosity ratio, M, are both set to 3. Figure 5.5 shows the comparisons between the FFrT method and the standard sequential implicit FV schemes on the coarse and fine grids. The coarse-resolution grid is used in the FFrT method. This method predicts the position of saturation discontinuity with very good precision.

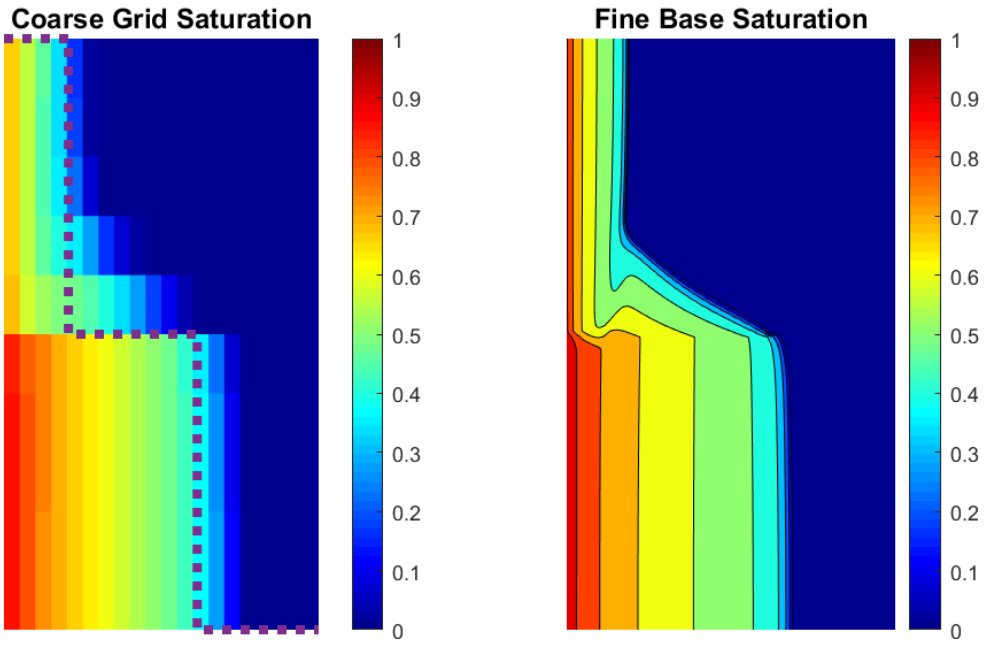

Figure 5.5: Layered medium test case. The left plot shows the saturation profile on a coarse mesh using the FV method. The dotted violet line shows the position of the saturation discontinuity using the FFrT method on the same mesh. The right plot presents the saturation contour map on the fine grid using the FV method, as a reference solution.

5.3.3 **Random generated isotropic medium**

To increase the complexity of test cases, we generate two heterogeneous random permeability models with two variance cases, as shown in Figure 5.6. Variances are presented as non-dimensional Dykstra-Parsons coefficients:

$$\sigma_{DP}^2 = 1 - e^{-\sigma} \qquad \text{Eq. 5.11}$$

where σ^2 is the variance and σ is the standard deviation. Gaussian covariance is used for both permeability models:

$$c(h) = \sigma^2 exp\left(-\left(\frac{h}{l_c}\right)^2\right) \qquad \text{Eq. 5.12}$$

where h is the spatial lag and l_c is the correlation length. l_c is the same in x and y directions and equal to 0.1 in both cases. The detailed properties for these two cases are shown in Table 5.1.

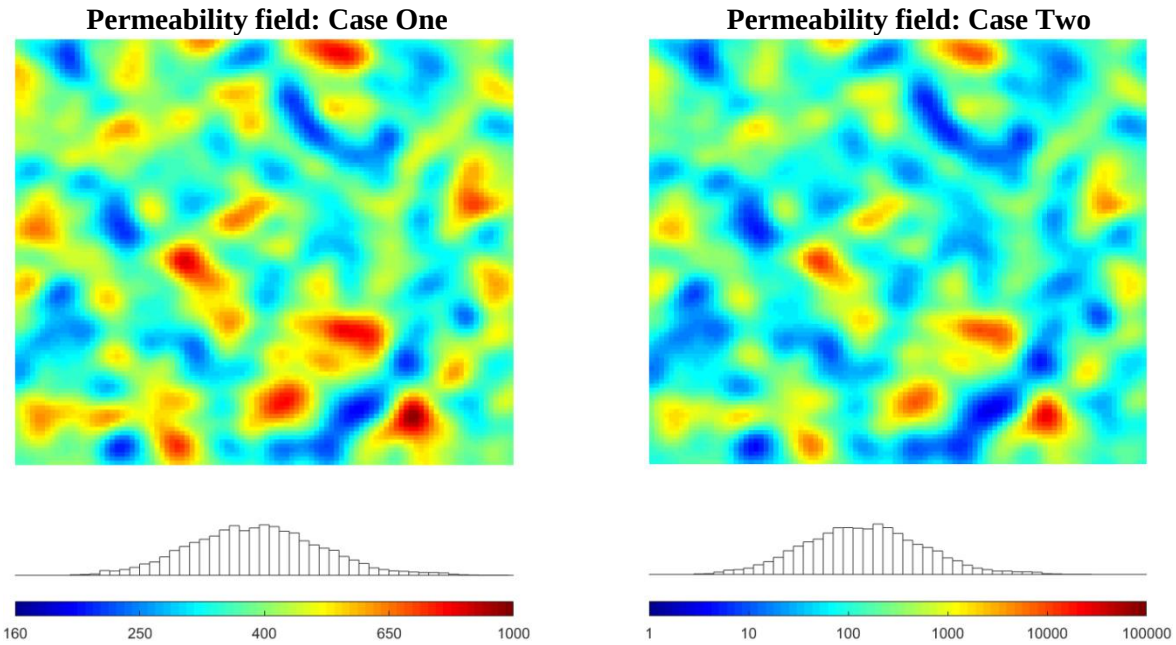

Figure 5.6: Isotropic randomly generated permeability models with a dimensionless correlation length of 0.1 and Dikstra-Parson coefficients of 0.2 (left) and 0.75 (right) on a logarithmic scale.

Table 5.1: Mean, standard deviation, and correlation length of the generated heterogeneous permeability models

	Permeability mean ($\boldsymbol{m^2}$)	Permeability standard deviation ($\boldsymbol{m^2}$)	Dimensionless correlation length (-)
Case One	4×10^{-13}	1×10^{-13}	0.1
Case Two	4×10^{-13}	1×10^{-12}	0.1

We consider the same two-phase flow problem of the previous example, with the same boundary conditions. We set oil viscosity to 10 cp and water viscosity to 10 and 1 cp, to test the method in both favourable and unfavourable displacement processes. The original grid contains 100×100 cells. In these examples, we test the FFrT method on the original resolution grid. In Figure 5.7, the water saturation maps for the permeability field of case one and a unit viscosity ratio are shown at two timesteps. The FFrT method prediction of the front position is in good accordance with the standard FV solution.

In Figure 5.8, water saturation maps and water saturation contour maps are shown for the same permeability field with a viscosity ratio of 10. In this more spreading front case, it seems

that the predicted position of the front is behind the modelled one with the FV method. To be able to analyse this difference in more detail, the water saturation contour maps computed with the FFrT and the FV methods for four viscosity ratios have been superimposed in Figure 5.9. For each case of the viscosity ratio M, the analytical saturation of the front, computed using Eq. 5.7, is also represented. In the case of a unit viscosity ratio with a relatively sharp front, the prediction of the FFrT method is in good accordance with the saturation profile computed using the standard FV scheme. When the viscosity ratio M increases and the front becomes more distorted, a small difference between the predicted front position and the FV solution can be observed. Due to the numerical errors inherent to both methods and the lack of an exact solution it may be difficult to interpret the difference.

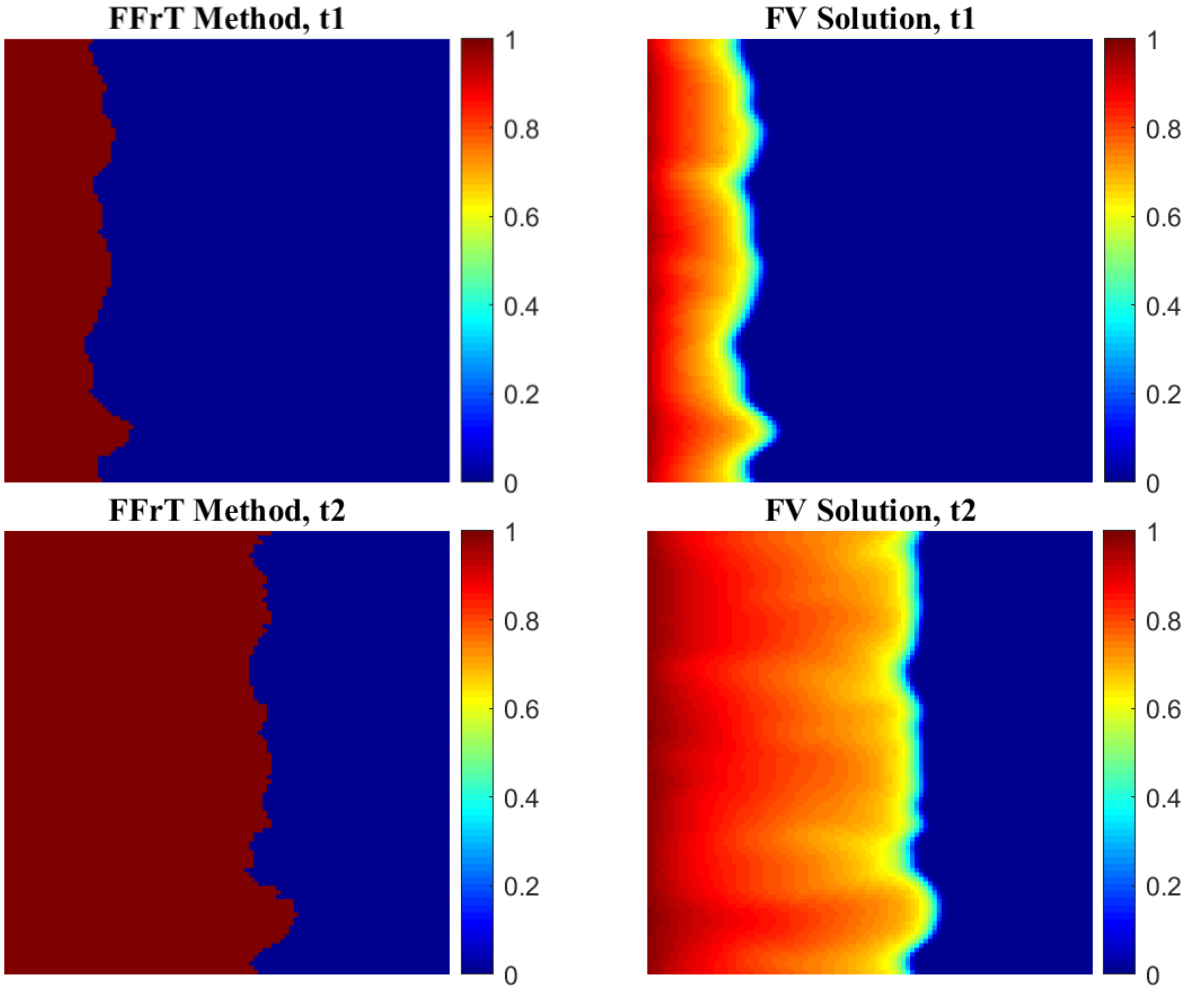

Figure 5.7: Water saturation maps for the first randomly generated permeability domain with a unit viscosity ratio at two different time steps, computed by the FFrT method and the FV method.

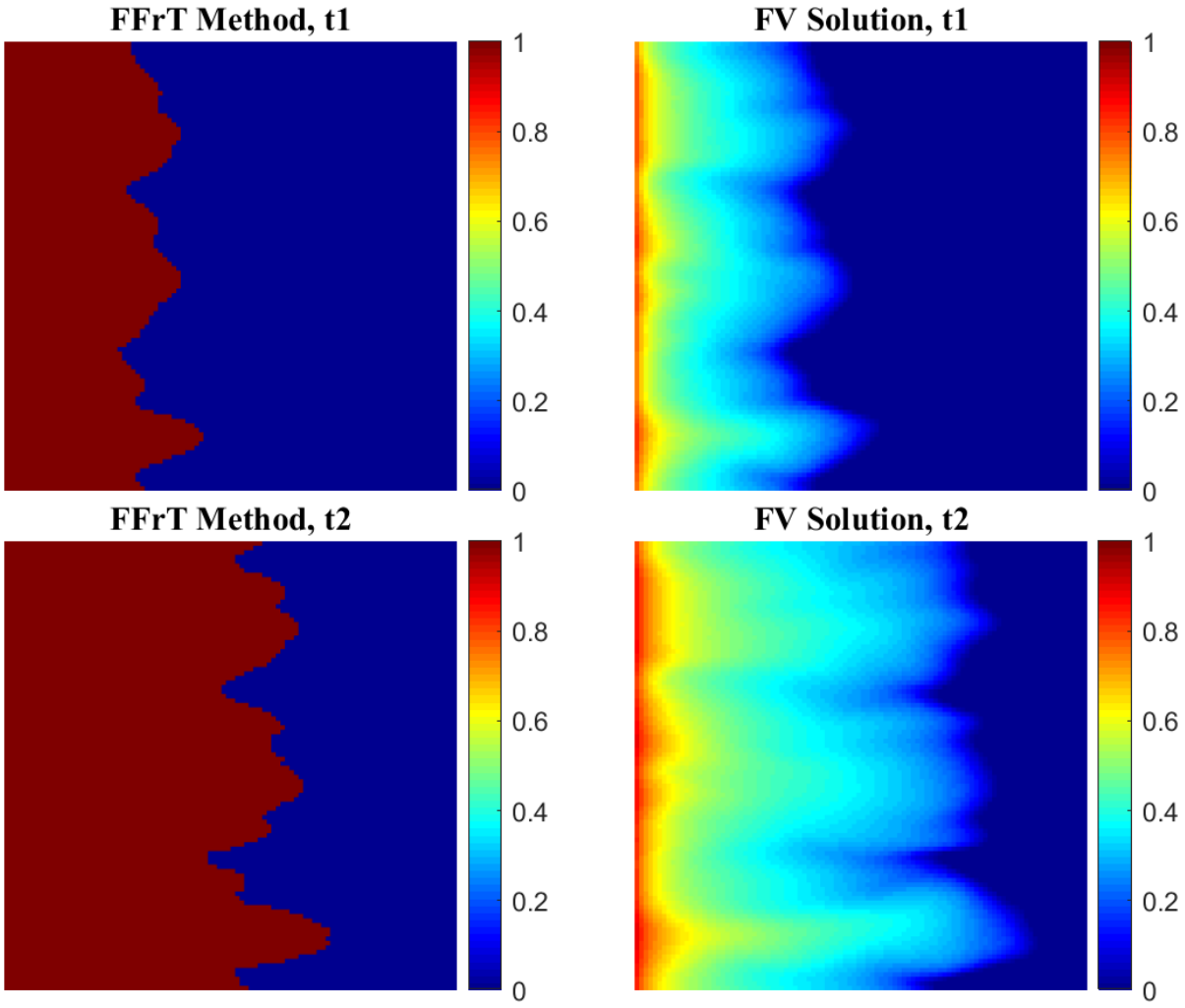

Figure 5.8: Water saturation maps for the first randomly generated permeability domain with a viscosity ratio of 10 at two different time steps, computed using the FFrT and the FV methods.

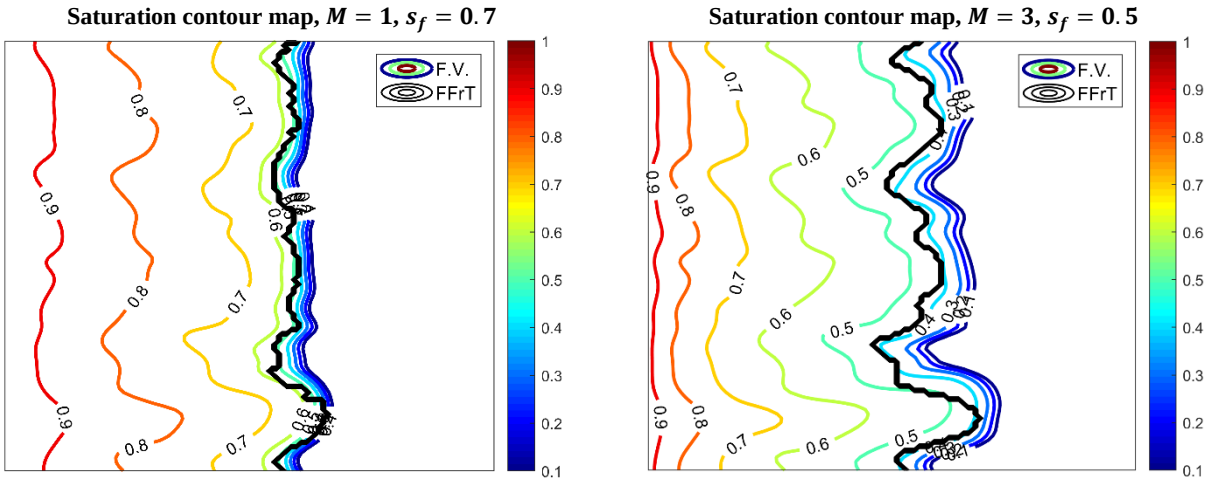

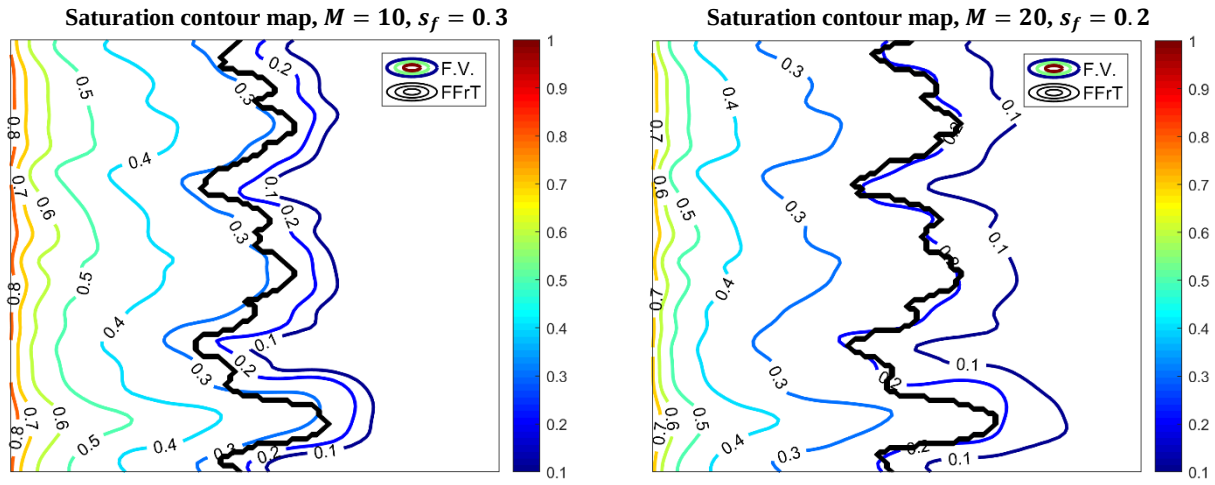

Figure 5.9: Water saturation contour maps for the first randomly generated permeability domain with different cases of viscosity ratio, computed with the proposed FFrT method and a standard FV scheme.

The water saturation maps and contour maps for the viscosity ratios of 1 and 10, on the more heterogeneous permeability domain of case two, are shown in Figure 5.10. In this case, the FFrT method is also successful. For $M = 10$, the results of the FFrT method are closer to the saturation contours of 0.3. To better represent the smearing of the front in numerical simulations, Figure 5.4 shows the saturation profiles for a homogeneous domain, using the FV numerical method in two high and low-resolution grids. It is also worth noting that the proposed fast front tracking method cannot predict the rarefaction wave behind the front and the numerical diffusion at the front. The essential fact is that the frontal zone is captured correctly. This allows to set-up correctly the adaptive coarsening strategy with the FFrT method used as a criterion, which is our main goal in the proposed workflow.

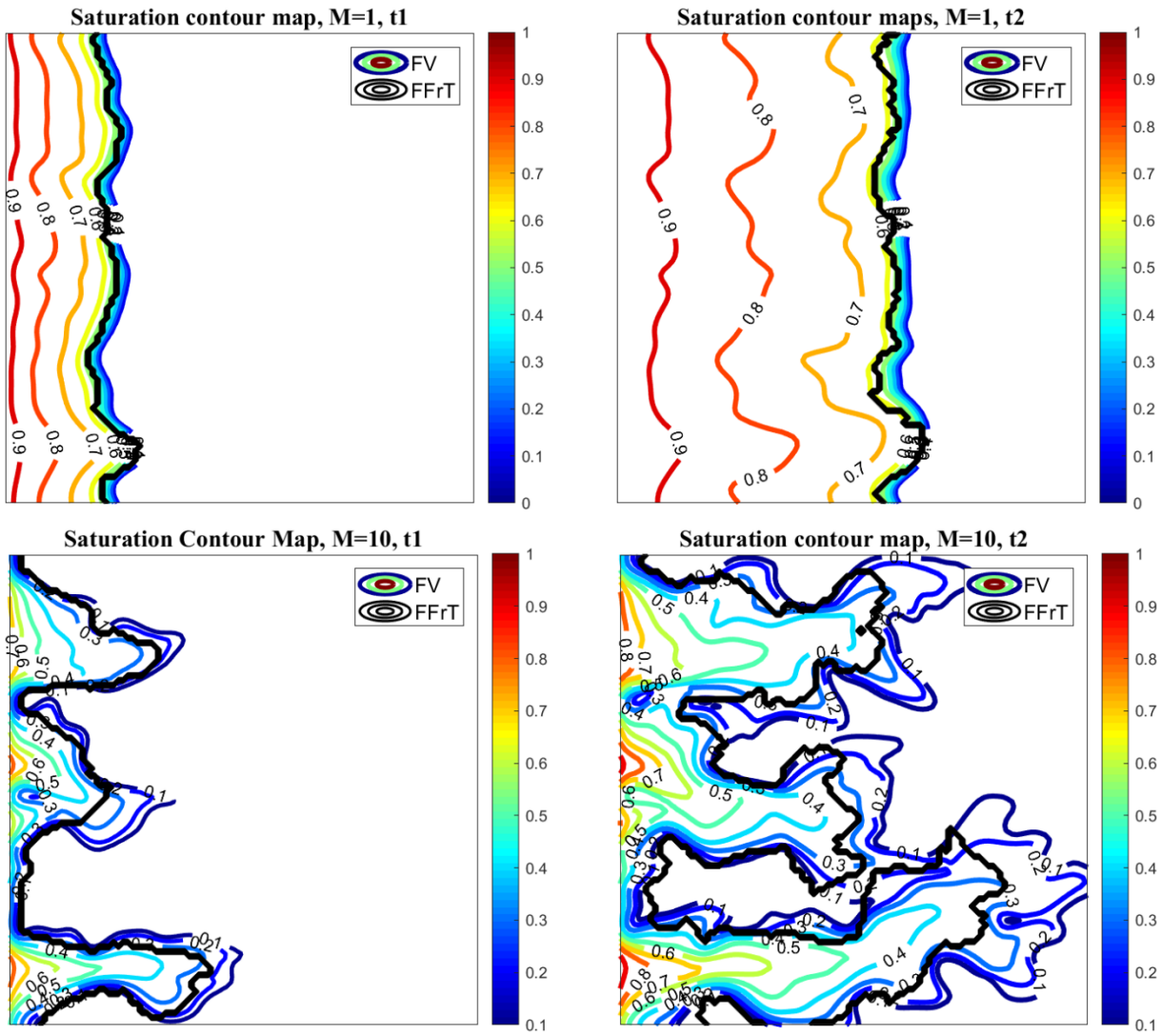

Figure 5.10: Water saturation contour maps for the second randomly generated permeability domain with two viscosity ratio cases of 1 and 10 at two different time steps, computed by the FFrT method and a standard FV scheme.

5.3.4 **SPE10 benchmark test**

Now, we test the method on two-dimensional Cartesian models with permeability values taken from different layers of the second SPE10 benchmark test (Christie and Blunt, 2001). We consider the same immiscible two-phase flow problem with different viscosity ratios. We select layers 22 and 70, from Tarbert and Upper Ness formations. We generate the coarse grid via a uniform agglomeration of the base fine grid, with an agglomeration ratio of 10. We use a flow-based upscaling method to compute the upscaled permeabilities (Chen et al., 2003), where a set of representative boundary conditions are imposed at the coarse grid blocks to solve the flow

equation and use the fine-scale pressure and fluxes to compute the upscaled permeabilities. The fine-scale and upscaled permeability maps for the layers 22 and 70 of the SPE10 dataset are shown in Figure 5.11.

In Figure 5.12 we compare the FFrT method with a standard finite volume scheme at two resolutions, for a waterflood problem with a viscosity ratio $M = 10$ in layer 22 of the SPE 10 model. At the coarse scale, the results of FFrT method are very close to the FV solution of the same resolution. In fine-scale simulations, the FFrT method predicts the flow patterns very well, and the main difference with the fine-scale simulation is close to the right boundary, where the front becomes diffusive. For a more detailed comparison, the superimposed contour maps of the original resolution case are shown in Figure 5.13. This figure shows that the predicted front position is very close to the saturation contour line of 0.3, computed using the FV scheme on the original grid.

Figure 5.14 shows the water saturation maps and contour maps for the same waterflood problem in layer 70, at the original resolution. This layer, with a channelized pattern of sandstone in a low permeable shale background, is a challenging example to test the method in the presence of fingerings and channellings. The FFrT method gives similar results in most parts of the domain, to the FV method.

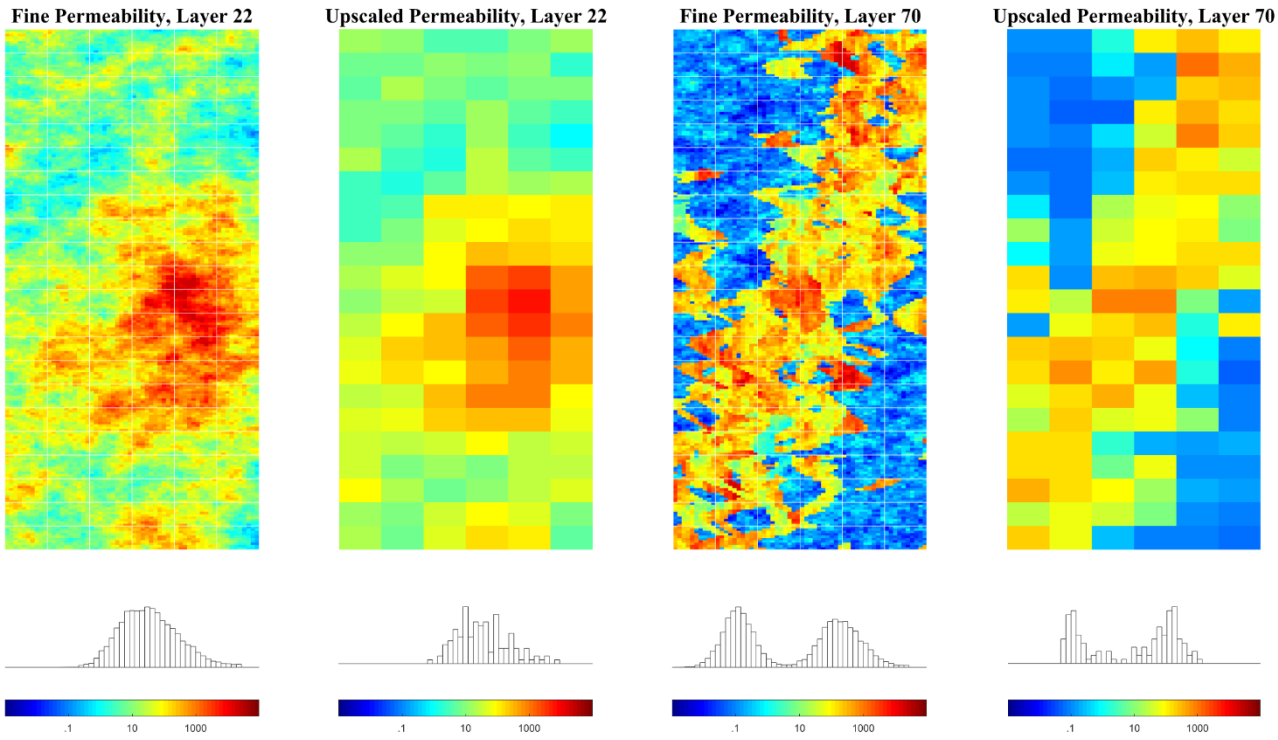

Figure 5.11: Permeability maps of the layers 22 and 70 of the SPE10 model in the logarithmic scale, before and after upscaling

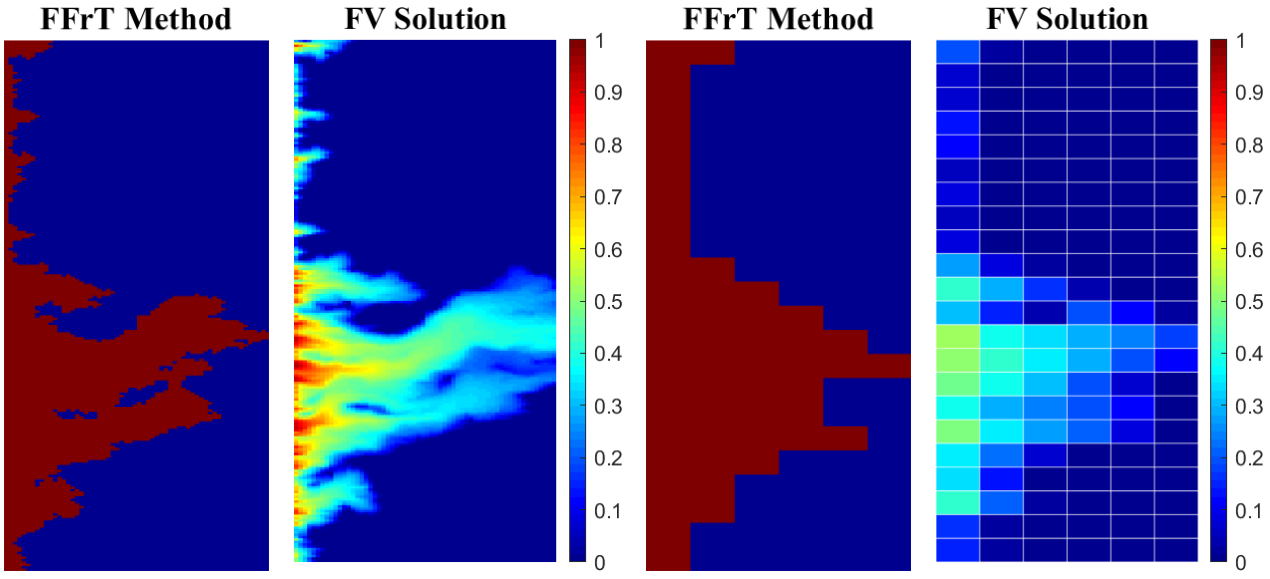

Figure 5.12: Water saturation maps for layer 22 of SPE 10 model for a waterflood problem with a viscosity ratio of 10 for the original and the coarsened resolution, computed by the FFrT and FV methods.

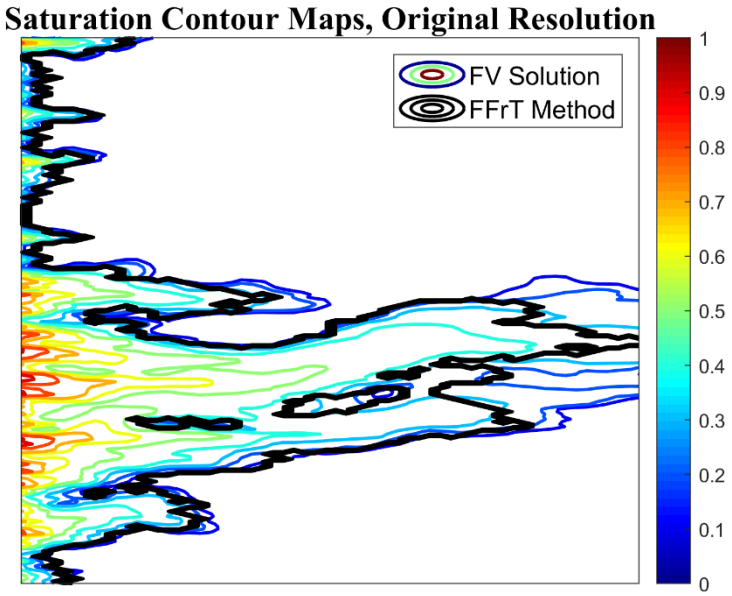

Figure 5.13: Water saturation contour maps for layer 22 of SPE 10 model, at the same time step, on the original fine grid.

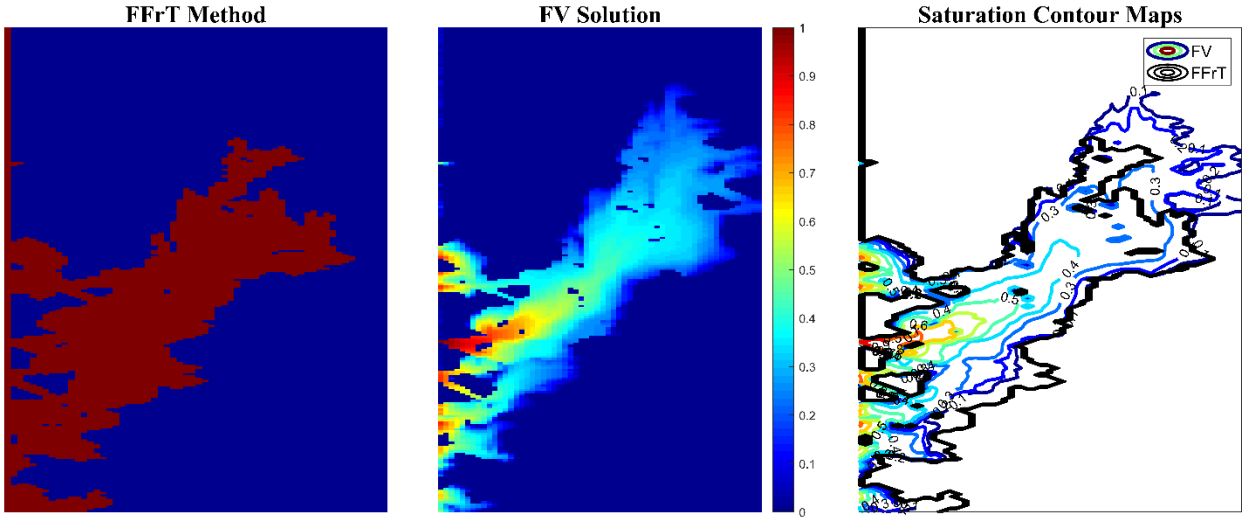

Figure 5.14: Water saturation maps and the superimposed contour maps for layer 70 of the SPE10 model with a viscosity ratio of 10 at the original resolution, computed by the FFrT method and the FV scheme.

We have not compared the computational times between the FFrT method and other standard FV methods. The reason is that we have developed this method with MATLAB, which is a scripting language. The focus of our work at this stage is not to develop an optimized code, but rather the prototype that validates the proposed method. Another solution for performance

evaluation would be to compare the number of unknowns to be solved for each method. These comparisons are included in the next chapter. It is worth mentioning that the equation of advance of the front is an explicit equation to be solved only at the location of the front.

In all the examples of this chapter, we use the FFrT method as an independent simulator. At each time step, after the resolution of the pressure equation, the front advance equation is solved in some parts of the domain where the front is present. Another approach is to use the total flux values derived from a standard pressure solver. For this approach, steps (1) and (2) of the FFrT algorithm are not performed and the method is used after the solution of the pressure equation to predict the position of the front. This approach is tested in the next chapter.

6 Combining FFrT with adaptive coarsening: A proposed approach for immiscible multiphase flows

In this chapter, we detail the formulation and implementation of the proposed solution procedure, using the finite volume and discontinuous Galerkin discretization schemes, the FFrT method, and an adaptive coarsening approach. Next, we discuss the complexity and computational effort of all steps of the proposed algorithm. Finally, we analyse different aspects of this solution strategy and discuss its advantages and limitations through numerical examples.

6.1 Formulation

Starting from a field-scale geostatistical model with petrophysical properties and a fluid model with the associated governing equations as described in chapter 2, the fluid flow problem can be transformed to a numerical simulation by using the discretization methods reviewed and described in chapters 3 and 4. The next step is to generate a coarse grid from the high-resolution grid of the geostatistical model. In this work, the agglomeration-based coarsening approach is used, both for the generation of a base low-resolution grid over the whole domain and for an adaptive coarsening during the simulation. In the agglomeration-based coarsening approaches, a coarse grid is generated from the agglomeration of the fine grid by using a partition vector to relate coarse blocks to their underlying fine cells. Throughout this thesis, two-dimensional Cartesian models are used, and the base coarse grid is generated through a uniform agglomeration of the original fine grid. An illustrative example of uniform partitioning of the Cartesian topology is shown in Figure 6.1 for the coarsening of a 6×6 fine grid to a 2×2 coarse grid. A partition vector (π), as already defined in chapter 3, is an integer-valued vector such that $\pi(c) = b$, if cell c in the fine grid belongs to block b in the coarse grid. For this example, the partitioning gives a 36×1 vector that takes one of the 1,2,3,4 values for each cell in the fine grid:

$$\pi = [1,1,1,2,2,2,1,1,1,2,2,2,1,1,1,2,2,2,3,3,3,4,4,4,3,3,3,4,4,4,3,3,3,4,4,4]$$

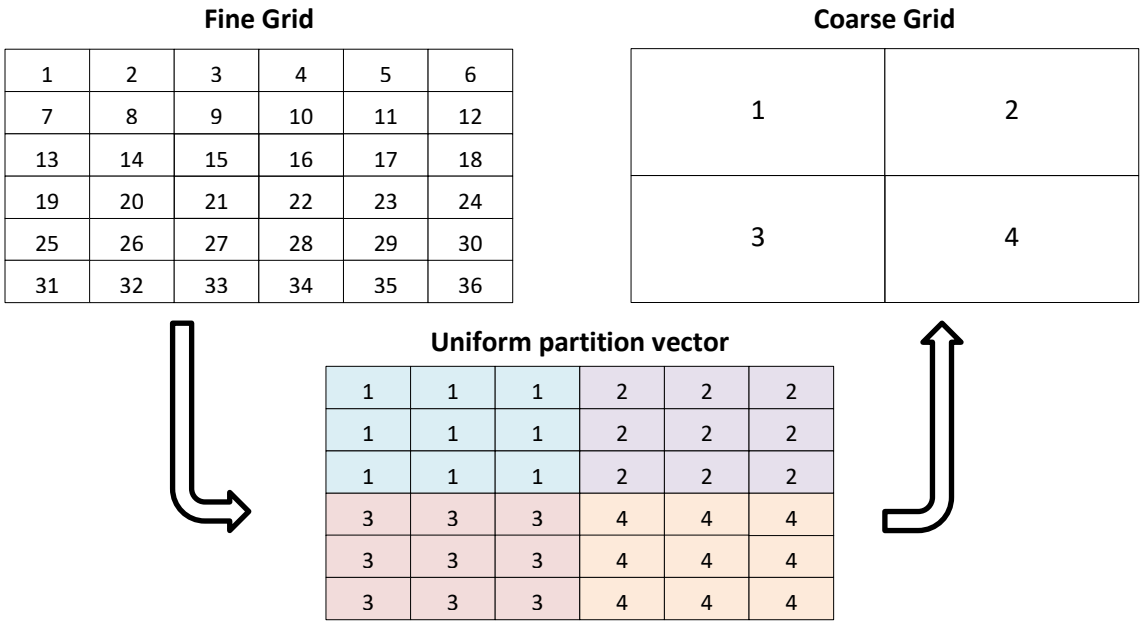

Figure 6.1: Coarsening of a 6×6 fine grid to a 2×2 coarse grid through a uniform partitioning.

Representation of coarse grids with the partition vector has many advantages compared to an independent generation of low-resolution grids. First, this approach allows the generation of non-uniform coarse grids that better preserve the complex geometry of the fine grid and better adapt to the geological features. Next, another important advantage lies in the dynamic coarsening for increasing or decreasing mesh resolution during the numerical simulation. Thanks to the preserved one-to-one mapping between fine and coarse grids, adding or removing local resolution is simple to carry out. We explore this advantage, which is related to this work, using the example of Figure 6.1 in more detail. To increase the local resolution of the fourth coarse block to its original fine resolution, the corresponding partition vector elements need to be replaced with a partition vector associated with the coarsening ratio 1 (see Figure 6.2). First, we mark the fourth coarse grid block:

$$markedBlocks = [false, false, false, true]$$

Next, we determine the underlying fine grid cells of the marked coarse block:

$$cells = markedBlocks(\pi)$$

Last, the partition vector is modified by simply assigning new integer values to the partition values of the corresponding fine grid cells:

$$\pi(cells) = 4 + [1{:}\, sum(cells)].$$

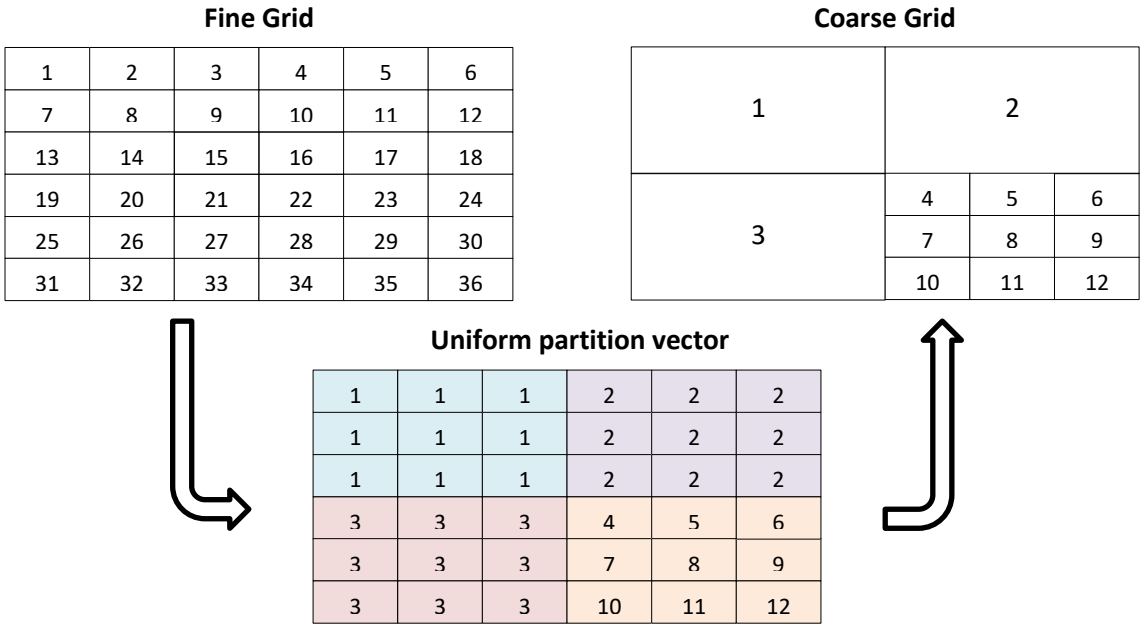

Figure 6.2: Illustration of adding high resolution to block 4 of the coarse grid.

After the coarsening of the original fine grid, petrophysical properties and parameters are propagated from the base fine grid to the coarse grid. Upscaling of additive properties like the porosity and the pore volume are straightforward, as already mentioned. For permeability upscaling, we use the flow-based upscaling approach, in which the flow equation is solved at the fine scale in subdomains specified by the coarse grid blocks. The prescribed pressure boundary conditions are set in the direction of the flow and no-flow boundary conditions are applied elsewhere. The fine-scale approximated pressure and fluxes are used to compute the upscaled permeabilities.

As an illustrative example, we detail the algorithm with case one from random permeability fields illustrated in Figure 5.6. We consider a two-dimensional waterflood problem, where water is injected from the left boundary of the domain. The reservoir is initially fully saturated with oil. Water and oil viscosities are equal to 1.0 and 0.2 cp, respectively. Both fluids are incompressible. A coarse grid is generated by uniform agglomeration of the original grid with

a coarsening ratio of 10. This simple example, with a sharp and smooth front, shows how the proposed approach works. Figure 6.3 illustrates the base coarse grid and the upscaled permeability computed by a pressure drop flow-based upscaling approach.

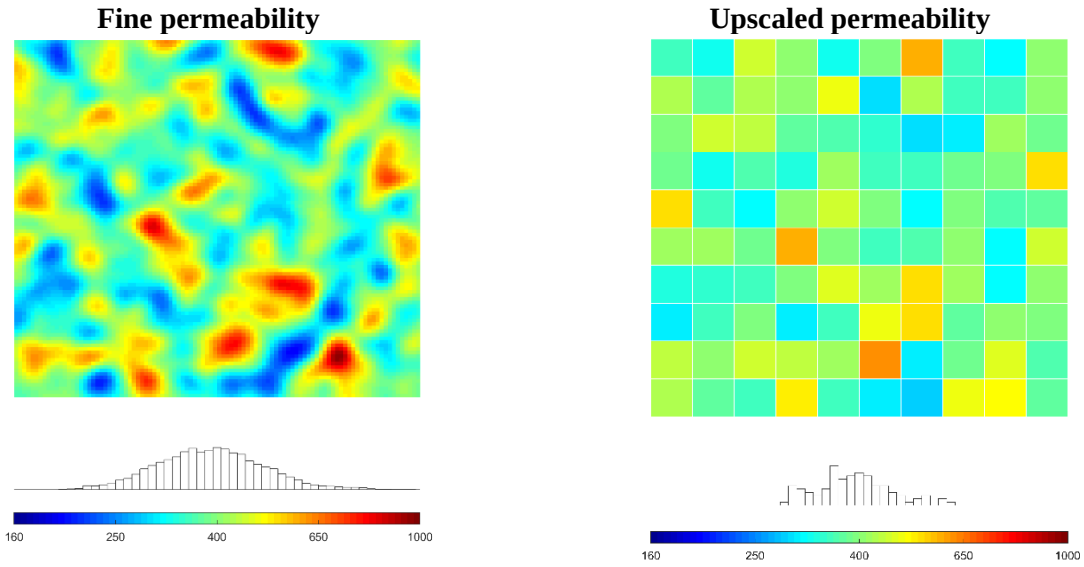

Figure 6.3: Isotropic randomly generated permeability model with a dimensionless correlation length of 0.1 and a Dikstra-Parson coefficient of 0.2, before (left) and after (right) upscaling.

Now, suppose we are at time step n of the simulation. Below is the flowchart of the proposed solution strategy for each time step:

(1) Pressure solution on the base coarse grid over the whole domain:

The pressure equation is solved using the DG scheme with a linear approximation on the base coarse grid over the whole domain. DG conservative fluxes are reconstructed using Eq. 4.38. The outputs of this step are updated approximated pressure and conservative total fluxes in the base coarse grid.

(2) Fast front tracking method:

Using the conservative total fluxes of the previous step, the FFrT method is implemented to move the front in the base coarse grid. This step includes solving Eq. 5.9 in some parts of the domain. This method gives the predicted position of the front and the coarse blocks where a part

of the front is present. Figure 6.4 shows the position of the front in the base coarse grid after 600 days. The front position in the original fine grid and the water saturation map computed by the FV sequential implicit scheme in the fine grid are also shown as references.

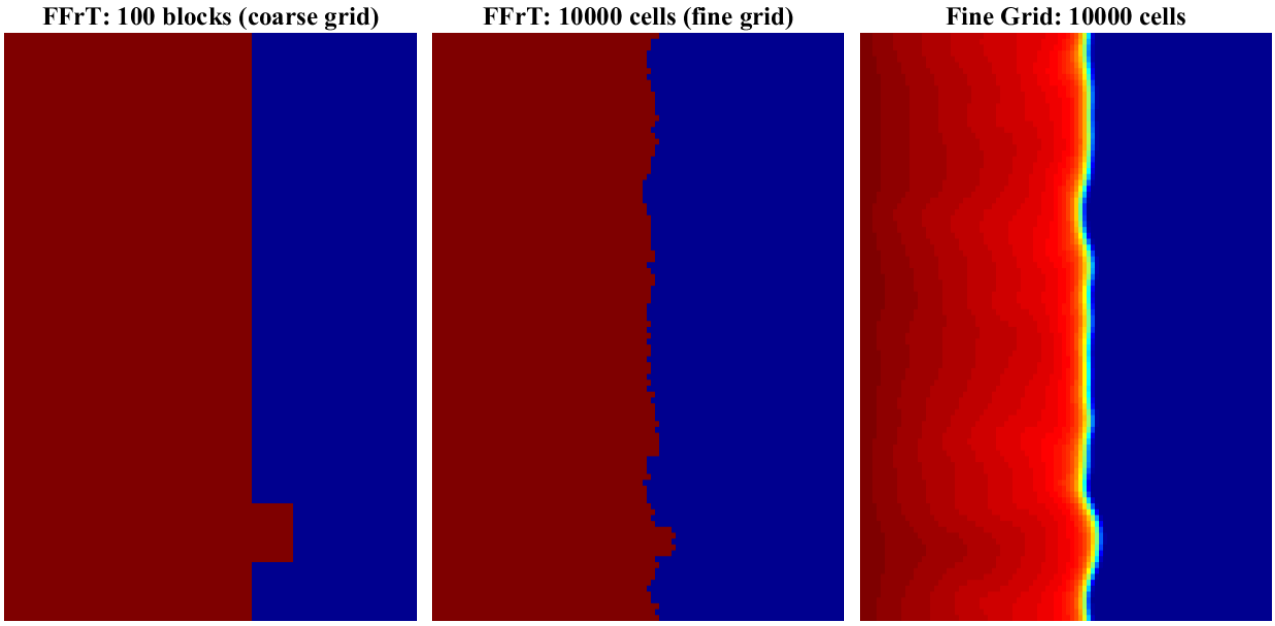

Figure 6.4: Position of the front after 600 days computed using the FFrT method on coarse and fine grids are presented in the left and middle plots, respectively. The water saturation map computed with the FV sequential implicit scheme is shown in the right plot, as reference.

(3) Domain decomposition and adaptive coarsening:

The position of the front is then used to (1) decompose the domain into single and multiphase flow regions and (2) use a higher resolution grid, equal to the resolution of the original fine grid or an intermediate resolution, where the front moves. One immediate advantage of domain decomposition is to solve the saturation equation only in the multi-phase flow region. As a result, no multiphase upscaling method is needed.

To decompose the domain into single-phase and multiphase flow regions in a two-dimensional simulation, we determine the left and right boundaries of the multiphase flow region. The right boundary is determined by the farthest block on the right containing the front in the direction of the flow. The left boundary is determined by the maximum position in the flow direction before which the front is not actively moving. The top and bottom boundaries coincide

with the outer boundaries of the domain. Figure 6.5 shows these boundaries for this illustrative example where green lines represent the boundaries of the two-phase flow region.

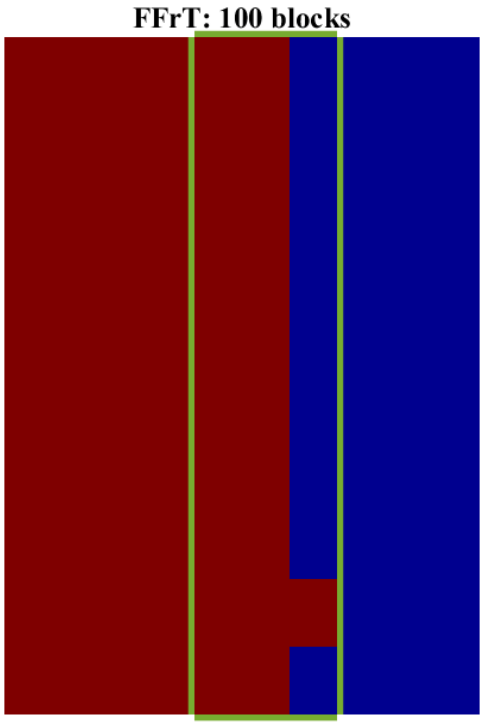

Figure 6.5: Two-phase flow region (green lines) determined using the predicted front position.

After decomposing the domain, we use the adaptive coarsening approach to use a higher-resolution grid where the criterion is met. The coarsening approach of Hauge et al. (2012) is used and the coarse blocks with the active front are taken as the criterion. These coarse blocks are marked to stay at a higher resolution, while the single-phase coarse blocks are coarsened to the resolution of the base coarse grid. Figure 6.6 shows the generated non-uniform grid using this approach with the FFrT method as the criterion.

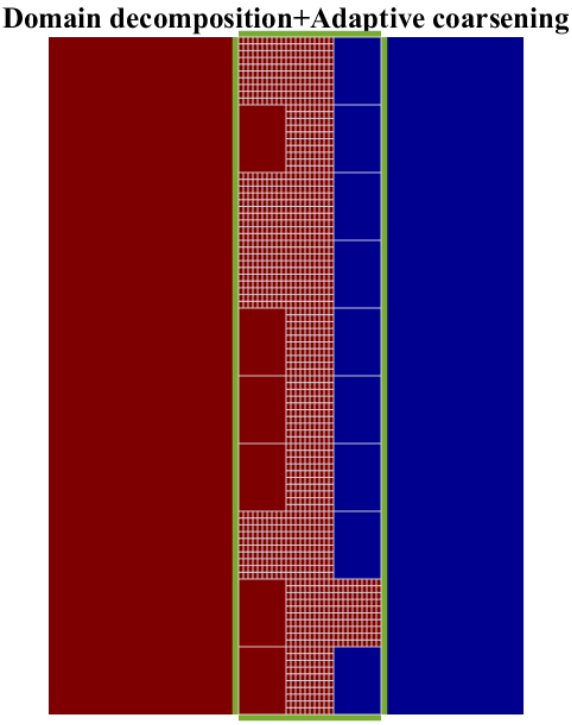

Figure 6.6: Generated non-uniform grid in the multiphase flow region using the adaptive agglomeration based coarsening method with the FFrT method used as the coarsening criterion.

(4) Flow and transport solution in the multiphase flow region:

Flow and transport problems are solved in the multiphase flow region of the domain, in the subgrid generated at the previous step, using the finite volume sequential implicit (IMPIMS) scheme. The boundary conditions to solve the flow and transport equations in the multiphase flow region depend on the type of faces. If one of the left or right boundaries coincides with the main boundaries of the domain, the prescribed pressure boundary conditions are set for both left and right boundaries of the multiphase region. If both left and right boundaries are internal, the conservative fluxes are set as boundary conditions. For the top and bottom boundaries, the homogeneous no-flow condition is used in all cases in this work. Figure 6.7 shows the water saturation maps obtained with both domain decomposition and dynamic non-uniform coarsening.

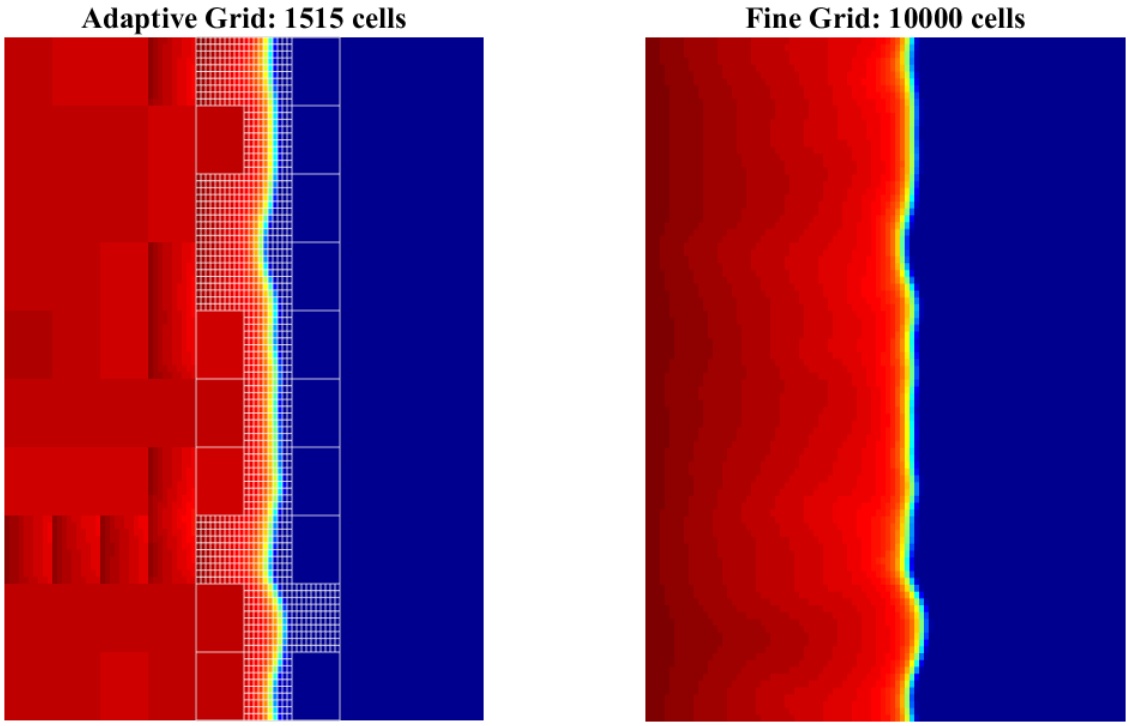

Figure 6.7: Water saturation maps computed using the proposed solution strategy and the FV sequential implicit solution in the base fine grid (reference) are represented in left and right plots, respectively.

Except for the DG and the FFrT methods, our methodology uses tools for the upscaling, the dynamic mesh coarsening, and the FV resolutions that are available in the MATLAB Reservoir Simulation Toolbox, MRST[4] (Lie, 2019; Lie et al., 2012). A flowchart of the proposed approach at each time step is illustrated in Figure 6.8.

[4] https://www.sintef.no/projectweb/mrst/

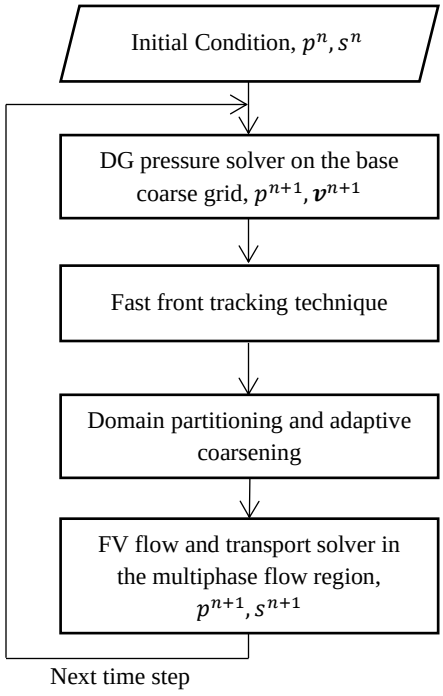

Figure 6.8: Flow chart of the proposed sequential approach for each time step

6.2 Complexity analysis

We use the number of unknowns solved at each step as the main indicator of the complexity of the solution approach so that this analysis does not depend on the actual implementation of the method. In the following, we detail the computational cost of each step separately.

(1) Pressure solution on the base coarse grid over the whole domain:

In the proposed approach we use the DG scheme to solve the pressure equation. In this case, the number of unknowns is equal to the number of grid blocks in the coarse grid times the number of local degrees of freedom. The number of local degrees of freedom, denoted by N, is equal to:

$$N = (P + 1)^2 \qquad \text{Eq. 6.1}$$

where P is the polynomial degree. In the case of using the FV scheme, the number of local degrees of freedom is equal to one and the total number of unknowns is equal to the number of coarse grid blocks.

(2) Fast front tracking method:

In this step, Eq. 5.9 is solved in parts of the domain where the front is present, and the number of unknowns depends on the shape of the front. The explicitness of the equation to be solved and being local to cells with the front are two important features that make this step computationally very fast.

(3) Domain decomposition and adaptive coarsening:

It is difficult to quantify the complexity of adaptive coarsening algorithm. However, in test cases we performed this step was less than about five per cent of the overall computational time. It is worth noting that this dynamic coarsening reduces the number of unknowns in the computationally demanding transport solver.

(4) Flow and transport solution in the multiphase flow region:

The number of unknowns in this step is twice the number of cells in the two-phase flow region.

Figure 6.9 shows the ratio of the total number of global degrees of freedom in the proposed approach compared to the reference solution for the same example. The total number of global degrees of freedom in the reference solution is equal to twice the number of grid cells in the original fine grid.

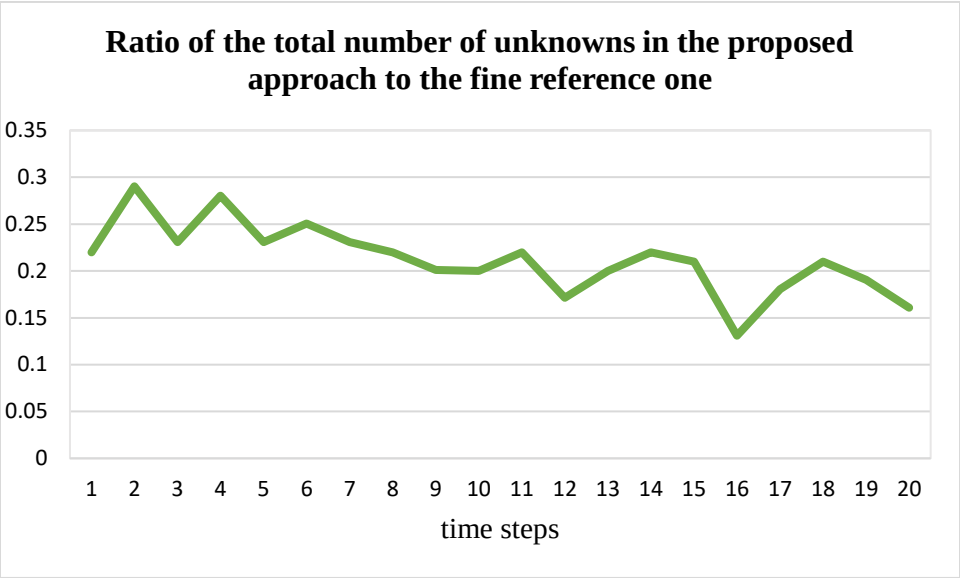

Figure 6.9: Ratio of the total number of unknowns to be solved at each time step in the proposed solution approach compared to the fine reference solution.

6.3 Numerical examples

To test and analyse the different aspects of the proposed solution strategy different two-dimensional water-flood problems are considered, where water is injected from the left boundary of the domain. Both fluids are incompressible. The reservoir is initially fully saturated with oil. Dirichlet conditions on the left ($XMIN$) and right ($XMAX$) boundaries are imposed, while and a no-flow condition is applied on the top ($YMAX$) and bottom ($YMIN$) boundaries. In all the following examples, the base coarse grid is generated via a uniform agglomeration of the original fine grid, with an agglomeration ratio of 10. A flow-based upscaling method is implemented to compute the upscaled permeabilities. In these examples, we aim to test different aspects of the proposed solution strategy, from step (1) to step 0, and compare them with other existing methods. In the last two examples, the proposed approach is tested in different layers of the SPE10 test case for favourable and unfavourable displacement processes. In all the following examples, the reference solution is set as the finite volume sequential implicit scheme on the original fine grid.

6.3.1 **Numerical example one: Pressure solution on the base coarse grid**

The main objective of this example is to test different pressure solvers in the first step of the proposed algorithm. At each time step, the pressure equation is solved on the base coarse grid and the approximated new fluxes are used (1) to advance the front using the FFrT method and (2) as boundary conditions for solving the pressure and saturation equations in the multiphase flow region in a higher resolution subgrid. We compare the TPFA FV and the DG scheme with the order of approximation 1. In this example, we take case two of randomly generated permeability fields in the example 5.3.3. Oil and water viscosities are set to 5 cp.

Figure 6.10 shows the water saturation maps at three different time steps, computed using the proposed adaptive solution strategy, where the marked coarse blocks containing the front are replaced with their underlying original fine grid cells. In the first column, the DG scheme with the approximating polynomials of order one is used to solve the pressure equation in the base coarse grid. In the second column, the TPFA FV scheme is used as the coarse-scale pressure solver. The last column shows the fine-scale FV solution as reference. This figure shows that the FFrT method using DG conservative fluxes gives better results in terms of domain decomposition and determination of the right boundary of the two-phase flow region. In terms of adaptive coarsening criterion, the FFrT method performs the same either using the FV or the DG computed fluxes.

The water cuts and the relative L1 saturation errors for these solution strategies are represented in Figure 6.11 and Figure 6.12, respectively. Comparison of the adaptive solution method using FV and DG total fluxes shows a greater difference between two approaches in the water cut than in the L1 saturation relative error. The reason might be that the prediction of the right boundary of the two-phase flow region is more accurate in the adaptive scheme with the DG pressure solver. These plots also include the water cut and the relative error for two coarse-scale solution schemes. In these solution schemes, the saturation equation is solved using the FV implicit formulation, while the pressure equation is solved using the FV method in one and the DG method in the other. Comparing these two coarse-scale solutions shows that the error is relatively similar in both schemes compared to the reference solution. The difference between

these approaches is larger in terms of water cut. The water cut is overestimated in the DG scheme while it is underestimated in the FV scheme.

In the rest of this work, we use the DG discretization method with the order of approximation one to solve the pressure equation on the base coarse grid.

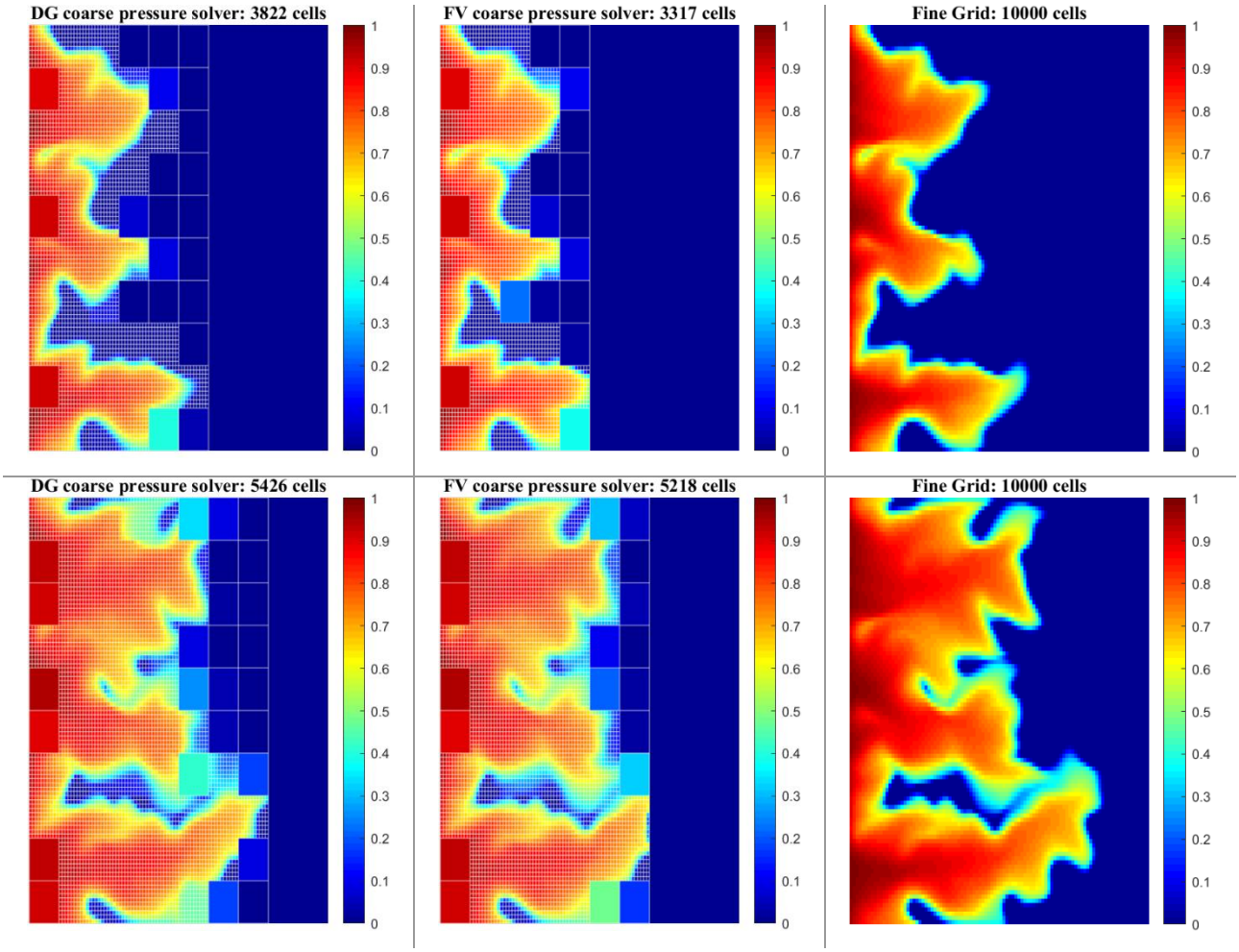

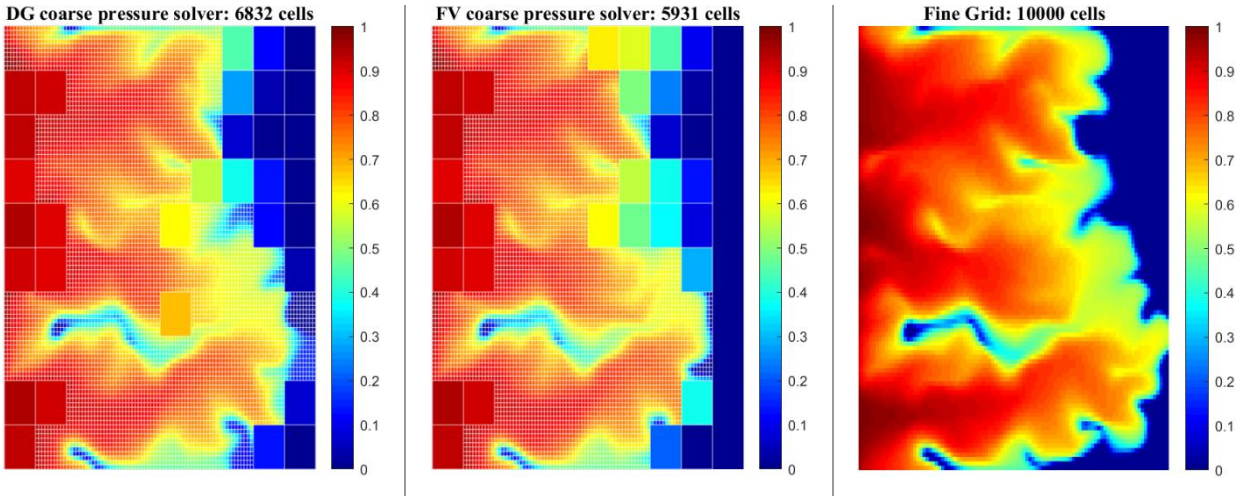

Figure 6.10: Water saturation maps at three different time steps, computed using the adaptive solution strategy with different coarse-scale pressure solvers. In each row, the first plot shows the results of using the DG method, the middle plot shows the results of using the FV method. The plots on the right are fine FV reference solutions.

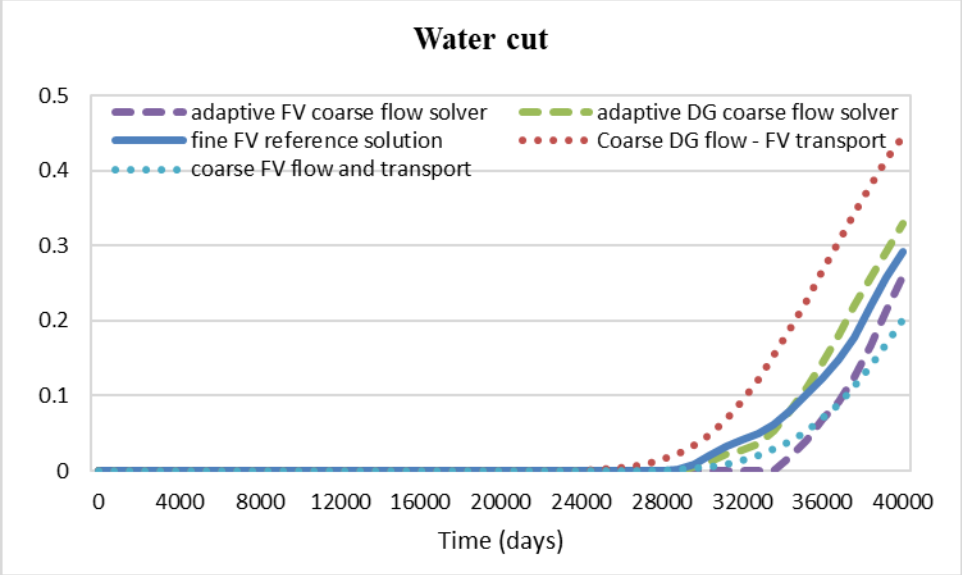

Figure 6.11: Water cut obtained with different solution schemes for case two of randomly generated permeability fields with a viscosity ratio of 1.

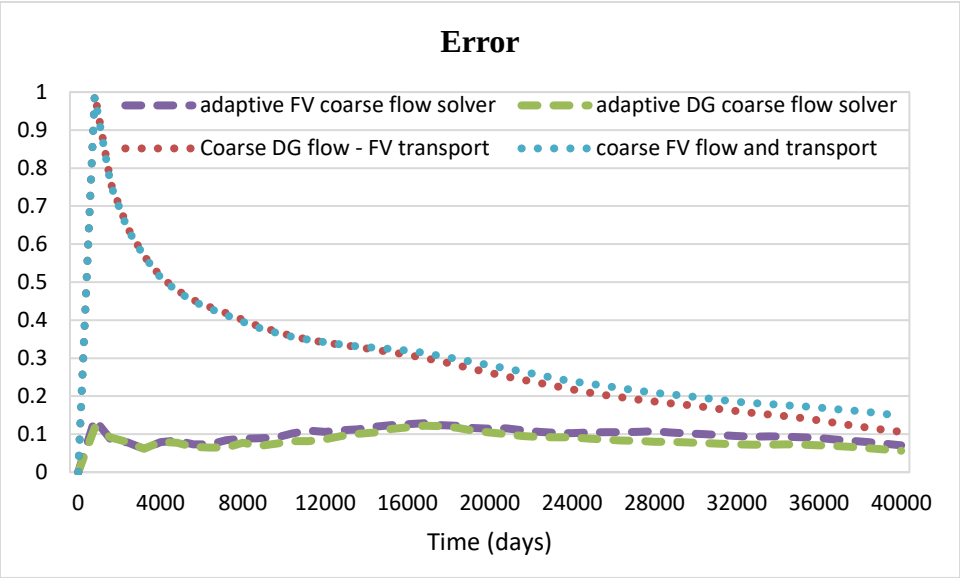

Figure 6.12: Relative L1 saturation error for different solution schemes in the randomly generated permeability field case two.

6.3.2 **Numerical example two: Adaptive coarsening criterion**

In this example, we compare the FFrT method with a classic coarsening criterion, the saturation difference with the previous step. For this criterion, after solving the pressure equation in the base coarse grid using the DG scheme, the saturation equation is solved at the coarse scale over the whole domain using the implicit FV scheme. The saturation difference between the new and the previous time step is used as the coarsening criterion. The mesh resolution in the blocks where this saturation difference exceeds a defined tolerance is increased to a higher resolution. In this example, the adaptive solution approach using this saturation criterion is tested in the same flow problem as in the previous numerical example of page 99. We set the saturation tolerance to 0.001

Water saturation maps are illustrated in Figure 6.13, at the same time steps. As it can be observed, all the grid blocks containing the displacing fluid have been replaced with their underlying original fine grid cells. However, some of the single-phase blocks in the unswept regions are also marked to remain in high resolution with this coarsening criterion. This phenomenon can be linked to the greater numerical diffusion associated with solving the transport equation in low-resolution grids. Figure 6.14 shows the water cuts for this scheme, the

adaptive schemes described in the previous example, and the base fine solution. Figure 6.15 presents the relative L1 saturation errors for these different solution methods. These two figures confirm that the FFrT method using the DG fluxes provides a satisfying accuracy in terms of the water breakthrough time, the water cut, and the relative error, with the small cost of solving an explicit equation in some parts of the domain. The saturation criterion gives the most accurate results, but as already stated, do not perform optimized in adaptive coarsening. The computational cost of the saturation criterion is also larger compared to the FFrT method. We do not include the CPU times of each approach due to its probable dependence on the implementation, but it should be noted that the cost of solving the transport equation even in a low-resolution grid is not negligible and can impact the overall efficiency of the solution method. Figure 6.16 shows the ratio of the total number of unknowns in the three mentioned adaptive solution algorithms to the total number of unknowns in the fine reference solution. The proposed solution method with the FFrT method using the DG total fluxes gives a satisfactory accuracy while maintaining a suitable computational efficiency represented by the number of global degrees of freedom.

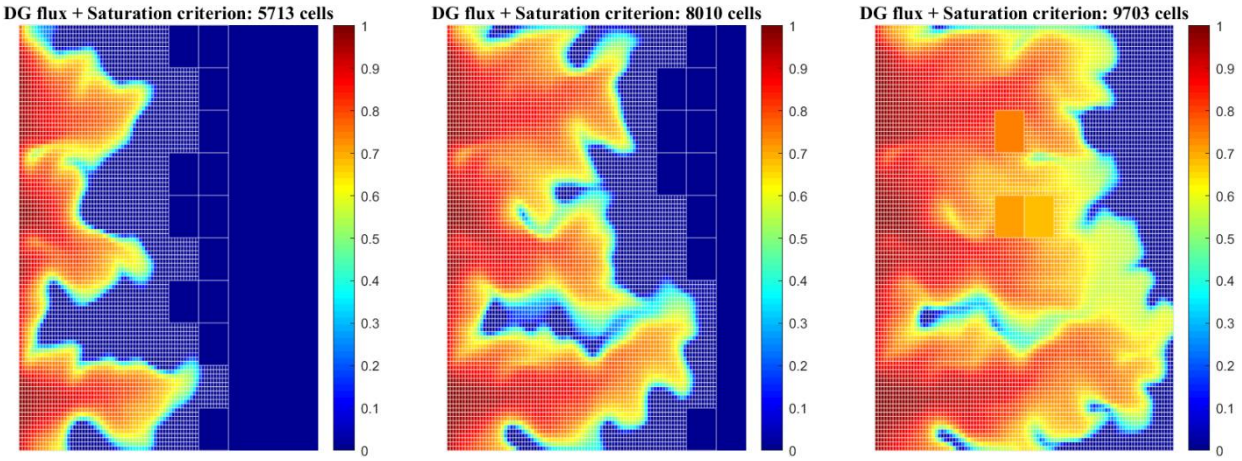

Figure 6.13: Water saturation maps computed with the adaptive solution strategy using the saturation gradient as the coarsening criterion.

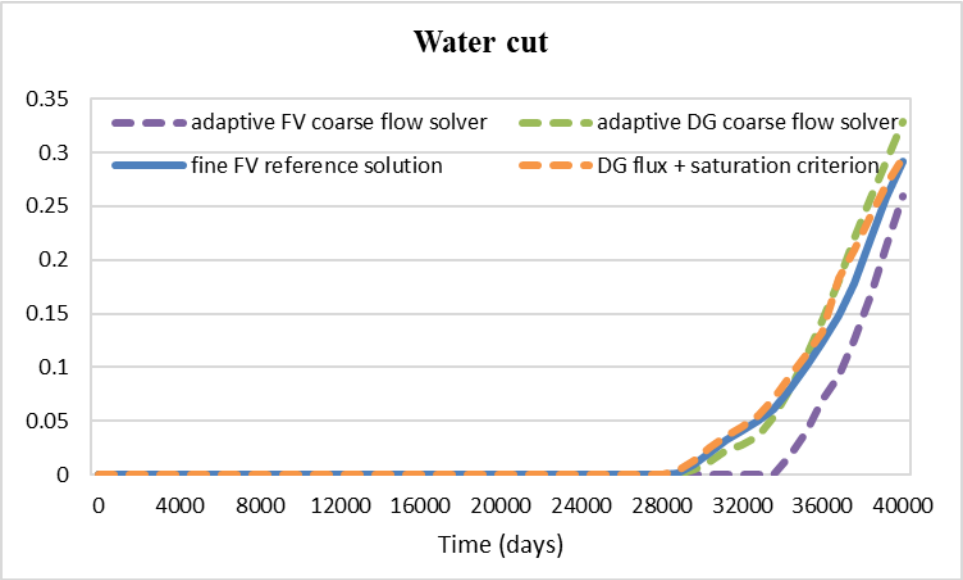

Figure 6.14: Water cut in the fine-scale FV reference solution (blue), and different adaptive solution strategies: the coarse-scale FV pressure solver and the FFrT method (violet), the coarse-scale DG pressure solver and the FFrT method (green), and the coarse-scale DG pressure solver with the saturation criterion (orange).

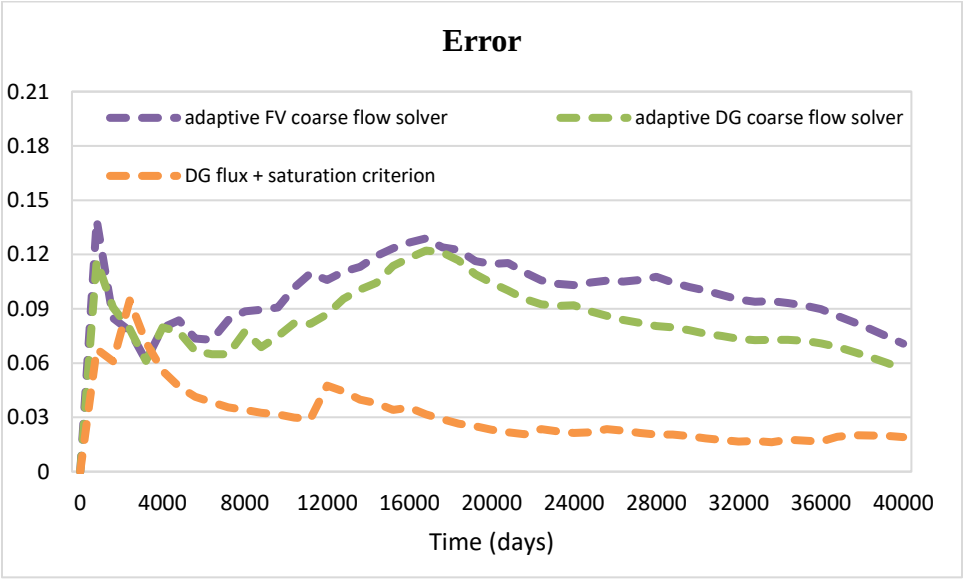

Figure 6.15: L1 saturation error relative to the base fine FV solution for different adaptive solution strategies; the coarse-scale FV pressure solver and the FFrT method (violet), the coarse-scale DG pressure solver and the FFrT method (green), and the coarse-scale DG pressure solver with the saturation criterion (orange).

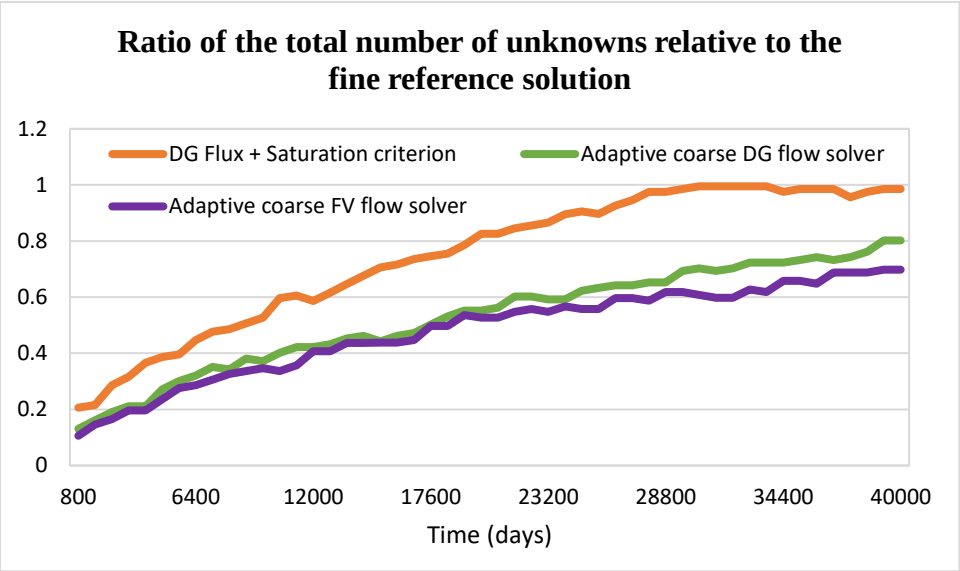

Figure 6.16: Total number of unknowns in each time step for different solution approaches relative to the total number of unknowns in the base fine solution.

6.3.3 **Numerical example three: Domain decomposition**

After advancing the front with the FFrT method, the new position of the front is used to identify the multiphase flow region and generate a non-uniform grid with the adaptive coarsening approach. To decompose the domain into single-phase and multiphase flow regions, the left and right boundaries are determined, as explained in section 6.1 (page 92). The left boundary of this rectangular-shaped multiphase region is determined by the most advanced position, in the flow direction, before which the front is not actively moving. Another approach is to use the saturation difference between the two previous time steps s^n and s^{n-1}, to coarsen the high-resolution single-phase regions behind the front and to determine the left boundary of the multiphase region. We test here this approach on the same test case as in the illustrative example described in section 6.1 (page 95).

The water saturation map is presented in Figure 6.17, at the same time step. The number of global degrees of freedom for the proposed solution method, using two approaches of domain decomposition, is plotted in Figure 6.18. The first approach uses the FFrT method while the second one operates with the saturation gradient described previously. The FFrT method seems more efficient, because of its lower total number of unknowns and its independency from the user-defined saturation tolerance.

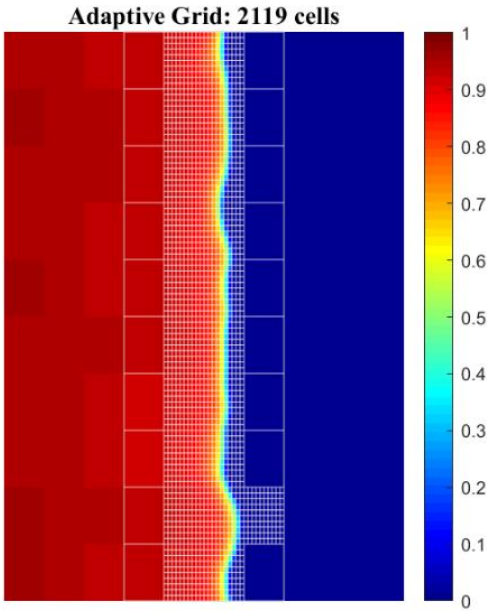

Figure 6.17: Generated non-uniform grid in the multiphase flow region using the saturation-based domain decomposition.

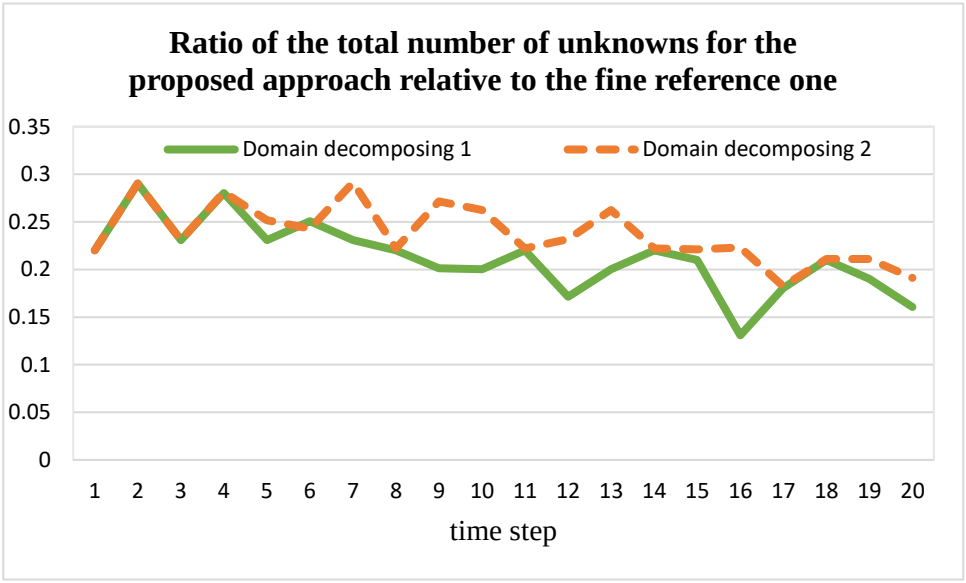

Figure 6.18: Ratio of the total number of unknowns, for two different domain decomposition approaches, to the total number of unknowns in the reference solution.

6.3.4 **Numerical example four: Non-uniform coarsening**

Another approach to increase the solution accuracy in the multiphase flow region could be to use a higher resolution grid uniformly in this region of the domain. In this approach, a high-

resolution grid, either the original fine grid or any chosen intermediate resolution grid, is used in the multiphase flow region. The intermediate resolution grid needs to be constructed only once in the pre-simulation step. In this case, the adaptivity step, which is the step (3) in the algorithm, only includes the domain decomposition and may become more computationally efficient. However, solving flow and transport equations in this uniformly high-resolution subgrid can be more computationally demanding.

In this example, we use a high-resolution grid in the multiphase flow region for the same test case described in section 6.1 (page 95). In this case, adaptive coarsening is not implemented, and the resolution of the multiphase flow region is increased to the original fine resolution.

Figure 6.19 shows the generated grid and the water saturation map, at the same time step as in the illustrative example. Figure 6.20 indicates the total number of unknowns, for the solution method, with and without non-uniform coarsening. This example, with a very sharp front, may be far from the real field complex multiphase problems but still can illustrate that a non-uniform coarsening approach helps to decrease the total number of unknowns through the coarsening of single-phase blocks without losing too much accuracy. The non-uniform coarsening step becomes more important in multiphase flows through heterogeneous channelled reservoirs where the front flows fast through the high-permeability layers while the low-permeability layers remain un-swept. Solving the transport equation in an adaptively coarsened grid is generally more computationally efficient, at an acceptable cost of adaptive non-uniform coarsening.

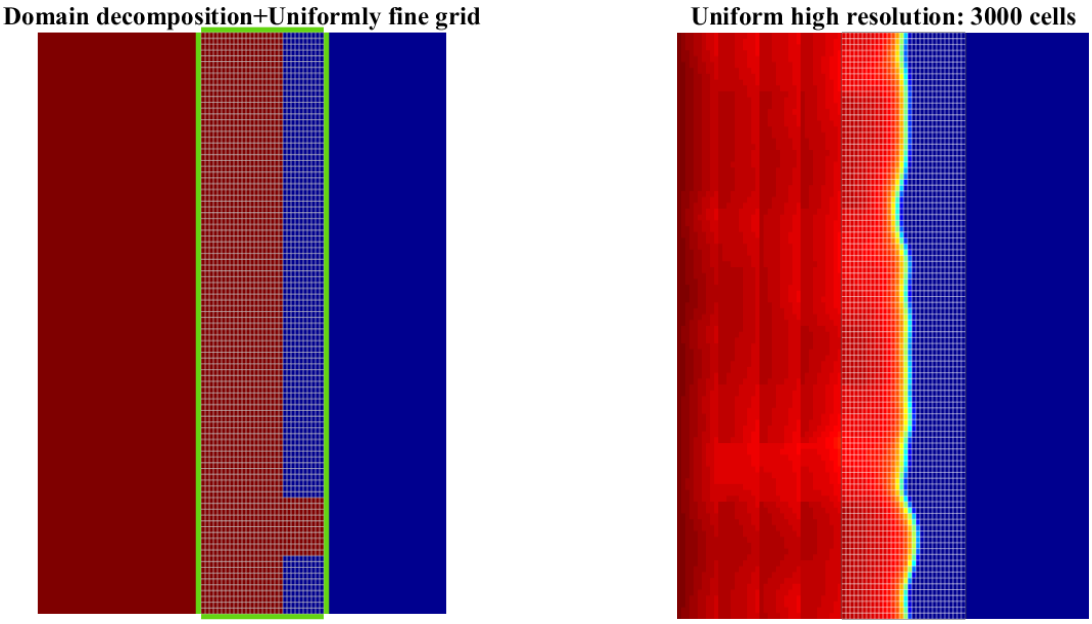

Figure 6.19: Grid generated using domain decomposition. The uniform fine grid used over the multiphase flow region is shown in the left plot. Water saturation map computed using this approach is presented in the right plot.

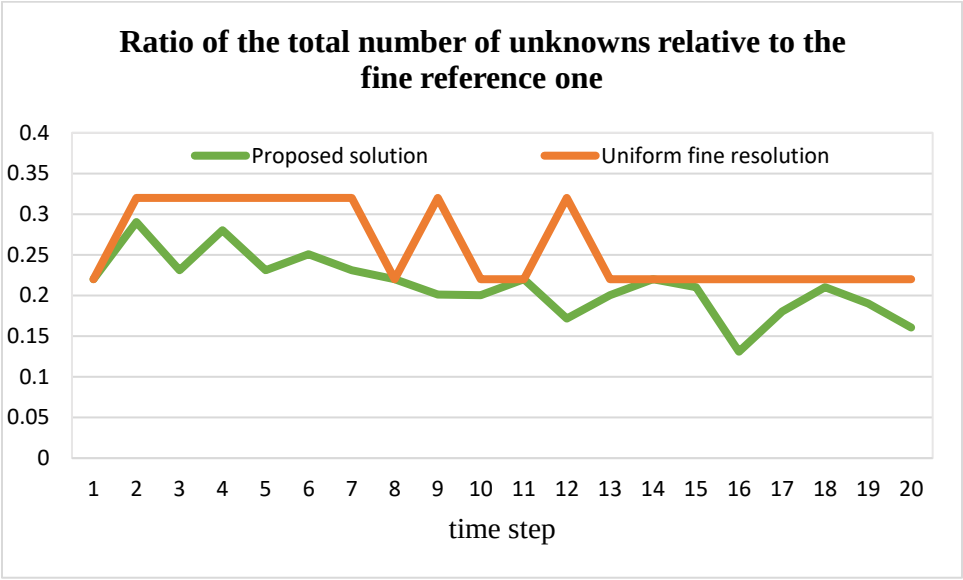

Figure 6.20: Ratio of the total number of unknowns, with and without non-uniform coarsening, to the total number of unknowns in the reference solution.

6.3.5 **Numerical example five: Intermediate resolution level**

In the previous examples, the resolution of the coarse blocks containing the front was increased to the resolution of the original fine grid in the adaptive coarsening step. However, the

spatial resolution of the indicated coarse grid blocks can be increased to any intermediate resolution. As a result, the number of global degrees of freedom could be decreased and thus the computational efficiency could be improved. In this example, we revisit the test case illustrated in numerical example 6.3.1 (page 99) and increase the resolution of coarse blocks in the frontal zone to an intermediate level, with a coarsening ratio of 2 relative to the original fine grid resolution.

Water saturation maps are shown in Figure 6.21, at the same time steps as in the test case. The water cut, the relative saturation error, and the number of global degrees of freedom for the two resolution levels of adaptive coarsening are presented in Figure 6.22, Figure 6.23, and Figure 6.24, respectively. In this example, increasing the resolution of the coarse blocks containing the front to an intermediate resolution with an agglomeration ratio of 2 gives similar results, while decreasing the total number of unknowns.

In general, the resolution level depends on the complexity of the multiphase flow problem. The intermediate resolution level will also be tested in the more heterogeneous reservoir of SPE10 benchmark model.

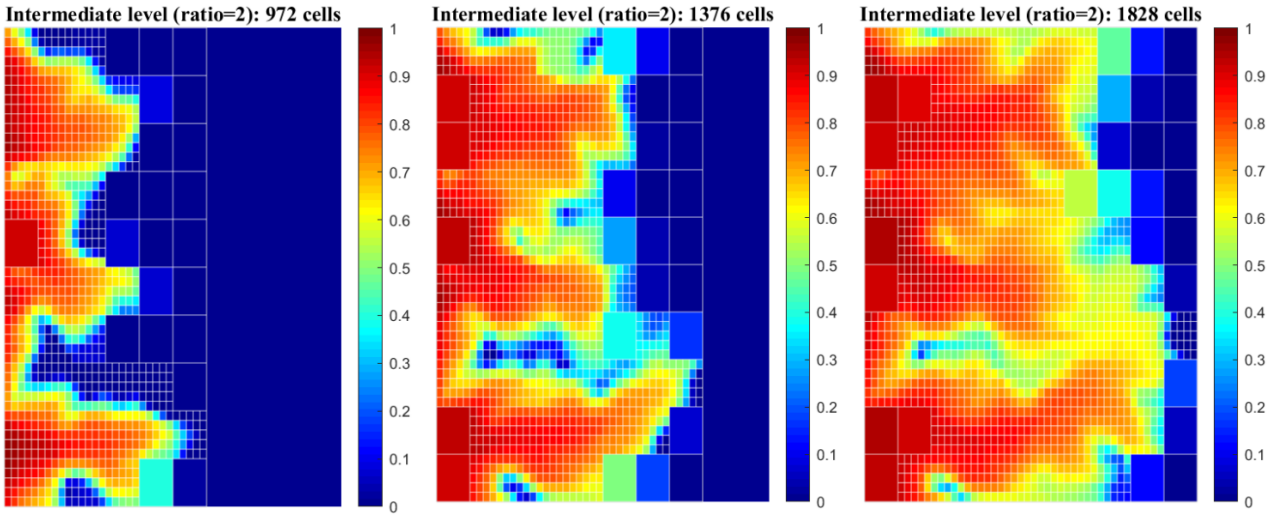

Figure 6.21: Water saturation maps computed using the adaptive solution strategy with the intermediate resolution level of coarsening ratio 2.

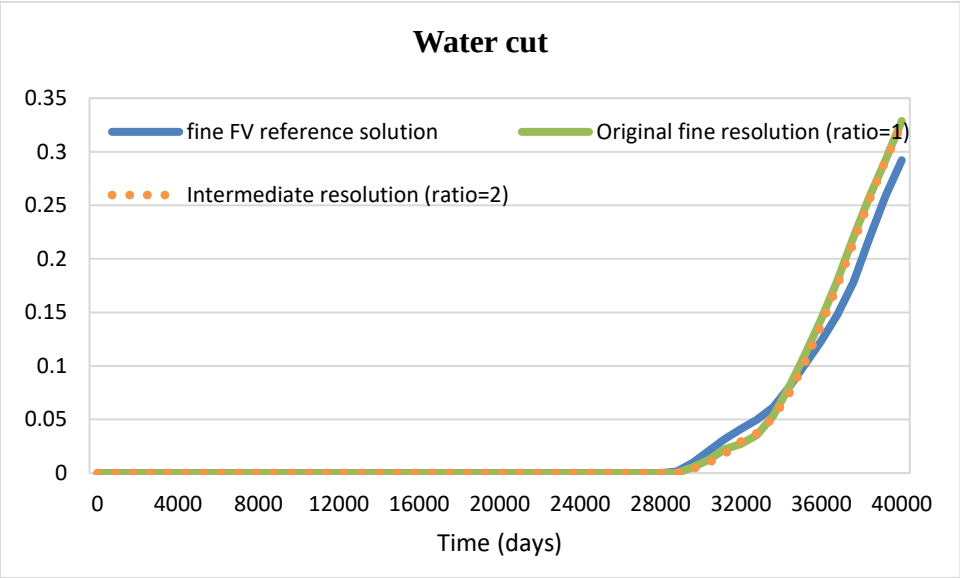

Figure 6.22: Water cut for the fine FV reference solution and the adaptive solution strategy with two resolution levels.

Figure 6.23: Relative saturation L1 error for the adaptive solution strategy with two resolution levels compared to the fine FV reference solution.

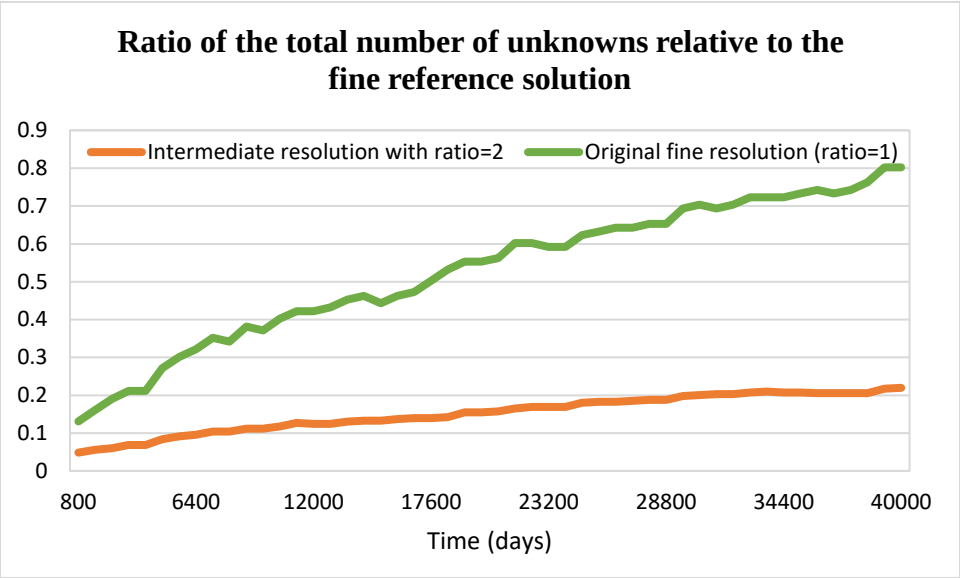

Figure 6.24: Ratio of the total number of unknowns, at each time step, for the adaptive solution strategy with two resolution levels, to the total number of unknowns in the reference solution.

6.3.6 **Numerical example six: Favourable displacement**

In this example, the proposed solution strategy is tested in a favourable displacement process, in a two-dimensional Cartesian model with permeability values taken from layer 70 of the second SPE10 benchmark test. Water and oil viscosities are set to 3.0 cp. Initial and boundary conditions remain as in the previous examples.

Figure 6.25 presents water saturation maps at three different time steps in this channelized reservoir, using the proposed solution strategy. The first two plots of each row show the results with two different resolution levels, the finest mesh resolution and an intermediate one equivalent to a grid with an agglomeration ratio of 2. The third plot displays the reference solution where flow and transport problems are solved using the FV scheme in the base fine grid. Water saturation maps computed using the DG method to solve the pressure equation and the implicit FV scheme to solve the saturation equation in the base coarse grid are presented in Figure 6.26. It can be observed from this figure that a low-resolution grid cannot capture the channelized flow details. The FFrT prediction of the flow pattern is close to the coarse-scale simulation results, by solving an explicit equation with a small computational cost. To compare the FFrT method as a non-uniform coarsening criterion, the results of the adaptive solution approach with a saturation criterion and a tolerance of 10^{-3} is shown in Figure 6.27, at the same timesteps. Using the

saturation criterion marks all grid blocks behind the front to remain in high-resolution during the coarsening step, that might affect the computational efficiency of the simulation.

Figure 6.28 compares water cut results for different solution schemes in this example. At the coarse scale, the DG flow – FV transport solution gives better results than the fully finite volume solution, both in terms of water breakthrough time and water cut. The adaptive approach with a saturation criterion and the DG pressure solver is closer to the fine reference solution compared to the proposed approach with the FFrT method. However, the use of high spatial resolutions is not optimized in this approach. At the intermediate fine resolution, the results of both approaches are similar, even though the saturation gradient criterion gives more accurate water production in the last time steps. Figure 6.29 presents the relative saturation L1 error computed for these solution approaches. The saturation criterion scheme gives the least error in this example. However, by comparing the total number of unknowns, presented in Figure 6.30, it is confirmed that the approach with the FFrT method is more computationally efficient as the number of global degrees of freedom is inferior. This figure does not take into account the real CPU time of solving the transport equation or the front advance equation, but as already stated, the FFrT method is faster than the saturation criterion approach. These last three plots also prove that an intermediate fine resolution provides a very good balance between solution accuracy and computational effort.

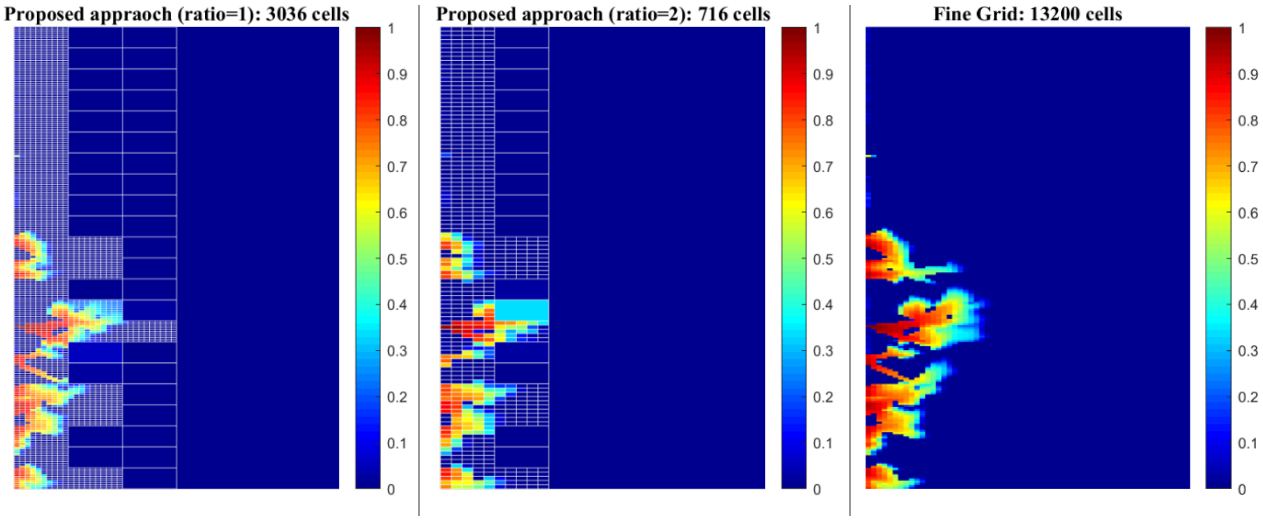

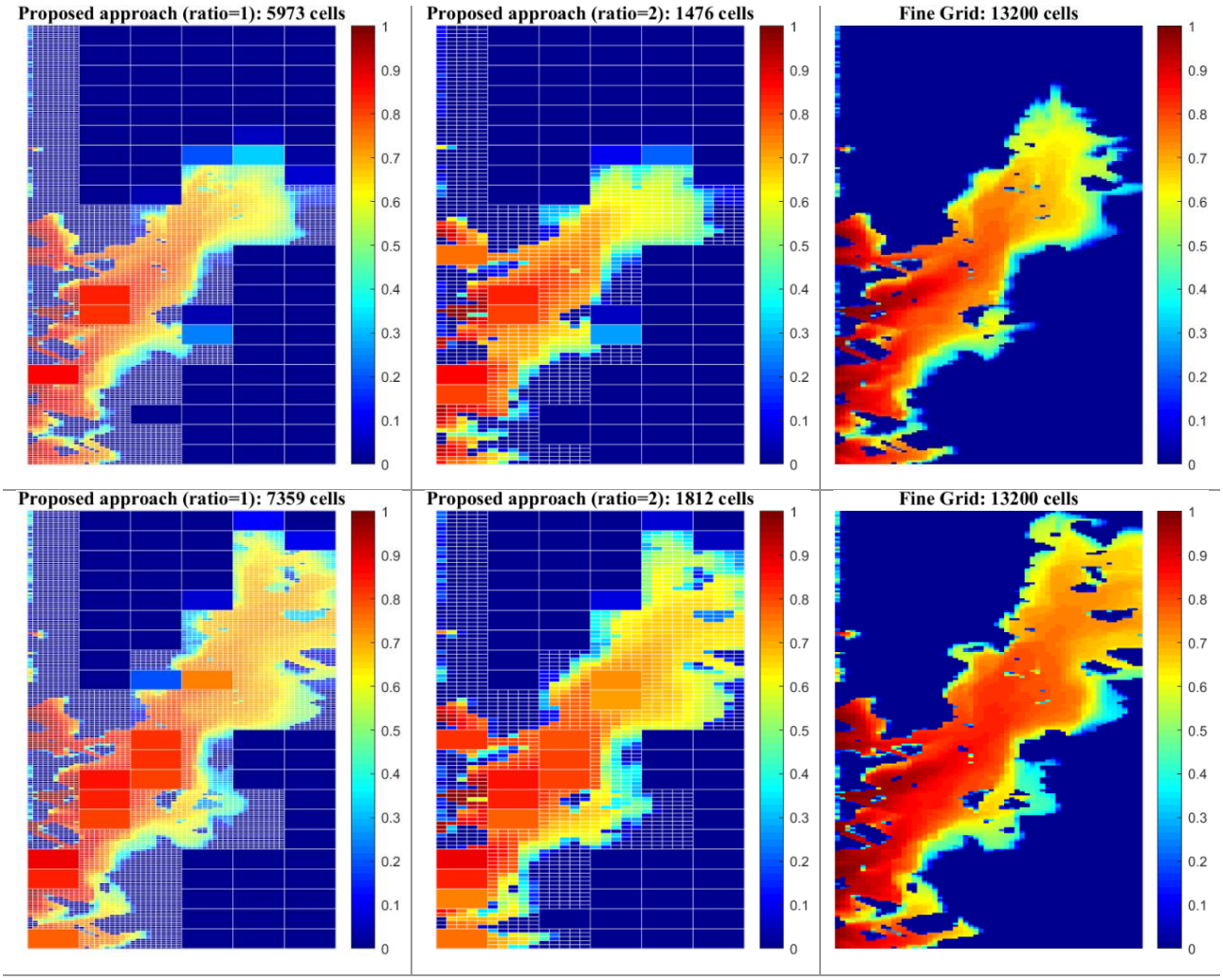

Figure 6.25: Water saturation maps, for layer 70 of the SPE10 model, computed using the proposed approach with the highest resolution and an intermediate one, and the FV on the original fine grid, before, at, and after breakthrough time.

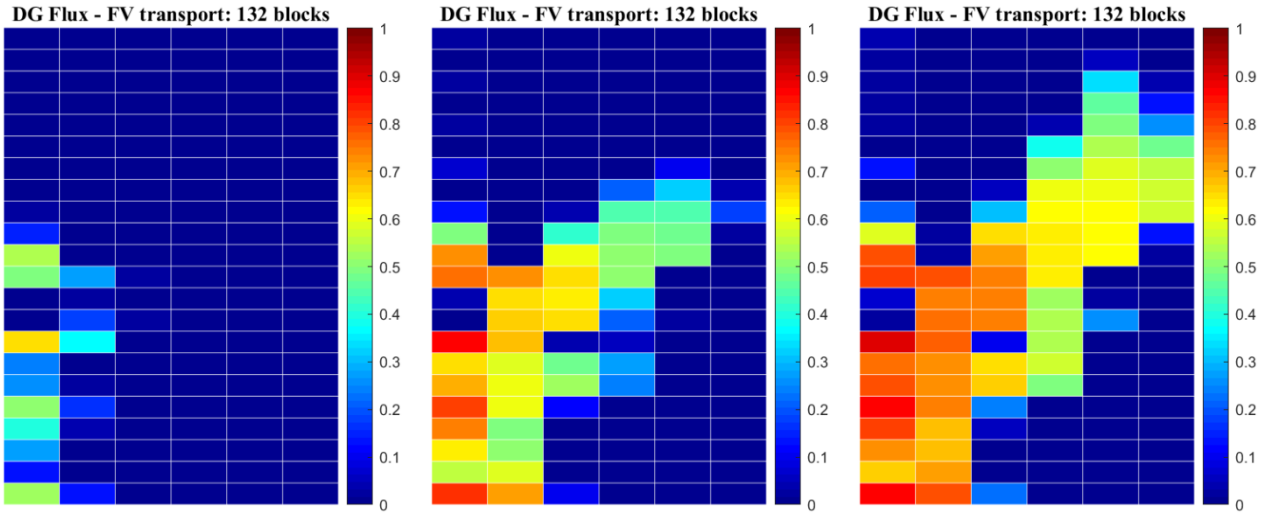

Figure 6.26: Water saturation maps, for layer 70 of the SPE10 model, computed using the DG pressure solver and the FV saturation solver in the base coarse grid, at the same time steps.

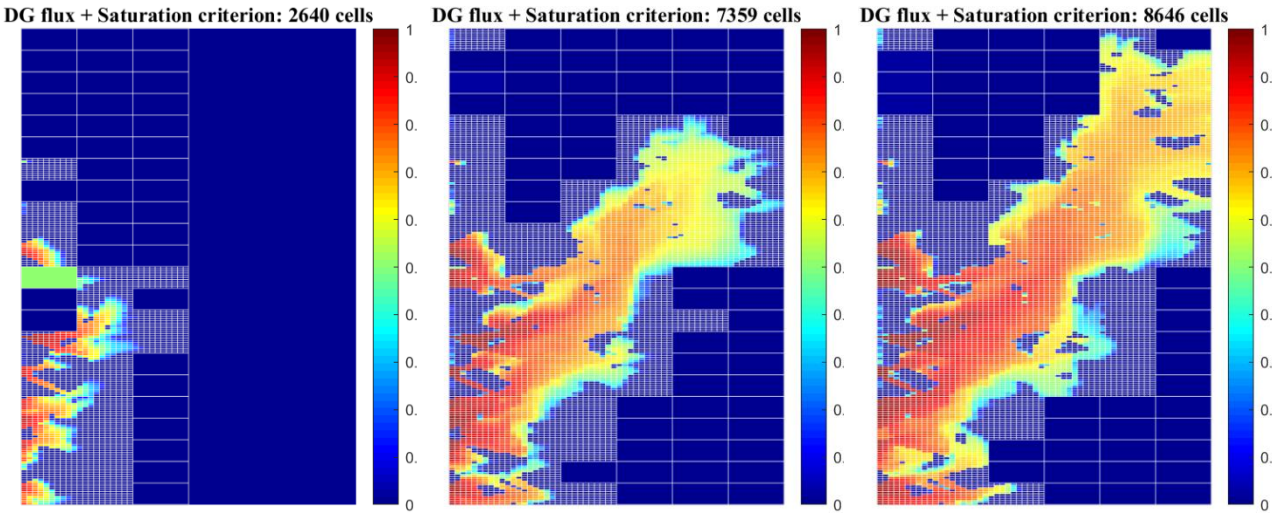

Figure 6.27: Water saturation maps, for layer 70 of the SPE10 model, computed with the adaptive approach using the saturation gradient as a coarsening criterion, at the same time steps.

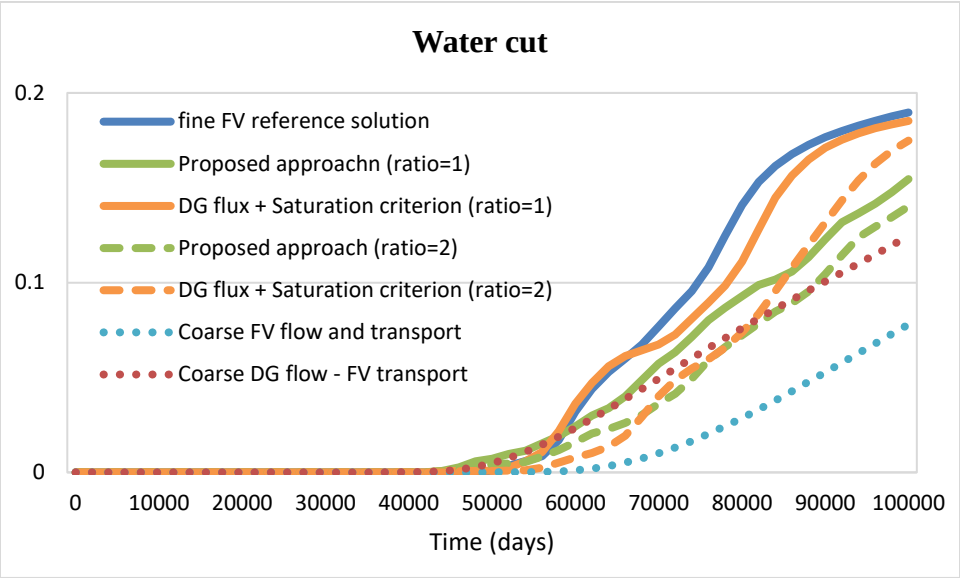

Figure 6.28: Water cut for different solution schemes for the case of a favourable displacement in layer 70 of the SPE10 model.

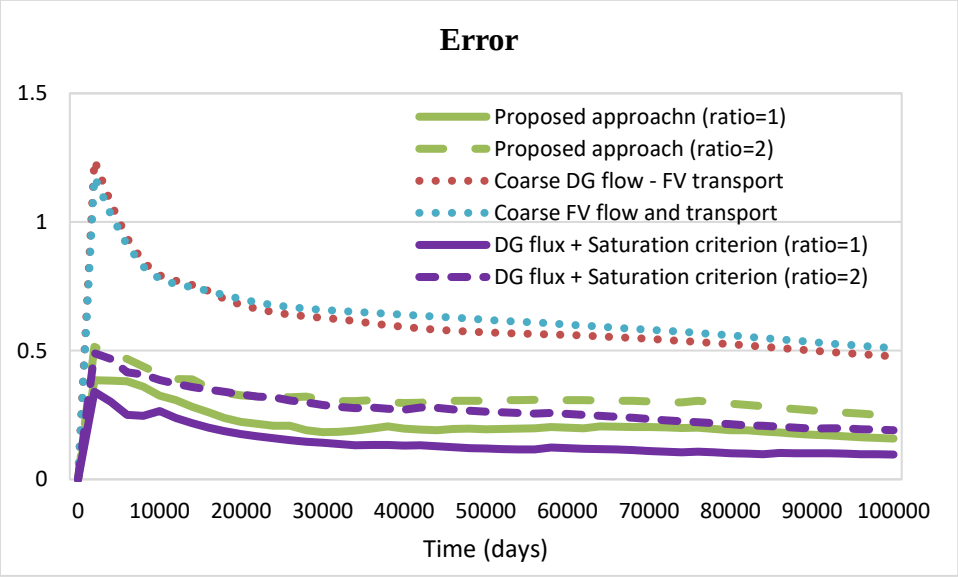

Figure 6.29: Relative saturation error for different solution schemes for the case of a favourable displacement in layer 70 of the SPE10 model.

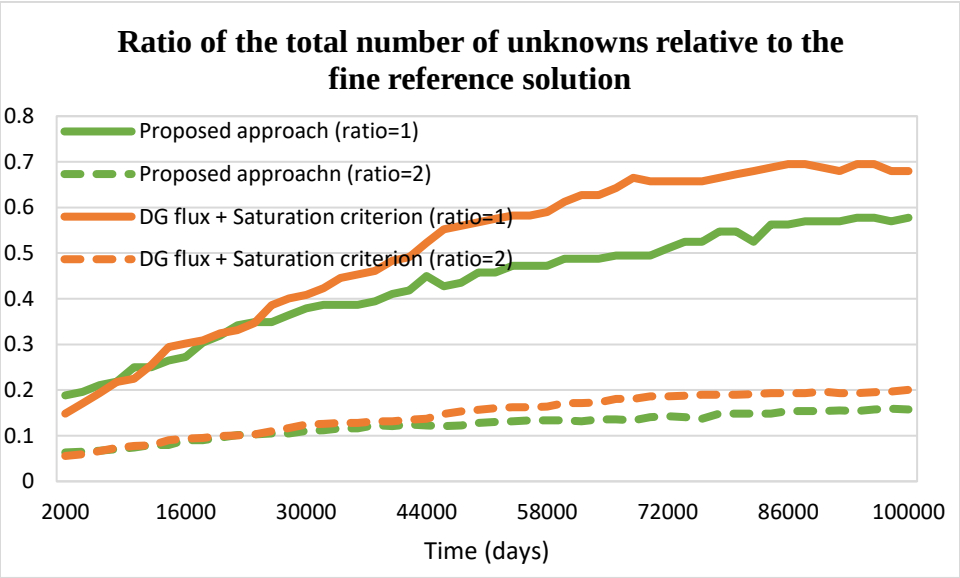

Figure 6.30: Ratio of the total number of unknowns in different solution strategies to the total number of unknowns in the base fine solution, for the case of a favourable displacement in layer 70 of the SPE10 benchmark test.

In another example with the same favourable viscosity ratio, the proposed solution scheme, along with other approaches, is tested in layer 22 of the SPE10 model.

Figure 6.31 shows water saturation maps for the proposed adaptive scheme with two coarsening criterion and the fine reference solution. In this example, the FFrT method successfully marks the frontal grid blocks to remain at a high resolution. Single-phase blocks, both in the un-swept areas ahead of the front and the swept areas behind the front, are coarsened to improve computational efficiency. The saturation criterion scheme, while producing results very similar to the base reference solution, uses a high-resolution mesh in many of the single-phase areas both ahead and behind the front.

Water cuts, relative saturation errors, and the number of global degrees of freedom, for the coarse-scale simulation and the proposed scheme with different intermediate resolution levels, are presented in Figure 6.32, Figure 6.33, and Figure 6.34, respectively. To obtain an accurate solution while minimizing the computational cost, the proposed approach with an intermediate resolution with an agglomeration ratio of 2 provides better results.

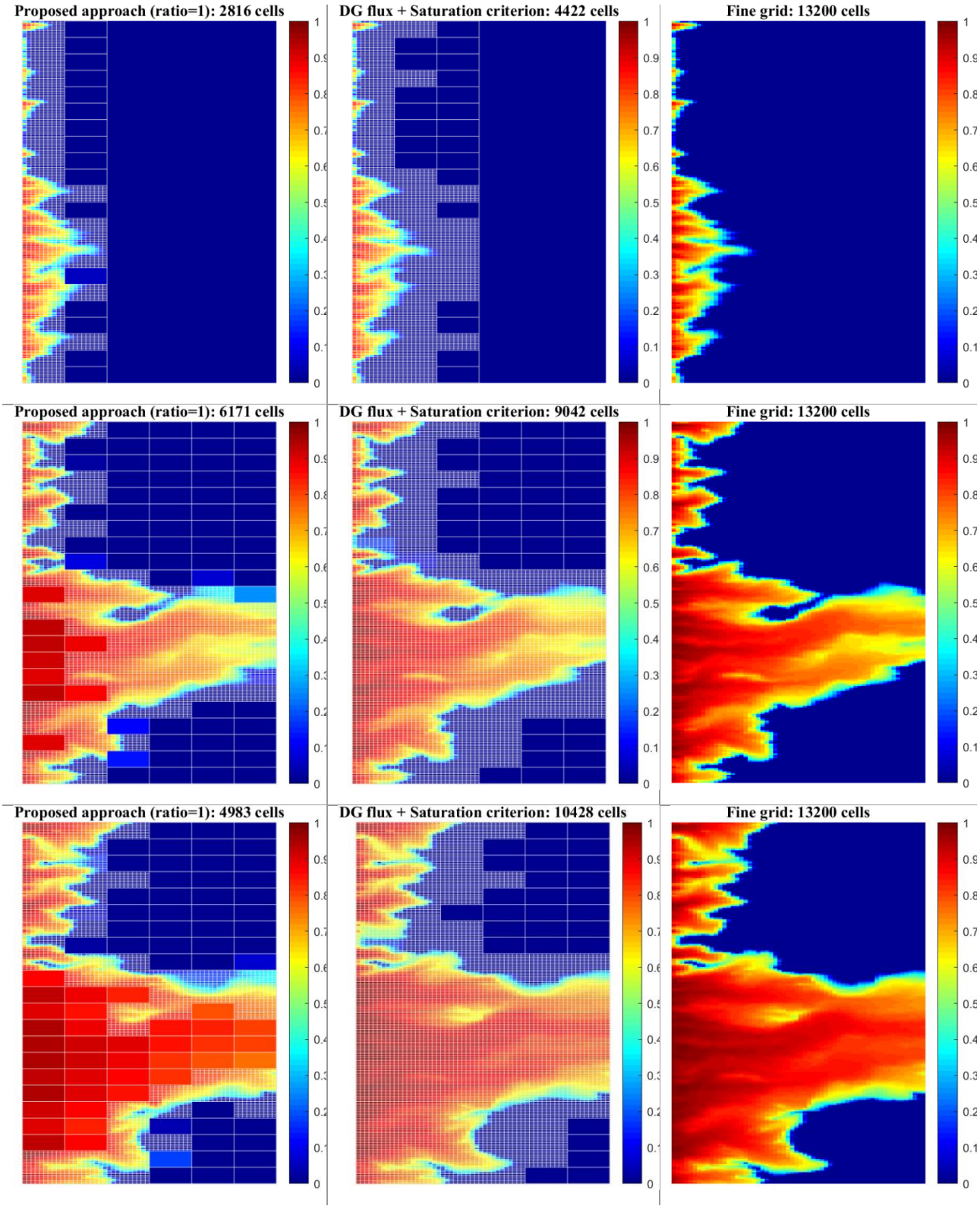

Figure 6.31: Water saturation maps for the adaptive scheme with two coarsening criteria and the fine reference solution, for a favourable displacement in layer 22 of the SPE10 test case.

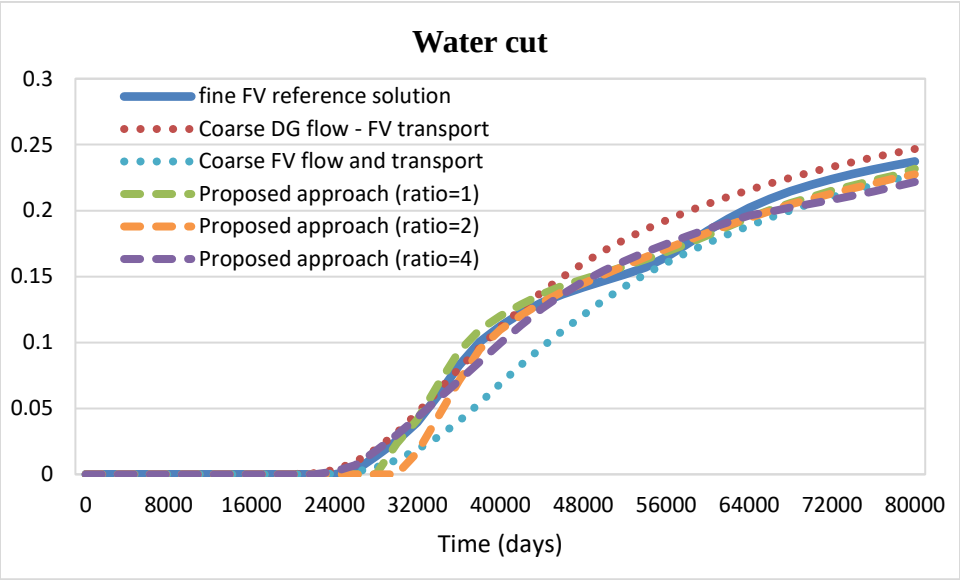

Figure 6.32: Water cut obtained for the fine-scale FV reference solution, the DG and FV coarse-scale solutions, and the adaptive proposed solution with different fine resolution levels, for the case of a favourable displacement in layer 22 of the SPE10 model.

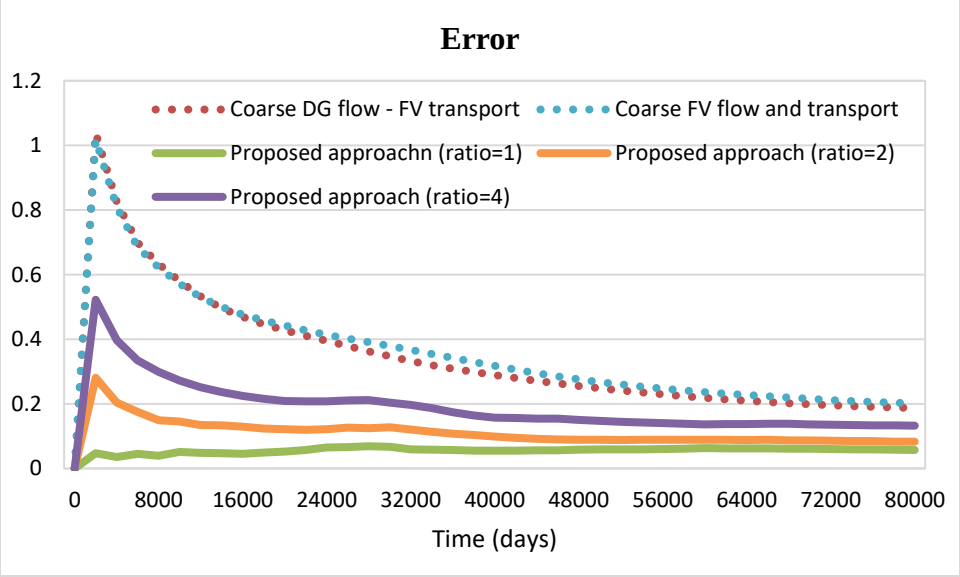

Figure 6.33: Relative error in coarse-scale solutions as well as the adaptive proposed solution with different fine resolution levels, for a favourable displacement in layer 22 of the SPE10 model.

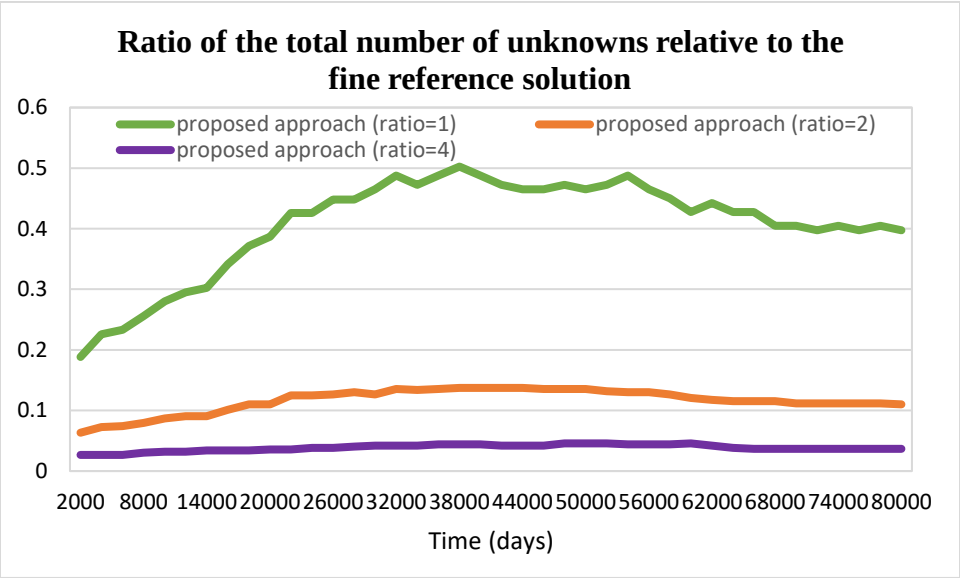

Figure 6.34: Ratio of the total number of unknowns in the proposed approach with different fine resolution levels to the total number of unknowns in the base fine solution, for the favourable displacement in layer 22 of the SPE10 benchmark test.

6.3.7 **Numerical example seven: Unfavourable displacement**

In this example, we consider the same waterflood problem in layer 70, but we decrease the viscosity of water to 0.3 *cp* to test the approach with an unfavourable viscosity ratio.

Water saturation maps for the proposed approach with the FFrT method and a classic saturation criterion and the fine reference solution are shown in Figure 6.35, at three different time steps. The scheme with the DG pressure solver and the coarsening criterion of the saturation gradient marks all the multiphase grid blocks to remain in a high resolution, however, some single-phase blocks are also marked using this criterion. This can be related to the numerical diffusion of solving the transport equation in a coarse grid. Even though this scheme gives very similar results to the ones of the fine reference solution, the non-uniform coarsening is not ideal. The proposed approach with the DG pressure solver and the FFrT method works well in terms of flow pattern and optimized non-uniform coarsening. All the marked grid blocks using the FFrT method are in the multiphase flow region. The only drawback is the prediction of the smearing front in the very low saturation areas before the breakthrough time.

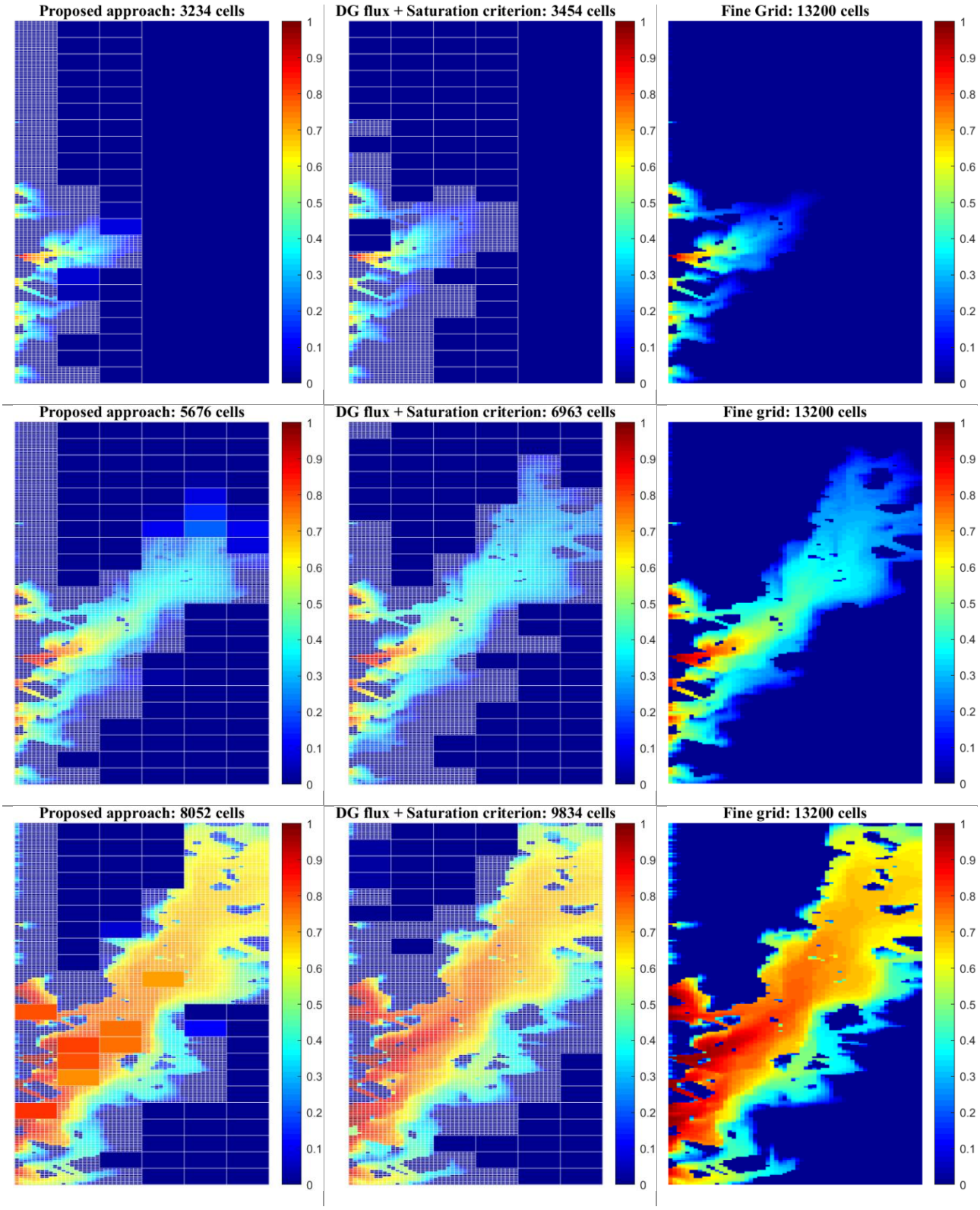

Figure 6.35: Water saturation maps for the layer 70 of the SPE10 model, at three different time steps before (first row), at (second row), and after (third row) the water breakthrough, for an unfavourable displacement case.

Figure 6.36 shows the water cut for different solution methods. The fully FV coarse-scale simulation gives errors both in the breakthrough time and the water cut, which confirms the importance of using more accurate solution methods. Figure 6.37 presents the relative L1 error in saturation for different schemes, including the intermediate resolution levels. The total number of unknowns in adaptive approaches relative to the base fine solution, presented in Figure 6.38, shows that using the saturation gradient as the criterion to use the highest resolution in multiphase regions is not computationally efficient. It is worth noting that this plot shows the number of global degrees of freedom as an indicator of computational effort. However, the computational time of solving the transport equation even in a low-resolution grid is much higher than solving an explicit equation in some parts of the same low-resolution grid. This cost has not been represented in this figure. The proposed approach with an intermediate resolution level of agglomeration ratio 2 provides an accurate solution and succeeds to decrease the number of global degrees of freedom.

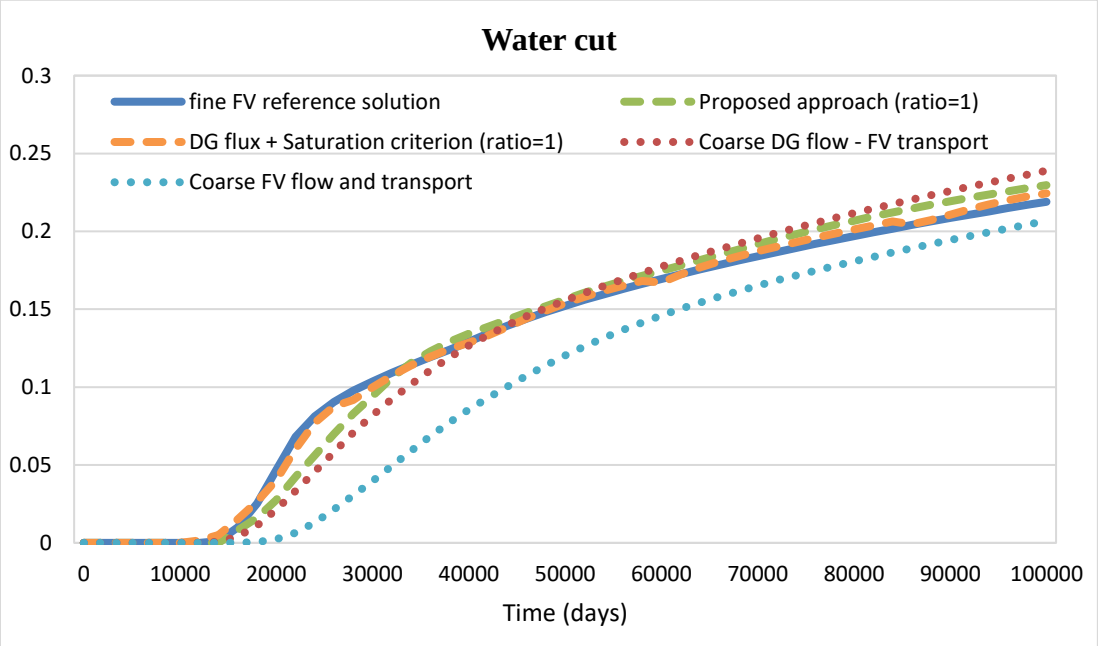

Figure 6.36: Water cut computed using the fine-scale FV simulation, the DG and FV coarse-scale solutions, and the adaptive solution approach with different coarsening criteria, for the case of an unfavourable waterflood problem in layer 70 of the SPE10 model.

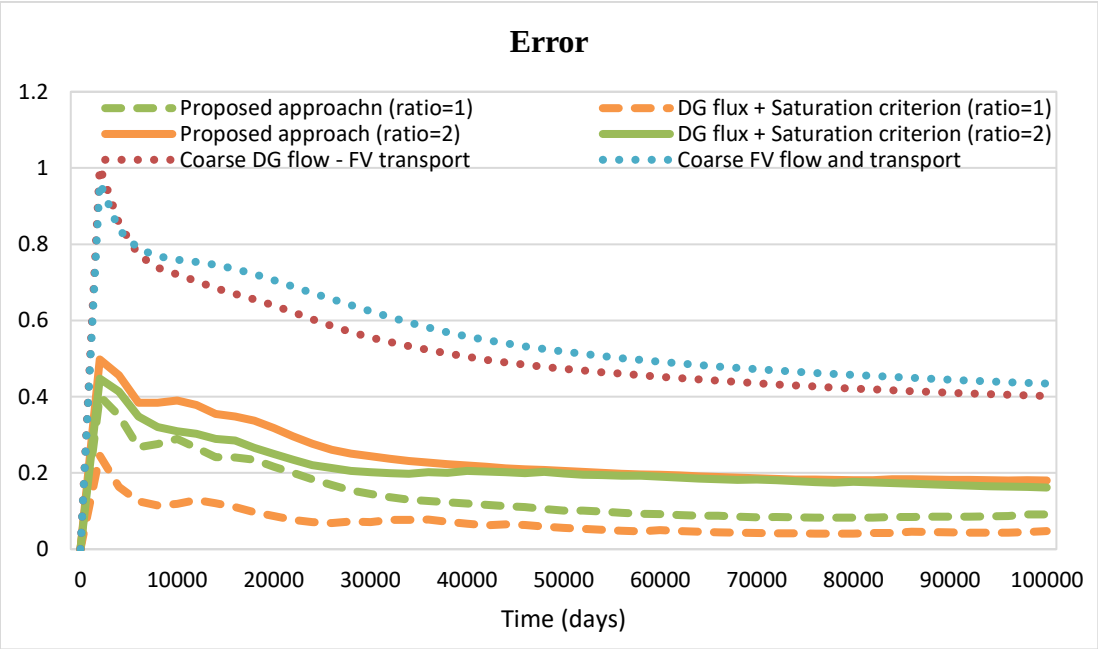

Figure 6.37: Relative error for the case of an unfavourable displacement in layer 70 of SPE10 model using different solution strategies.

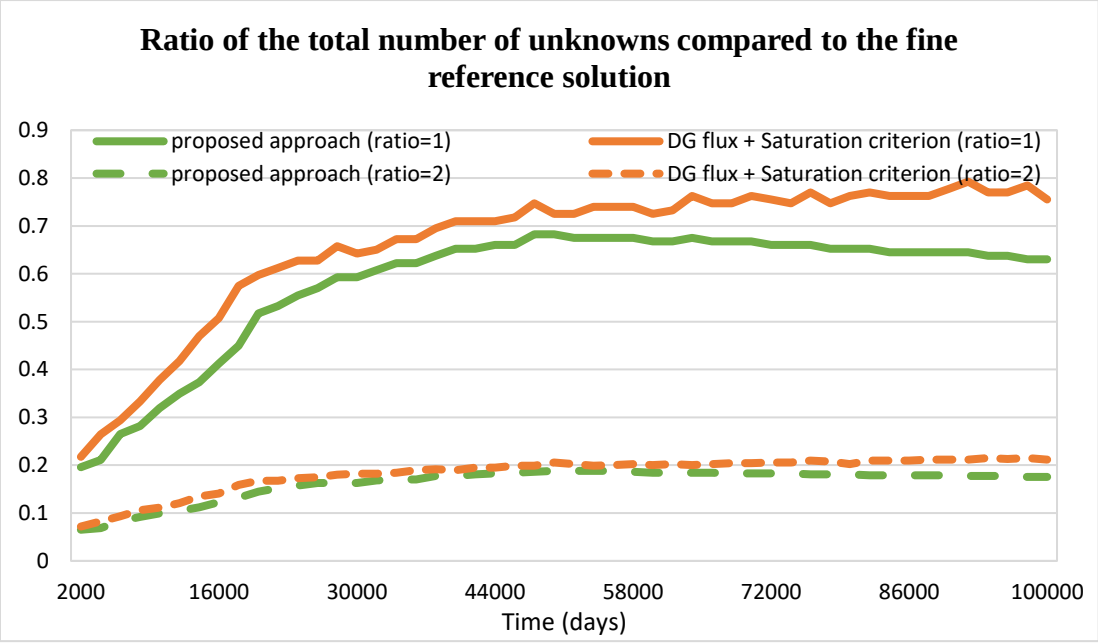

Figure 6.38: Ratio of the total number of unknowns in the adaptive approach with different coarsening criteria and different resolution levels to the total number of unknowns in the base fine solution, for an unfavourable displacement in layer 70 of the SPE10 benchmark test.

To summarize previous numerical examples with different cases of immiscible displacements, a standard coarse-scale FV solution yields erroneous results in terms of water breakthrough times, cumulative water production, and flow details. The DG discretization method with linear approximations provides better results in solving the pressure equation compared to the FV method. More accurate computation of total fluxes is proved to be important for getting a better prediction of the front position and the boundary conditions for the transport solution over the multiphase flow region. Concerning the adaptive coarsening criterion, the saturation gradient is slightly more precise than the FFrT method. However, the FFrT method is more advantageous in terms of computational costs, while still providing very effective results. We have also shown that the resolution of the multiphase flow region can be adjusted based on the complexity of the flow problem and the required order of accuracy. In the above numerical examples, an intermediate resolution level proved to be a suitable choice to achieve accurate results while decreasing the number of global degrees of freedom to a great extent.

7 Conclusion

7.1 Concluding remarks

This thesis presents the work towards the development of an efficient and accurate numerical model for solving multiphase flow problems in porous media. A sequential approach has been developed for immiscible multiphase flow simulations in heterogeneous porous media. Several numerical discretization methods and solution strategies have been investigated and incorporated into the proposed model. Numerical experiments are conducted to analyse the performance of the proposed solution strategy. To summarize the thesis work:

- An original method combining different solution strategies in different flow regions of the domain has been developed. The proposed method unifies the use of dynamic non-uniform coarsening, a discontinuous Galerkin method, and a fastly-evaluated coarsening criterion to accelerate multiphase flows simulations in heterogeneous porous media without losing accuracy.

- We have developed a fast front tracking (FFrT) method to predict the position of the front without solving nonlinearly coupled flow and transport equations over the whole domain. The FFrT method appears as being a promising approach to mix different resolution strategies according to different flow areas. This method can be used on a coarse scale to identify the multiphase flow region with satisfying accuracy and a small computational cost of solving an explicit equation in some parts of the domain. This information can be used as input to the dynamic mesh coarsening and adaptive use of DG and FV solvers for the pressure equation. The FFrT method has proved to be a powerful tool to predict the position of the front.

- Near the saturation front, in the multiphase region, where the coupling of viscous fingering and channelling is expected, we have shown that a high-resolution grid used along with a finite volume discretization leads to stable solutions with improved accuracy.

- Far from the front, in the single-phase flow regions i.e., the swept areas behind the front and the unswept areas ahead of the front, the DG method used on a lower resolution grid increases the accuracy of the total fluxes. In these parts of the domain, increasing the mesh

resolution does not yield significant improvements in the solution. The use of a DG method on a low-resolution grid, even with the linear approximation, proved to be superior to the FV scheme. The use of the DG method leads to an improved prediction in the FFrT method and more accurate total fluxes used as boundary conditions of the local multiphase flow problem.

- The computational efficiency of the solution method depends on the overall spreading of the multiphase region, and the level of resolution in the adaptive coarsening process. We have shown that the resolution level can be adjusted depending on the required order of accuracy, the available computational power, and the complexity of the problem. In the studied test cases, an intermediate resolution with an agglomeration ratio of 2 provided an acceptable balanced overall accuracy while decreasing significantly the computational effort compared to the original fine resolution.

7.2 Future work

In this section, some of the possible directions of future works are discussed.

- A more general framework:

The proposed solution strategy could be extended to a more general framework. The fast front tracking method can be adapted to handle more complex flows like radial ones around wells in 3D domains.

- A higher order of approximations in the DG scheme:

In this work, we have used linear approximations uniformly over the domain. An important advantage of DG methods is their ability to approximate the solution by discontinuous polynomials of various degrees in various elements, a feature supported in FESTUNG. Knowing the position of the front and thus the single and multiphase flow regions, one option could be to increase the order of approximating polynomials in the multiphase flow region. If the improved accuracy of the total fluxes is satisfactory, one could solve only the transport equation in the multiphase flow region in a non-uniform grid, instead of the current approach that solves both flow and transport equations in this region. The piece-wise constant fluxes can be computed on

faces of a finer resolution grid from polynomial approximated DG fluxes. This straightforward downscaling of total fluxes from a lower spatial resolution to a higher one is an important advantage over finite volume methods.

- DG pressure solver in a non-uniformly coarse grid

Throughout this work, we have solved the pressure equation in the base uniform coarse grid, using the DG method. Another option could be to solve the pressure equation using the DG scheme in a non-uniformly coarsened grid with an adaptive order of approximation. A lower polynomial order could be used in high-resolution areas, while higher orders of approximating polynomial could be implemented in coarse areas. A rigorous error analysis based on a-posteriori error estimation (Gratien et al., 2016) could be useful to guide this hp-adaptive scheme and to find the best trade-off between accuracy and efficiency.

- Using the underlying permeabilities in the DG pressure solver:

In this work, we have used the DG discretization method to improve the accuracy of total fluxes on a low-resolution grid. Another objective of using DG in our work was to test the idea of using the underlying fine permeability values instead of one upscaled permeability value per grid block when evaluating the integral terms. We have detailed the formulation and algorithm on page 64 of chapter 4, along with some preliminary results. We will continue to test this idea to increase the accuracy of DG conservative fluxes using the underlying permeability values at the coarse scale.

- Testing other approaches:

Other solution approaches could be tested. For example, working at a coarse-scale using classical single-phase upscaling, coupled with upscaled two-phase flow equations with an effective fractional flow function (Artus et al., 2004; Fayers et al., 1992; Sorbie et al., 1995) and a macrodispersion term modelling the subgrid disorder. The effective fractional flow accounts for the average local pressure saturation coupling. This could help to get fast estimation of the front location and its typical thickness at the coarse scale directly. If necessary, a mesh refinement will

then be set up in this area depending on a posteriori criterion quantifying the overall accuracy of the calculation.

8 References

Aarnes, J.E., 2004. On the use of a mixed multiscale finite element method for greater flexibility and increased speed or improved accuracy in reservoir simulation. Multiscale Modeling & Simulation 2 (3), 421–439.

Aarnes, J.E., Gimse, T., Lie, K.-A., 2007a. An Introduction to the Numerics of Flow in Porous Media using Matlab, in: Hasle, G. (Ed.), Geometric modelling, numerical simulation, and optimization: Applied mathematics at SINTEF ; with 34 tables. Springer, Berlin, pp. 265–306.

Aarnes, J.E., Hauge, V.L., Efendiev, Y., 2007b. Coarsening of three-dimensional structured and unstructured grids for subsurface flow. Advances in water resources 30 (11), 2177–2193. https://doi.org/10.1016/j.advwatres.2007.04.007.

Aarnes, J.E., Kippe, V., Lie, K.-A., 2005. Mixed multiscale finite elements and streamline methods for reservoir simulation of large geomodels. Advances in water resources 28 (3), 257–271. https://doi.org/10.1016/j.advwatres.2004.10.007.

Aarnes, J.E., Krogstad, S., Lie, K.-A., 2008. Multiscale mixed/mimetic methods on corner-point grids. Comput Geosci 12 (3), 297–315. https://doi.org/10.1007/s10596-007-9072-8.

Aavatsmark, I., 2007. Interpretation of a two-point flux stencil for skew parallelogram grids. Comput Geosci 11 (3), 199–206. https://doi.org/10.1007/s10596-007-9042-1.

Aavatsmark, I., Barkve, T., Bøe, O., Mannseth, T., 1998a. Discretization on Unstructured Grids for Inhomogeneous, Anisotropic Media. Part I: Derivation of the Methods. SIAM J. Sci. Comput. 19 (5), 1700–1716. https://doi.org/10.1137/S1064827595293582.

Aavatsmark, I., Barkve, T., Bøe, O., Mannseth, T., 1998b. Discretization on Unstructured Grids For Inhomogeneous, Anisotropic Media. Part II: Discussion And Numerical Results. SIAM J. Sci. Comput. 19 (5), 1717–1736. https://doi.org/10.1137/S1064827595293594.

Aavatsmark, I., Barkve, T., Bøe, Ø., Mannseth, T., 1996. Discretization on Non-Orthogonal, Quadrilateral Grids for Inhomogeneous, Anisotropic Media. Journal of Computational Physics 127 (1), 2–14. https://doi.org/10.1006/jcph.1996.0154.

Aavatsmark, I., Eigestad, G.T., Klausen, R.A., Wheeler, M.F., Yotov, I., 2007. Convergence of a symmetric MPFA method on quadrilateral grids. Comput Geosci 11 (4), 333–345. https://doi.org/10.1007/s10596-007-9056-8.

Al-Najem, A.A., Siddiqui, S., Soliman, M., Yuen, B. (Eds.), 2012. Streamline simulation technology: Evolution and recent trends. Society of Petroleum Engineers.

Alpak, F.O., 2015. Quasiglobal Multiphase Upscaling of Reservoir Models with Nonlocal Stratigraphic Heterogeneities. SPE Journal 20 (02), 277–293. https://doi.org/10.2118/170245-PA.

Alpak, F.O., Pal, M., Lie, K.-A., 2012. A Multiscale Adaptive Local-Global Method for Modeling Flow in Stratigraphically Complex Reservoirs. SPE Journal 17 (04), 1056–1070. https://doi.org/10.2118/140403-PA.

Amanbek, Y., Singh, G., Wheeler, M.F., van Duijn, H., 2017. Adaptive numerical homogenization for upscaling single phase flow and transport. ICES Report 12, 17.

Amaziane, B., 1993. Global behavior of compressible three-phase flow in heterogeneous porous media. Transp Porous Med 10 (1), 43–56. https://doi.org/10.1007/BF00617510.

Antonietti, P.F., Formaggia, L., Scotti, A., Verani, M., Verzott, N., 2016. Mimetic finite difference approximation of flows in fractured porous media. ESAIM: M2AN 50 (3), 809–832. https://doi.org/10.1051/m2an/2015087.

Arnold, D.N., 1982. An Interior Penalty Finite Element Method with Discontinuous Elements. SIAM J. Numer. Anal. 19 (4), 742–760. https://doi.org/10.1137/0719052.

Arnold, D.N., Brezzi, F., Cockburn, B., Marini, L.D., 2002. Unified Analysis of Discontinuous Galerkin Methods for Elliptic Problems. SIAM J. Numer. Anal. 39 (5), 1749–1779. https://doi.org/10.1137/S0036142901384162.

Artus, V., Nœtinger, B., Ricard, L., 2004. Dynamics of the water–oil front for two-phase, immiscible flow in heterogeneous porous media. 1–stratified media. Transport in porous media 56 (3), 283–303.

Ates, H., Bahar, A., Salem, S.E.-A., Charfeddine, M., Kelkar, M.G., 2005. Ranking and Upscaling of Geostatistical Reservoir Models Using Streamline Simulation: A Field Case Study. SPE Reservoir Evaluation & Engineering 8 (01), 22–32. https://doi.org/10.2118/81497-PA.

Audigane, P., Blunt, M.J., 2004. Dual Mesh Method for Upscaling in Waterflood Simulation. Transport in porous media 55 (1), 71–89. https://doi.org/10.1023/B:TIPM.0000007309.48913.d2.

Babuska, I., 1973. The Finite Element Method with Penalty. Mathematics of Computation 27 (122), 221. https://doi.org/10.2307/2005611.

Babuška, I., Zlámal, M., 1973. Nonconforming Elements in the Finite Element Method with Penalty. SIAM J. Numer. Anal. 10 (5), 863–875. https://doi.org/10.1137/0710071.

Barker, J.W., Dupouy, P., 1999. An analysis of dynamic pseudo-relative permeability methods for oil-water flows. Petroleum Geoscience 5 (4), 385–394.

Barker, J.W., Fayers, F.J., 1994. Transport Coefficients for Compositional Simulation With Coarse Grids in Heterogeneous Media. SPE Advanced Technology Series 2 (02), 103–112. https://doi.org/10.2118/22591-PA.

Barker, J.W., Thibeau, S., 1997. A critical review of the use of pseudorelative permeabilities for upscaling. SPE reservoir engineering 12 (2), 138–143.

Bassi, F., Rebay, S., 1997. A High-Order Accurate Discontinuous Finite Element Method for the Numerical Solution of the Compressible Navier–Stokes Equations. Journal of Computational Physics 131 (2), 267–279. https://doi.org/10.1006/jcph.1996.5572.

Bastian, P., Riviere, B., 2004. Discontinuous Galerkin methods for two-phase flow in porous media. University of Heidelberg Technical Report 28, 2004.

Batycky, R.P., Blunt, M.J., Thiele, M.R., 1997. A 3D field-scale streamline-based reservoir simulator. SPE reservoir engineering 12 (04), 246–254.

Batycky, R.P., Thiele, M.R., Baker, R.O., Chugh, S., 2008. Revisiting Reservoir Flood-Surveillance Methods Using Streamlines. SPE Reservoir Evaluation & Engineering 11 (02), 387–394. https://doi.org/10.2118/95402-PA.

Begg, S.H., Carter, R.R., Dranfield, P., 1989. Assigning effective values to simulator gridblock parameters for heterogeneous reservoirs. SPE reservoir engineering 4 (04), 455–463.

Bell, J.B., Trangenstein, J.A., Shubin, G.R., 1986. Conservation Laws of Mixed Type Describing Three-Phase Flow in Porous Media. SIAM J. Appl. Math. 46 (6), 1000–1017. https://doi.org/10.1137/0146059.

Berger, M.J., Oliger, J., 1984. Adaptive mesh refinement for hyperbolic partial differential equations. Journal of Computational Physics 53 (3), 484–512. https://doi.org/10.1016/0021-9991(84)90073-1.

Berkowitz, B., Balberg, I., 1993. Percolation theory and its application to groundwater hydrology. Water Resour. Res. 29 (4), 775–794. https://doi.org/10.1029/92WR02707.

Berre, I., Dahle, H.K., Karlsen, K.H., Nordhaug, H.F., 2002. A streamline front tracking method for two-and three-phase flow including capillary forces. Contemporary Mathematics 295, 49–62.

Berre, I., Karlsen, K.H., Lie, K.-A., Natvig, J.R., 2005. Fast computation of arrival times in heterogeneous media. Computational Geosciences 9 (4), 179–201.

Bouquet, S., Douarche, F., Roggero, F., Leray, S., 2020. Characterization of Viscous Fingering and Channeling for the Assessment of Polymer-Based Heavy Oil Displacements. Transp Porous Med 131 (3), 873–906. https://doi.org/10.1007/s11242-019-01370-3.

Bourgeat, A., 1997. Two-Phase Flow, in: Hornung, U. (Ed.), Homogenization and Porous Media. Springer New York, New York, NY, pp. 95–127.

Bratvedt, F., Bratvedt, K., Buchholz, C.F., Holden, L., Holden, H., Risebro, N.H., 1992. A New Front-Tracking Method for Reservoir Simulation. SPE reservoir engineering 7 (01), 107–116. https://doi.org/10.2118/19805-PA.

Bressan, A., 1992. Global solutions of systems of conservation laws by wave-front tracking. Journal of mathematical analysis and applications 170 (2), 414–432. https://doi.org/10.1016/0022-247x(92)90027-b.

Brezzi, F., LIPNIKOV, K., Shashkov, M., 2005a. Convergence of the Mimetic Finite Difference Method for Diffusion Problems on Polyhedral Meshes. SIAM J. Numer. Anal. 43 (5), 1872–1896. https://doi.org/10.1137/040613950.

Brezzi, F., LIPNIKOV, K., SIMONCINI, V., 2005b. A FAMILY OF MIMETIC FINITE DIFFERENCE METHODS ON POLYGONAL AND POLYHEDRAL MESHES. Math. Models Methods Appl. Sci. 15 (10), 1533–1551. https://doi.org/10.1142/S0218202505000832.

Brooks, R., Corey, T., 1964. Hydraulic Properties of Porous Media and Their Relation to Drainage Design. Transactions of the ASAE 7 (1), 26–28. https://doi.org/10.13031/2013.40684.

Cao, H., Aziz, K., 2002. Performance of IMPSAT and IMPSAT-AIM Models in Compositional Simulation, in: SPE Annual Technical Conference and Exhibition: Proceedings : 28 September-2 October, 2002, San Antonio, Texas, U.S.A. SPE Annual Technical Conference and Exhibition. Society of Petroleum Engineers, Dallas, Tex.

Cappanera, L., Riviere, B., 2019. Discontinuous Galerkin method for solving the black-oil problem in porous media. Numer. Methods Partial Differential Eq. 35 (2), 761–789. https://doi.org/10.1002/num.22324.

Chen, Y., Durlofsky, L.J., 2006. Adaptive Local–Global Upscaling for General Flow Scenarios in Heterogeneous Formations. Transp Porous Med 62 (2), 157–185. https://doi.org/10.1007/s11242-005-0619-7.

Chen, Y., Durlofsky, L.J., Gerritsen, M., Wen, X.H., 2003. A coupled local–global upscaling approach for simulating flow in highly heterogeneous formations. Advances in water resources 26 (10), 1041–1060. https://doi.org/10.1016/s0309-1708(03)00101-5.

Christensen, J.R., Darche, G., Dechelette, B., Ma, H., Sammon, P.H., 2004. Applications Of Dynamic Gridding To Thermal Simulations, in: . SPE International Thermal Operations and Heavy Oil Symposium and Western Regional Meeting. Society of Petroleum Engineers.

Christie, M.A., 1996. Upscaling for reservoir simulation. Journal of Petroleum Technology 48 (11), 1,004-1,010.

Christie, M.A., Blunt, M.J., 2001. Tenth SPE Comparative Solution Project: A comparison of upscaling techniques, in: . SPE Reservoir Simulation Symposium. Society of Petroleum Engineers.

Coats, K.H., 2000. A Note on IMPES and Some IMPES-Based Simulation Models. SPE J. 5 (03), 245–251. https://doi.org/10.2118/65092-PA.

Cockburn, B., Shu, C.-W., 1998. The Local Discontinuous Galerkin Method for Time-Dependent Convection-Diffusion Systems. SIAM J. Numer. Anal. 35 (6), 2440–2463. https://doi.org/10.1137/S0036142997316712.

Courant, R., Friedrichs, K., Lewy, H., 1928. ber die partiellen Differenzengleichungen der mathematischen Physik. Math. Ann. 100 (1), 32–74. https://doi.org/10.1007/BF01448839.

Dagan, G., 1989. Flow and Transport in Porous Formations Springer {Verlag. Springer-Verlag, Berlin and New York.

Dagan, G., 1993. Higher-order correction of effective permeability of heterogeneous isotropic formations of lognormal conductivity distribution. Transp Porous Med 12 (3), 279–290. https://doi.org/10.1007/BF00624462.

Dagan, G., Fiori, A., Jankovic, I., 2013. Upscaling of flow in heterogeneous porous formations: Critical examination and issues of principle. Advances in water resources 51, 67–85. https://doi.org/10.1016/j.advwatres.2011.12.017.

Darcy, H.P., 1856. Exposition et application des principes à suivre et des formules à employer dans les questions de distribution d'eau. Les fontaines publiques de la ville de Dijon, Eds. Victor Dalmont, Paris 1856.

Daripa, P., Glimm, J., Lindquist, B., Maesumi, M., McBryan, O., 1987. On the simulation of heterogeneous petroleum reservoirs. New York Univ., NY (USA). Courant Mathematics and Computing Lab. https://www.osti.gov/biblio/6568167.

Darman, N.H., Pickup, G.E., Sorbie, K.S., 2002. A comparison of two-phase dynamic upscaling methods based on fluid potentials. Computational Geosciences 6 (1), 5–27.

Datta-Gupta, A., King, M.J., 2007. Streamline simulation: Theory and practice. Society of Petroleum Engineers Richardson.

Deutsch, C., 1989. Calculating effective absolute permeability in sandstone/shale sequences. SPE Formation Evaluation 4 (03), 343–348.

De-Wit, A., Homsy, G.M., 1997a. Viscous fingering in periodically heterogeneous porous media. I. Formulation and linear instability. The Journal of Chemical Physics 107 (22), 9609–9618. https://doi.org/10.1063/1.475258.

De-Wit, A., Homsy, G.M., 1997b. Viscous fingering in periodically heterogeneous porous media. II. Numerical simulations. The Journal of Chemical Physics 107 (22), 9619–9628. https://doi.org/10.1063/1.475259.

Di Pietro, D.A., Ern, A., 2011. Mathematical aspects of discontinuous Galerkin methods. Springer Science & Business Media.

Di Pietro, D.A., Vohralík, M., 2014. A Review of Recent Advances in Discretization Methods, a Posteriori Error Analysis, and Adaptive Algorithms for Numerical Modeling in

Geosciences. Oil & Gas Science and Technology - Rev. IFP Energies nouvelles 69 (4), 701–729. https://doi.org/10.2516/ogst/2013158.

Droniou, J., 2014. Finite volume schemes for diffusion equations: Introduction to and review of modern methods. Math. Models Methods Appl. Sci. 24 (08), 1575–1619. https://doi.org/10.1142/S0218202514400041.

Droniou, J., Eymard, R., 2006. A mixed finite volume scheme for anisotropic diffusion problems on any grid. Numer. Math. 105 (1), 35–71. https://doi.org/10.1007/s00211-006-0034-1.

Droniou, J., Eymard, R., GALLOUET, T., HERBIN, R., 2010. A unified approach to mimetic finite difference, hybrid finite volume and mixed finite volume methods. Math. Models Methods Appl. Sci. 20 (02), 265–295. https://doi.org/10.1142/S0218202510004222.

Durlofsky, L.J., 1991. Numerical calculation of equivalent grid block permeability tensors for heterogeneous porous media. Water Resources Research 27 (5), 699–708.

Durlofsky, L.J. (Ed.), 2003. Upscaling of geocellular models for reservoir flow simulation: A review of recent progress. Citeseer, 23-27.

Durlofsky, L.J. (Ed.), 2005. Upscaling and gridding of fine scale geological models for flow simulation.

Durlofsky, L.J., Jones, R.C., Milliken, W.J., 1997. A nonuniform coarsening approach for the scale-up of displacement processes in heterogeneous porous media. Advances in water resources 20 (5-6), 335–347.

Edwards, M.G., Rogers, C.F., 1998. Finite volume discretization with imposed flux continuity for the general tensor pressure equation. Computational Geosciences 2 (4), 259–290. https://doi.org/10.1023/A:1011510505406.

EPGeology, 2014. Scales in Subsurface Modeling. The different data scales used in subsurface modeling. Petroleum Geology. http://www.epgeology.com/gallery/image.php?album_id=10&image_id=188.

Ern, A., Stephansen, A.F., Zunino, P., 2008. A discontinuous Galerkin method with weighted averages for advection-diffusion equations with locally small and anisotropic diffusivity. IMA Journal of Numerical Analysis 29 (2), 235–256. https://doi.org/10.1093/imanum/drm050.

Eymard, R., Gallouet, T., Herbin, R., 2010. Discretization of heterogeneous and anisotropic diffusion problems on general nonconforming meshes SUSHI: a scheme using stabilization and hybrid interfaces. IMA J Numer Anal 30 (4), 1009–1043. https://doi.org/10.1093/imanum/drn084.

Eymard, R., GALLOUËT, T., HERBIN, R., 2000. Finite volume methods, in: Ciarlet, P.G., Lions, J.L. (Eds.), Handbook of numerical analysis. North-Holland, Amsterdam, London, pp. 713–1018.

Fabien, M.S., Knepley, M.G., Rivière, B.M., 2018. A hybridizable discontinuous Galerkin method for two-phase flow in heterogeneous porous media. Int J Numer Methods Eng 116 (3), 161–177. https://doi.org/10.1002/nme.5919.

Fagin, R.G., Stewart, C.H., 1966. A New Approach to the Two-Dimensional Multiphase Reservoir Simulator. Society of Petroleum Engineers Journal 6 (02), 175–182. https://doi.org/10.2118/1188-PA.

Faille, I., 1992. A control volume method to solve an elliptic equation on a two-dimensional irregular mesh. Computer methods in applied mechanics and engineering 100 (2), 275–290. https://doi.org/10.1016/0045-7825(92)90186-N.

Farmer, C.L., 2002. Upscaling: A review. International Journal for Numerical Methods in Fluids 40 (1-2), 63–78.

Fayers, F.J., Blunt, M.J., Christie, M.A., 1992. Comparisons of empirical viscous-fngering models and their calibration for heterogeneous problems. SPE reservoir engineering 7 (02), 195–203. https://doi.org/10.2118/22184-PA.

Floris, F.J.T., Bush, M.D., Cuypers, M., Roggero, F., Syversveen, A.-R., 2001. Methods for quantifying the uncertainty of production forecasts: a comparative study. Petroleum Geoscience 7 (S), S87-S96. https://doi.org/10.1144/petgeo.7.S.S87.

Frank, F., Reuter, B., Aizinger, V., Knabner, P., 2015. FESTUNG: A MATLAB/GNU Octave toolbox for the discontinuous Galerkin method, Part I: Diffusion operator. Computers & Mathematics with Applications 70 (1), 11–46.

Ganjeh-Ghazvini, M., 2019. The impact of viscosity contrast on the error of heterogeneity loss in upscaling of geological models. Journal of Petroleum Science and Engineering 173, 681–689. https://doi.org/10.1016/j.petrol.2018.10.061.

Gelhar, L.W., Axness, C.L., 1983. Three-dimensional stochastic analysis of macrodispersion in aquifers. Water Resour. Res. 19 (1), 161–180. https://doi.org/10.1029/WR019i001p00161.

Gerritsen, M., Lambers, J.V., 2008. Integration of local–global upscaling and grid adaptivity for simulation of subsurface flow in heterogeneous formations. Computational Geosciences 12 (2), 193–208. https://doi.org/10.1007/s10596-007-9078-2.

Glimm, J., Grove, J.W., Li, X.L., Shyue, K., Zeng, Y., Zhang, Q., 1998. Three-dimensional front tracking. SIAM Journal on Scientific Computing 19 (3), 703–727.

Glimm, J., Isaacson, E., Marchesin, D., McBryan, O., 1980. A shock tracking method for hyperbolic systems, in: . the 1980 Army Numerical Analysis and Computers Conference, NASA Res. Center, Moffett Field, Calif., p. 1.

Glimm, J., Isaacson, E., Marchesin, D., McBryan, O., 1981. Front tracking for hyperbolic systems. Advances in Applied Mathematics 2 (1), 91–119. https://doi.org/10.1016/0196-8858(81)90040-3.

Glimm, J., Lindquist, B., McBryan, O.A., Plohr, B., Yaniv, S. (Eds.), 1983. Front tracking for petroleum reservoir simulation. Society of Petroleum Engineers.

Gómez-Hernández, J.J., Journel, A.G. (Eds.), 1990. Stochastic Characterization of Grid-Block Permeabilities: from Point Values to Block Tensors: from point values to block tensors. European Association of Geoscientists & Engineers, 1 p.

Gorell, S., Bassett, R., 2001. Trends in Reservoir Simulation: Big Models, Scalable Models? Will you Please Make up Your Mind?, in: . SPE Annual Technical Conference and Exhibition. OnePetro.

Gratien, J.-M., Ricois, O., Yousef, S., 2016. Reservoir Simulator Runtime Enhancement Based on a Posteriori Error Estimation Techniques. Oil & Gas Science and Technology - Rev. IFP Energies nouvelles 71 (5), 59. https://doi.org/10.2516/ogst/2016009.

Guadagnini, A., Riva, M., Neuman, S.P., 2018. Recent advances in scalable non-Gaussian geostatistics: The generalized sub-Gaussian model. Journal of Hydrology 562, 685–691. https://doi.org/10.1016/j.jhydrol.2018.05.001.

Guerillot, D., Rudkiewicz, J.L., Ravenne, C., Renard, G., Galli, A., 1990. An Integrated Model for Computer Aided Reservoir Description : from Outcrop Study to Fluid Flow Simulations. Rev. Inst. Fr. Pét. 45 (1), 71–77. https://doi.org/10.2516/ogst:1990005.

Guion, A.N., Skaflestad, B., Lie, K.-A., Wu, X.-H., 2019. Validation of a Non-Uniform Coarsening and Upscaling Framework, in: . SPE Reservoir Simulation Conference. Society of Petroleum Engineers.

Hajibeygi, H., Tchelepi, H.A., 2014. Compositional Multiscale Finite-Volume Formulation. SPE Journal 19 (02), 316–326. https://doi.org/10.2118/163664-PA.

Han, D.K., Han, D.L., Yan, C.Z., Peng, L.T., 1987. A more flexible approach of dynamic local grid refinement for reservoir modeling, in: SPE Symposium on Reservoir Simulation. Society of Petroleum Engineers.

Hauge, V.L., Lie, K.-A., Natvig, J.R. (Eds.), 2010. Flow-based grid coarsening for transport simulations.

Hauge, V.L., Lie, K.-A., Natvig, J.R., 2012. Flow-based coarsening for multiscale simulation of transport in porous media. Computational Geosciences 16 (2), 391–408.

Heinemann, Z.E., Gerken, G., Hantelmann, G. von, 1983. Using Local Grid Refinement in a Multiple-Application Reservoir Simulator, in: SPE Reservoir Simulation Symposium. Society of Petroleum Engineers.

Hewett, T.A., Behrens, R.A., 1991. Scaling laws in reservoir simulation and their use in a hybrid finite difference/streamtube approach to simulation the effects of permeability heterogeneity. Academic Press Inc., London.

Holden, H., Risebro, N.H., 2015. Front tracking for hyperbolic conservation laws. Springer.

Holden, L., Nielsen, B.F., 2000. Global Upscaling of Permeability in Heterogeneous Reservoirs; The Output Least Squares (OLS) Method. Transport in porous media 40 (2), 115–143. https://doi.org/10.1023/A:1006657515753.

Hornung, U. (Ed.), 1997. Homogenization and Porous Media. Springer New York, New York, NY.

Hoteit, H., Chawathé, A., 2016. Making Field-Scale Chemical Enhanced-Oil-Recovery Simulations a Practical Reality With Dynamic Gridding. SPE Journal 21 (06), 2220–2237. https://doi.org/10.2118/169688-PA.

Hou, T.Y., Wu, X.-H., 1997a. A multiscale finite element method for elliptic problems in composite materials and porous media. Journal of Computational Physics 134 (1), 169–189.

Hou, T.Y., Wu, X.-H., 1997b. A Multiscale Finite Element Method for Elliptic Problems in Composite Materials and Porous Media. Journal of Computational Physics 134 (1), 169–189. https://doi.org/10.1006/jcph.1997.5682.

Hunt, A.G., Ewing, R.P., Ghanbarian, B., 2014. Percolation theory for flow in porous media, 3rd ed. Springer, Berlin.

Idrobo, E.A., Choudhary, M.K., Datta-Gupta, A., 2000. Swept Volume Calculations and Ranking of Geostatistical Reservoir Models Using Streamline Simulation, in: . SPE/AAPG Western Regional Meeting. Society of Petroleum Engineers.

IEA, 2020. CCUS in Clean Energy Transitions. https://www.iea.org/reports/ccus-in-clean-energy-transitions.

Indelman, P., Abramovich, B., 1994. A higher-order approximation to effective conductivity in media of anisotropic random structure. Water Resour. Res. 30 (6), 1857–1864. https://doi.org/10.1029/94WR00077.

Izgec, O., Sayarpour, M., Shook, G.M., 2011. Maximizing volumetric sweep efficiency in waterfloods with hydrocarbon F–Φ curves. Journal of Petroleum Science and Engineering 78 (1), 54–64. https://doi.org/10.1016/j.petrol.2011.05.003.

Jaekel, U., Vereecken, H., 1997. Renormalization group analysis of macrodispersion in a directed random flow. Water Resour. Res. 33 (10), 2287–2299. https://doi.org/10.1029/97WR00553.

Jamei, M., Ghafouri, H., 2016. An efficient discontinuous Galerkin method for two-phase flow modeling by conservative velocity projection. Int Jnl of Num Meth for HFF 26 (1), 63–84. https://doi.org/10.1108/HFF-08-2014-0247.

Jaust, A., Reuter, B., Aizinger, V., Schütz, J., Knabner, P., 2018. FESTUNG: A MATLAB/GNU Octave toolbox for the discontinuous Galerkin method. Part III: Hybridized discontinuous Galerkin (HDG) formulation. Computers & Mathematics with Applications 75 (12), 4505–4533.

Jenny, P., Lee, S.H., Tchelepi, H.A., 2003. Multi-scale finite-volume method for elliptic problems in subsurface flow simulation. Journal of Computational Physics 187 (1), 47–67.

Jenny, P., Lee, S.H., Tchelepi, H.A., 2005. Adaptive multiscale finite-volume method for multiphase flow and transport in porous media. Multiscale Modeling & Simulation 3 (1), 50–64.

Karimi-Fard, M., Durlofsky, L.J., 2016. A general gridding, discretization, and coarsening methodology for modeling flow in porous formations with discrete geological features. Advances in water resources 96, 354–372. https://doi.org/10.1016/j.advwatres.2016.07.019.

Karlsen, K.H., Lie, K.-A., Risebro, N.H., 2000. A fast marching method for reservoir simulation. Computational Geosciences 4 (2), 185–206. https://doi.org/10.1023/A:1011564017218.

King, M.J., Burn, K.S., Wang, P., Muralidharan, V., Alvarado, F.E., Ma, X., Datta-Gupta, A., 2006. Optimal Coarsening of 3D Reservoir Models for Flow Simulation. SPE Reservoir Evaluation & Engineering 9 (04), 317–334. https://doi.org/10.2118/95759-PA.

King, M.J., Dunayevski, V.A. (Eds.), 1989. Why waterflood works: A linearized stability analysis. Society of Petroleum Engineers.

King, M.J., King, P.R., McGill, C.A., Williams, J.K., 1995. Effective properties for flow calculations. Transport in porous media 20 (1-2), 169–196. https://doi.org/10.1007/BF00616929.

King, M.J., Mansfield, M. (Eds.), 1997. Flow Simulation of Geologic Models.

King, P.R., 1987. The use of field theoretic methods for the study of flow in a heterogeneous porous medium. J. Phys. A: Math. Gen. 20 (12), 3935–3947. https://doi.org/10.1088/0305-4470/20/12/038.

Kippe, V., Aarnes, J.E., Lie, K.A., 2008. A comparison of multiscale methods for elliptic problems in porous media flow. Computational Geosciences 12 (3), 377–398. https://doi.org/10.1007/s10596-007-9074-6.

Kyte, J.R., Berry, D.W., 1975. New pseudo functions to control numerical dispersion. Society of Petroleum Engineers Journal 15 (04), 269–276.

Langlo, P., Espedal, M.S., 1994. Macrodispersion for two-phase, immiscible flow in porous media. Advances in water resources 17 (5), 297–316. https://doi.org/10.1016/0309-1708(94)90033-7.

Langseth, J.O., 1996. On an implementation of a front tracking method for hyperbolic conservation laws. Advances in Engineering Software 26 (1), 45–63. https://doi.org/10.1016/0965-9978(95)00089-5.

Le Ravalec, M., Noetinger, B., Hu, L.Y., 2000. The FFT moving average (FFT-MA) generator: An efficient numerical method for generating and conditioning Gaussian simulations. Mathematical Geology 32 (6), 701–723.

Lee, S., Wheeler, M.F., 2018. Enriched Galerkin methods for two-phase flow in porous media with capillary pressure. Journal of Computational Physics 367, 65–86. https://doi.org/10.1016/j.jcp.2018.03.031.

Lee, S.H., Wolfsteiner, C., Tchelepi, H.A., 2008. Multiscale finite-volume formulation for multiphase flow in porous media: black oil formulation of compressible, three-phase flow with gravity. Comput Geosci 12 (3), 351–366. https://doi.org/10.1007/s10596-007-9069-3.

Lie, K.-A., 2019. An introduction to reservoir simulation using MATLAB/GNU Octave: User guide for the MATLAB reservoir simulation toolbox (MRST). Cambridge University Press, Cambridge, United Kingdom, New York, NY, USA, 1 Online-Ressource.

Lie, K.-A., Juanes, R., 2005. A front-tracking method for the simulation of three-phase flow in porous media. Computational Geosciences 9 (1), 29–59.

Lie, K.-A., Kedia, K., Skaflestad, B., Wang, X., Yang, Y., Wu, X.-H., Hoda, N., 2017a. A General Non-Uniform Coarsening and Upscaling Framework for Reduced-Order Modeling, in: . SPE Reservoir Simulation Conference. Society of Petroleum Engineers.

Lie, K.-A., Krogstad, S., Ligaarden, I.S., Natvig, J.R., Nilsen, H.M., Skaflestad, B., 2012. Open-source MATLAB implementation of consistent discretisations on complex grids. Comput Geosci 16 (2), 297–322. https://doi.org/10.1007/s10596-011-9244-4.

Lie, K.-A., Møyner, O., Natvig, J.R., 2017b. Use of Multiple Multiscale Operators To Accelerate Simulation of Complex Geomodels. SPE Journal 22 (06), 1 929-1 945. https://doi.org/10.2118/182701-PA.

Lie, K.-A., Møyner, O., Natvig, J.R., Kozlova, A., Bratvedt, K., Watanabe, S., Li, Z., 2017c. Successful application of multiscale methods in a real reservoir simulator environment. Computational Geosciences 21 (5-6), 981–998.

Lie, K.-A., Natvig, J.R., Krogstad, S., Yang, Y., Wu, X.-H., 2014. Grid adaptation for the Dirichlet–Neumann representation method and the multiscale mixed finite-element method. Comput Geosci 18 (3-4), 357–372. https://doi.org/10.1007/s10596-013-9397-4.

Lokhorst, A., Wildenborg, T., 2005. Introduction on CO 2 Geological Storage - Classification of Storage Options. Oil & gas science and technology 60 (3), 513–515. https://doi.org/10.2516/ogst:2005033.

Manzocchi, T., Carter, J.N., Skorstad, A., Fjellvoll, B., Stephen, K.D., Howell, J.A., Matthews, J.D., Walsh, J.J., Nepveu, M., Bos, C., Cole, J., Egberts, P., Flint, S., Hern, C., Holden, L., Hovland, H., Jackson, H., Kolbjørnsen, O., MacDonald, A., Nell, P.A.R., Onyeagoro, K., Strand, J., Syversveen, A.R., Tchistiakov, A., Yang, C., Yielding, G., Zimmerman, R.W., 2008. Sensitivity of the impact of geological uncertainty on production from faulted and unfaulted shallow-marine oil reservoirs: objectives and methods. Petroleum Geoscience 14 (1), 3–15. https://doi.org/10.1144/1354-079307-790.

Marcondes, F., Maliska, C.R., Zambaldi, M.C., 2009. A comparative study of implicit and explicit methods using unstructured voronoi meshes in petroleum reservoir simulation. J. Braz. Soc. Mech. Sci. & Eng. 31 (4). https://doi.org/10.1590/s1678-58782009000400010.

Marle, C.-M., 1981. Multiphase flow in porous media. Éditions technip.

Matek, B., 2016. Annual US & global geothermal power production report. Geothermal Energy Association.

Møyner, O., Krogstad, S., Lie, K.-A., 2015. The Application of Flow Diagnostics for Reservoir Management. SPE Journal 20 (02), 306–323. https://doi.org/10.2118/171557-PA.

Muggeridge, A.H., 1991. Generation of effective relative permeabilities from detailed simulation of flow in heterogeneous porous media, in: Lake, L.W., Carroll, H.B., Wesson, T.C. (Eds.), Reservoir characterization II. Academic Press, San Diego, pp. 197–225.

Muskat, M., Wyckoff, R.D., 1937. Flow of homogeneous fluids through porous media.

Natvig, J.R., Lie, K.A., Krogstad, S., Yang, Y., Wu, X.H., 2012. Grid adaption for upscaling and multiscale methods, in: Proceedings of ECMOR XIII–13th European Conference on the Mathematics of Oil Recovery. September 13.

Natvig, J.R., Skaflestad, B., Bratvedt, F., Bratvedt, K., Lie, K.-A.-A., Laptev, V., Khataniar, S.K., 2011. Multiscale Mimetic Solvers for Efficient Streamline Simulation of Fractured Reservoirs. SPE J. 16 (04), 880–888. https://doi.org/10.2118/119132-PA.

Nielsen, B.F., Tveito, A., 1998. An upscaling method for one-phase flow in heterogeneous reservoirs. A weighted output least squares (WOLS) approach. Computational Geosciences 2 (2), 93–123. https://doi.org/10.1023/A:1011541917701.

Nitsche, J., 1971. Über ein Variationsprinzip zur Lösung von Dirichlet-Problemen bei Verwendung von Teilräumen, die keinen Randbedingungen unterworfen sind. Abh.Math.Semin.Univ.Hambg. 36 (1), 9–15. https://doi.org/10.1007/bf02995904.

Noetinger, B., 1994. The effective permeability of a heterogeneous porous medium. Transp Porous Med 15 (2), 99–127. https://doi.org/10.1007/BF00625512.

Noetinger, B., Artus, V., Ricard, L., 2004. Dynamics of the water–oil front for two-phase, immiscible flow in heterogeneous porous media. 2 – isotropic media. Transport in porous media 56 (3), 305–328. https://doi.org/10.1023/B:TIPM.0000026086.75908.ca.

Nœtinger, B., Artus, V., Zargar, G., 2005. The future of stochastic and upscaling methods in hydrogeology. Hydrogeology Journal 13 (1), 184–201.

Nœtinger, B., Gautier, Y., 1998. Use of the Fourier-Laplace transform and of diagrammatical methods to interpret pumping tests in heterogeneous reservoirs. Advances in water resources 21 (7), 581–590. https://doi.org/10.1016/S0309-1708(97)00014-6.

Osher, S., Sethian, J.A., 1988. Fronts propagating with curvature-dependent speed: Algorithms based on Hamilton-Jacobi formulations. Journal of Computational Physics 79 (1), 12–49.

Paksoy, H.Ö., 2007. Thermal energy storage for sustainable energy consumption: Fundamentals, case studies and design / edited by Halime Ö Paksoy. Springer, Dordrecht.

Peaceman, D.W., 1997. Effective Transmissibilities of a Gridblock by Upscaling - Comparison of Direct Methods with Renormalization. SPE Journal 2 (03), 338–349. https://doi.org/10.2118/36722-PA.

Percell, P., Wheeler, M.F., 1978. A Local Residual Finite Element Procedure for Elliptic Equations. SIAM J. Numer. Anal. 15 (4), 705–714. https://doi.org/10.1137/0715047.

Quandalle, P., 1983. The use of flexible gridding for improved reservoir modeling, in: . SPE Reservoir Simulation Symposium. Society of Petroleum Engineers.

Rame, M., Killough, J.E., 1991. A new approach to the simulation of flows in highly heterogeneous porous media. paper SPE 21247, 17–20.

Reed, W.H., Hill, T.R., 1973. Triangular mesh methods for the neutron transport equation. Los Alamos Scientific Lab., N. Mex.(USA). https://www.osti.gov/servlets/purl/4491151.

Renard, P., Marsily, G. de, 1997. Calculating equivalent permeability: A review. Advances in water resources 20 (5-6), 253–278.

Reuter, B., Aizinger, V., Wieland, M., Frank, F., Knabner, P., 2016. FESTUNG: A MATLAB/GNU Octave toolbox for the discontinuous Galerkin method, Part II: Advection operator and slope limiting. Computers & Mathematics with Applications 72 (7), 1896–1925.

Reuter, B., Hajduk, H., Rupp, A., Frank, F., Aizinger, V., Knabner, P., 2020. FESTUNG 1.0: Overview, usage, and example applications of the MATLAB/GNU Octave toolbox for discontinuous Galerkin methods. Computers & Mathematics with Applications. https://doi.org/10.1016/j.camwa.2020.08.018.

Reuter, B., Rupp, A., Aizinger, V., Frank, F., Knabner, P., 2018. FESTUNG: A MATLAB/GNU Octave toolbox for the discontinuous Galerkin method. Part IV: Generic problem framework and model-coupling interface. arXiv preprint arXiv:1806.03908.

Risebro, N.H., 1993. A front-tracking alternative to the random choice method. Proc. Amer. Math. Soc. 117 (4), 1125. https://doi.org/10.1090/s0002-9939-1993-1120511-x.

Riviere, B., Wheeler, M.F., 2002. Discontinuous Galerkin methods for flow and transport problems in porous media. Commun. Numer. Meth. Engng. 18 (1), 63–68. https://doi.org/10.1002/cnm.464.

Riviere, B., Wheeler, M.F., Banaś, K., 2000. Part II. Discontinuous Galerkin method applied to a single phase flow in porous media. Computational Geosciences 4 (4), 337–349.

Saez, A.E., Otero, C.J., Rusinek, I., 1989. The effective homogeneous behavior of heterogeneous porous media. Transport in porous media 4 (3), 213–238. https://doi.org/10.1007/BF00138037.

Saffman, P.G., Taylor, G.I., 1958. The penetration of a fluid into a porous medium or Hele-Shaw cell containing a more viscous liquid. Proc. R. Soc. Lond. A 245 (1242), 312–329.

Sammon, P.H., 2003. Dynamic Grid Refinement and Amalgamation for Compositional Simulation, in: . SPE Reservoir Simulation Symposium. Society of Petroleum Engineers.

Sethian, J.A., 1996a. A fast marching level set method for monotonically advancing fronts. Proceedings of the National Academy of Sciences 93 (4), 1591–1595.

Sethian, J.A., 1996b. Theory, algorithms, and applications of level set methods for propagating interfaces. Acta numerica 5, 309–395.

Sethian, J.A., 1999. Level set methods and fast marching methods: Evolving interfaces in computational geometry, fluid mechanics, computer vision, and materials science / J.A. Sethian, 2nd ed. Cambridge University Press, New York.

Shahvali, M., Mallison, B., Wei, K., Gross, H., 2012. An Alternative to Streamlines for Flow Diagnostics on Structured and Unstructured Grids. SPE Journal 17 (03), 768–778. https://doi.org/10.2118/146446-PA.

Shook, G.M., Mitchell, K.M., 2009. A Robust Measure of Heterogeneity for Ranking Earth Models: The F PHI Curve and Dynamic Lorenz Coefficient, in: ATCE 2009: SPE Annual Technical Conference and Exhibition : proceedings, 4-7 October, New Orleans, Louisiana, USA. SPE Annual Technical Conference and Exhibition. Society of Petroleum Engineers, Richardson, Tex.

Sorbie, K.S., Zhang, H.R., Tsibuklis, N.B., 1995. Linear viscous fingering: New experimental results, direct simulation and the evaluation of averaged models. Chemical Engineering Science 50 (4), 601–616. https://doi.org/10.1016/0009-2509(94)00252-M.

Spesivtsev, P., Teodorovich, E.V., 2007. The statistical characteristics of the displacement front in a randomly heterogeneous medium. Journal of Applied Mathematics and Mechanics 71 (3), 424–431. https://doi.org/10.1016/j.jappmathmech.2007.07.006.

Spillette, A.G., Hillestad, J.G., Stone, H.L., 1973. A High-Stability Sequential Solution Approach to Reservoir Simulation, in: . Fall Meeting of the Society of Petroleum Engineers of AIME. OnePetro.

Stone, H.L., 1991. Rigorous Black Oil Pseudo Functions, in: SPE Symposium on Reservoir Simulation. Society of Petroleum Engineers.

Stone, H.L., Garder, A.O., 1961. Analysis of Gas-Cap or Dissolved-Gas Drive Reservoirs. Society of Petroleum Engineers Journal 1 (02), 92–104. https://doi.org/10.2118/1518-G.

Sussman, M., Smereka, P., Osher, S., 1994. A Level Set Approach for Computing Solutions to Incompressible Two-Phase Flow. Journal of Computational Physics 114 (1), 146–159. https://doi.org/10.1006/jcph.1994.1155.

Thiele, M.R., Batycky, R.P., 2003. Water Injection Optimization Using a Streamline-Based Workflow, in: SPE Annual Technical Conference and Exhibition: Proceedings : Mile-high meeting of the minds : 5-8 October, 2003, Denver, Colorado, U.S.A. SPE Annual Technical Conference and Exhibition. Society of Petroleum Engineers, Richardson, Tex.

Thomas, G.W., Thurnau, D.H., 1982. The Mathematical Basis of the Adaptive Implicit Method, in: . SPE Reservoir Simulation Symposium. Society of Petroleum Engineers.

van Batenburg, D.W., Bosch, M., Boerrigter, P.M., Zwart, A.H. de, Vink, J.C., 2011. Application of Dynamic Gridding Techniques to IOR/EOR-Processes, in: SPE Reservoir Simulation Symposium. SPE Reservoir Simulation Symposium, The Woodlands, Texas, USA. 21-23 February. Society of Petroleum Engineers, Richardson, Texas.

Verdière, S., Guérillot, D., Thomas, J.M. (Eds.), 1996. Dual mesh method for multiphase flows in heterogeneous porous media.

Von-Rosenberg, D.U., 1982. Local Mesh Refinement for Finite Difference Methods, in: . SPE Annual Technical Conference and Exhibition. Society of Petroleum Engineers.

Warren, J.E., Price, H.S., 1961. Flow in Heterogeneous Porous Media. Society of Petroleum Engineers Journal 1 (03), 153–169. https://doi.org/10.2118/1579-G.

Welge, H.J., 1952. A Simplified Method for Computing Oil Recovery by Gas or Water Drive. Journal of Petroleum Technology 4 (04), 91–98. https://doi.org/10.2118/124-G.

Wheeler, M.F., 1978. An Elliptic Collocation-Finite Element Method with Interior Penalties. SIAM J. Numer. Anal. 15 (1), 152–161. https://doi.org/10.1137/0715010.

White, C.D., Horne, R.N. (Eds.), 1987. Computing Absolute Transmissibility in the Presence of Fine-Scale Heterogeneity.

Wiener, O., 1912. physischen klasse der Konigl. Sachsischen Gesellshaft der Wissenschaften. PhD., 96 pp.

Woopen, M., Balan, A., May, G., Schütz, J., 2014. A comparison of hybridized and standard DG methods for target-based hp-adaptive simulation of compressible flow. Computers & Fluids 98, 3–16. https://doi.org/10.1016/j.compfluid.2014.03.023.

Wu, X.-H., Efendiev, Y., Hou, T.Y., 2002. Analysis of upscaling absolute permeability. Discrete and Continuous Dynamical Systems Series B 2 (2), 185–204.

Wu, X.-H., Parashkevov, R., 2009. Effect of Grid Deviation on Flow Solutions. SPE Journal 14 (01), 67–77. https://doi.org/10.2118/92868-PA.

Yin, J., Park, H.-Y., Datta-Gupta, A., King, M.J., Choudhary, M.K., 2011. A hierarchical streamline-assisted history matching approach with global and local parameter updates. Journal of Petroleum Science and Engineering 80 (1), 116–130. https://doi.org/10.1016/j.petrol.2011.10.014.

Zhang, D., Tchelepi, H., 1999. Stochastic Analysis of Immiscible Two-Phase Flow in Heterogeneous Media. SPE J. 4 (04), 380–388. https://doi.org/10.2118/59250-PA.